

Simulation of Laser Thermal Interaction with Titanium Dioxide /Polyvinyl Alcohol Nanocomposite Thin Films

A.M.Shehap
Physics Department
Cairo University
Cairo,Egypt

Dana.S.Akil
Cairo University
Cairo,Egypt

Abstract: The aim of this work is to use the computational simulation to define the operational conditions to achieve the desired process. The diagnostic tests were used to guide the experiment where PVA composites doped with Titanium dioxide nanoparticles were irradiated with nitrogen laser in order to modify its properties. The temperature of the samples with different laser fluencies were simulated using finite element method, in COMSOL program, to predict the fluencies that is suitable to use for modification before reaching the decomposition temperature of the nanocomposite sample to make sure not to cause any damage. The optical and thermal properties were experimentally studied, and the results were used to define the absorption coefficient and the thermal conductivity of the studied nanocomposites

Keywords: Polymer nanocomposite; Simulation ; pulsed laser ; heat equation .

1. INTRODUCTION

There are various chemical and physical changes caused when materials exposed to electromagnetic radiation. The ability to use the laser to affect a specific and small spot have a great advantage to use in manufacturing integrated circuits and control properties.[1] Many researchers deal with the interaction of laser irradiation with doped polymer films. Laser was used to change the optical structural and thermal properties of polymers and polymers composites like crystallinity and band gap [2,3]. Laser effect on thin films can be simulated by numerical methods to define the operational conditions. Which included minimizing heat effect zone, reaching the melting point ,or reaching ablation threshold.

Computer-assisted technologies for product design usually based on numerical methods, that are able to solve a set of algebraic equations to obtain desired results, in determined boundary conditions of process. Numerical programs are used to calculate tensions, shifts, vibration, heat transfer, fluid flow, and other process parameters [4]

In this work, the COMSOL program is used to build a numerical model capable of simulating the heat transfer and predict the temperature distribution on a thin film of TiO₂/PVA nanocomposited after irradiated by Nitrogen pulsed laser . The aim of this work is to define the Laser dynamic range for modifying the prepared nanocomposites before damaging (i.e the temperature of the nanocomposite does not exceed decomposition temperature of the nanocomposite)

2. THE PROPERTIES OF THE STUDIED NANOCOMPOSITES

The optical properties of the TiO₂ /PVA prepared nanocomposites with different doping percentage (1.25, 2.5, 5, 7.5, 10 % TiO₂/PVA) were studied. The PVA Pure films have absorption band of wavelength $\lambda=198$ nm 208 nm and at 281 nm assigned [25], these three absorption bands are followed by transparency region. It can be understood that the absorption of the Nitrogen laser is neglected since PVA does not have an

absorption peak around 337 nm which is the wavelength of the Nitrogen laser. But in the case of the doped PVA films with TiO₂, a new absorption peak can be noticed around 388 nm which correspond to the absorption of the TiO₂ nanoparticles.It can be seen that the absorption increases by increasing the dopant in the matrix .Table (1) illustrate the absorption coefficient for each nanocomposite film .

3. LASER ABSORPTION IN TiO₂ /PVA NANOCOMPOSITE

Doping PVA polymer with TiO₂ nanoparticles increase the composite absorption of the Nitrogen laser. As the laser is absorbed mostly by the nanoparticles and not by the PVA chemical bonds , we can neglect the photochemical effect and consider the laser effect thermally. The absorbed part of the laser energy in the nanocomposite depend on its properties including reflectivity and absorption which both depend on the wavelength of the laser wavelength .To study the laser thermal effect and temperature distribution we be consider the absorbed laser energy as heat source which is given by [5]:

$$Q(r, t) = \alpha I_0(r, t)(1 - R) \exp(-\alpha z) \quad (1)$$

Where α and R are the absorption coefficient and the reflectivity of the nanocomposite film at the laser wavelength . I is the laser power intensity which depend on time and on the beam shape (which is Gaussian in this case).

The last part of the equation is related to the fact that the laser energy absorption decrease exponentially with depth from the sample surface (z)[6]

$$I(z) = I_0 e^{-\alpha z} \quad (2)$$

The penetration depth of the laser is related to the skin depth for the electromagnetic field

$$\delta = \frac{1}{\alpha} = \frac{\lambda}{4\pi n''(\lambda)} \quad (3)$$

Where, $n''(\lambda)$ is the imaginary part of the complex index of the refraction of the material. δ is the shield depth of the electromagnetic radiation. The thin film of the nanocomposites in our case has 50 μ m thickness which is much smaller than the

penetration depth of the laser, so we can neglect the variation of laser energy with depth.

4. HEAT EQUATION

We used the COMSOL 4.3 to solve the following heat equation:

$$\nabla^2 T(r, t) + \frac{1}{k} Q(r, t) = \frac{1}{\alpha} \frac{\partial T(r, t)}{\partial t} \quad (4)$$

And find the temperature distribution in order predict the laser intensity that could cause damage in the nanocomposite film which means to reach its decomposition temperature.

The prepared nanocomposite films were found to have more stability as the doping ratio increased, as was found by thermal studying of nanocomposites, the decomposition temperature (T_d) is found to increase as illustrated in table (1) Thermal conductivity is a very important factor in the heat equation which is equal to 0.2 W/(m. K) for PVA but increases for the composites because of the TiO_2 doping which has a thermal conductivity about (3.62) W/(m. K) Maxwell calculated the effective thermal conductivity (ETC) of a random distribution of spheres in a continuous medium for low filler concentration [7] as:

$$k_e = k_m \frac{k_f + 2k_m + 2\phi(k_f - k_m)}{k_f + 2k_m - \phi(k_f - k_m)} \quad (5)$$

Where k_e , k_m and k_f are effective thermal conductivity, matrix thermal conductivity and thermal conductivity of fillers, respectively, and ϕ is the volume fraction of inclusions. The calculated values of thermal conductivity of the nanocomposites is illustrated in table (1)

Table 1. experimental values of thermal conductivity, decomposition temperature and absorption coefficient for ($\lambda=337nm$)

Sample TiO_2/PVA (wt/wt %)	k [W/(m. K)]	T_d [C°]	α [cm-1]
0	0.2	288	36.54
1.5%	0.208	290	201.66
2.5%	0.213	302	391.57
5%	0.2269	304	475.81
7.5%	0.2413	306	1023.60
10%	0.3412	319	1093.16

5. SIMULATION AND RESULTS

We can solve the equation using the COMSOL. The films are having the dimension (3cm radius and 0.05 cm thickness). The initial temperature is (300 K). The laser energy (0.375 J), the spot radius (2 cm), pulse duration (15 ns), and repetition rate (0.5 Hz).

The laser is modeled as pulsed heat source and inserted in the heating equation as general inward heat

$$Q = \alpha * hf(x, y, t) * gf(t) \left[\frac{W}{m^2} \right] \quad (6)$$

Where α is the absorption coefficient, $hf(x, y, t)$ is the Gaussian laser beam as in figure (1)

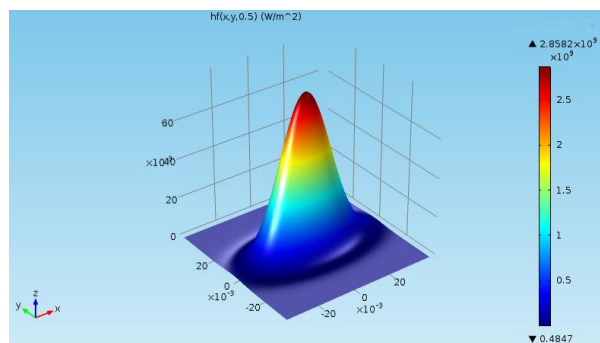


Figure 1. Laser beam used in the simulation.

$gf(t)$ is the pulse function to represent the laser as pulsed train with pulse duration equals to 15 ns that represent the ON stage with the energy equals to 375mJ per pulse, and pulse separation is 2 s which is the OFF stage

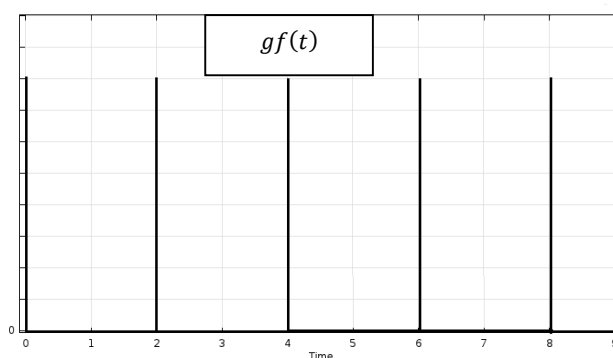


Figure 2. Pulsed function.

The simulations were performed for different number of pulses and for all the nanocomposite samples, until the maximum temperature reaches the decomposition temperature for the specific nanocomposite.

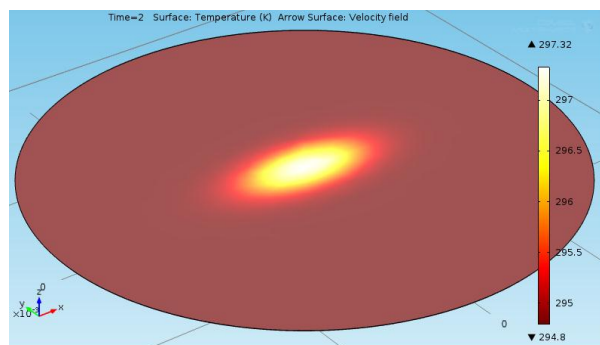


Figure 3. Temperature distribution within 2.5% sample after the first pulse.

Table (2) shows the simulation results. The maximum temperature after one pulse T_{MAX} is found to increase as the nanocomposite doping is higher. As can be seen that after one pulse the maximum temperature increases from the initial temperature only (1°C) for PVA, It is about (30°C) for the 10% nanocomposite sample.

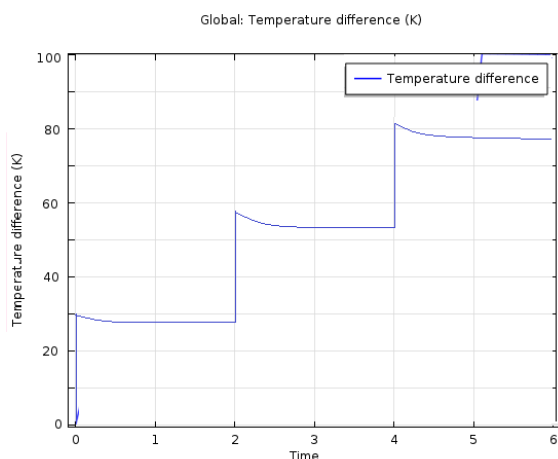


Figure 4. temperature change with time during simulation for sample 10%.

This can be understood since the absorption coefficient increases by increasing TiO₂ ratio. Heat diffusion in the thin film is faster for higher doped composites. It can be seen from the simulation that the PVA is hardly affected by the Nitrogen laser. Since the maximum temperature rose about 1°C and decreases before the next pulse. The laser gets more effective as the doping ration increases. And the decomposition temperature could be reached by lower fluencies as shown in table (2)

Table 2. Simulation values for maximum temperature after one pulse and the damage threshold

Sample TiO ₂ /PVA (wt/wt %)	T _{Max} [C]	Damage threshold [J]
0	1	-
1.5%	5.5	1.611
2.5%	11	0.836
5%	13	0.716
7.5%	28	0.328
10 %	30	0.298

6. CONCLUSION

Laser heat effect on TiO₂ /PVA nanocomposie thin films were simulated using COMSOL 4.3. The nanoparticles increases laser absorption in the nanocomposite thin films, which causes lower damage threshold for the nanocomposites by increasing doping percentage.

7. REFERENCES

[1] Wehner M., Beckemper S., Jacobs P., Schillinger S., Schibur D., Gillner A. (2005) Processing of polycarbonate by high-repetition rate ArF excimer laser radiation, in Proceedings of the Third international WLT conference

on Lasers in Manufacturing (LIM2005), Munich, Germany, 557- 561.

- [2] Jassim, A. S., Dahham, N. A., & Maric, M. Sh. (2010). Study of theoptical properties for ZnS thin film irradiated by Co2 laser. *Ibn Al-Haitham Journal for Pure and Applied Science*, 23(3), 58e67.
- [3] Shan-Ting Hsu*, Huade Tan, Y. Lawrence Yao *Polymer Degradation and Stability* 97 (2012) 88e97
- [4] Andrade, S. R., Jardini, A., Wolf Maciel, M. R., Maciel Filho, R., 2006, Numerical Simulation of Localized Cure of Thermosensitive Resin During Thermo Stereolithography Process (TSTL) *J Appl Polym Sci* 102, 2777 – 2783
- [5] Generating Micro- and Nanopatterns on Polymeric Materials Aranzazu del Campo , Eduard Arzt
- [6] Frenk Kreith, *The CRC handbook of thermal engineering* , : CRC Press LLC, 2000
- [7] Sajjan Kumar¹, Rajpal Singh Bhoopal¹, Pradeep Kumar Sharma¹, Radhey Shyam Beniwal², Ramvir Singh^{1*} *Open Journal of Composite Materials*, 2011, 1, 10-18

A Comparative Study Of Remote Access Technologies and Implementation of a Smartphone App for Remote System Administration Based on a Proposed Secure RFB Protocol

Ernest D. Ganaa
School of Applied Science &
Technology
Department of Information &
Communication Technology
Wa Polytechnic
Wa, Ghana

Frimpong Twum
College of Science
Dept. of Computer Science
Kwame Nkrumah University of
Science & Technology
Kumasi, Ghana

J. B. Hayfron- Acquah
College of Science
Dept. of Computer Science
Kwame Nkrumah University
of Science & Technology
Kumasi, Ghana

Abstract: In this paper we proposed advanced technologies to provide tremendous support for network administrators by implementing a secure remote system administration app that runs on android smartphones to aid them administer their servers remotely when they (network administrators) are out stationed using their smartphones.

The android app developed in eclipse establishes a secure connection with a remote server running a PHP application. The app was developed based on the Remote Frame Buffer (RFB) protocol. The RFB protocol, a display protocol has some security lapses including being vulnerable to Man-In-The-Middle (MITM) attack using a few tools and techniques. This research therefore incorporated a self-signed Secure Socket Layer (SSL) certificate in the android app to enable secure encrypted connections to be established between the android app and the remote server to ensure end-to-end security against attacks such as Man-In-The-Middle (MITM).

The whole system was deployed based on client-server architecture with the hand-held smart devices as clients, providing real-time network access to network administrators to their remote servers.

The secure RFB protocol proposed and implemented in the android app was compared with other existing software for remote system administration such as Remote Desktop (RDP), and RFB protocols using ICMP ping command. The results show that the average response time of the RDP protocol was 436ms, that of the RFB protocol was 496ms and that of the android app which is based on a proposed secure RFB protocol was 474ms.

Keywords: Remote access; Remote Frame Buffer; Remote Desktop Protocol; Android app; Remote server; Remote system administration

1. INTRODUCTION

There are several situations where network administrators are faced with the problem of monitoring and administering their various computer networks while away from their offices. In such circumstances, the network administrators depend on third party reports to know the status of their networks. Some even have to direct such third parties as to how to resolve network issues on their behalf when they (network administrators) are out stationed which most times leads to networks jamming and other related issues.

This research looks at remote access technologies and how to implement a smartphone app for remote system administration so as to create some kind of virtual office(s) for System Administrators who will like to always be tied up to their networks even if they are out stationed.

Also, in today's world, it is not a question of whether a remote access software will be used, but which one of the available remote access software will be selected by users and how the selected product will be configured to minimize security risk. It is against this background that this research seeks to conduct a comparative study on remote access technologies in short messaging system (SMS) to perform system administration tasks.

This research work intends to build an android app based on a proposed secure RFB protocol sitting on a smart device that will communicate with a network server running a Hypertext Pre-Processor program. The proposed android app which will act as an interface to the network server will connect to the server using Virtual Private Network (VPN) technology.

The server will perform the processing and send responses back to the android app. As an example, android app will be responsible for issuing basic commands like creating files and as well as performing basic server management task such as creating users, setting user privileges, etc.

2. AIM OF RESEARCH

The aim of this research is to do a comparative study of remote access technologies and implement a smartphone app for remote system administration based on a proposed secure RFB protocol.

The specific objectives are as follows:

- ✓ To investigate what remote access technologies are available
- ✓ To examine the current usage of remote access technologies

- ✓ To evaluate the security of current remote access technologies
- ✓ To implement a smartphone app for remote system administration based on a proposed secure RFB protocol
- ✓ To evaluate the performance of existing remote access technologies as against a proposed secure RFB protocol.

3. SYSTEM OVERVIEW

The purpose of the system is to allow system administrators monitor and administer their computer networks remotely using their android smartphones.

With this system, a system administrator can create a user remotely, create, view and modify text files remotely, check network status, shutdown a server and set user privileges.

The system was developed based on a proposed secure RFB protocol with self-signed Secure Socket Layer (SSL) certificate incorporated into this RFB protocol to ensure end-to-end encrypted connections between the smart device (client) and server.

The system can be used to monitor and administer only one server at a time.

3.1 System Architecture

The system is client-server architecture with the smartphone as the client and the remote computer to be administered as the server.

The android app runs on a smartphone and it is responsible for issuing commands to the remote server. The android app acts as an interface to the remote server.

The restful PHP application runs on the remote server machine and is responsible for processing and returning all requests to the smart device. The database keeps track of all administrators who logon to the system and the activity performed for audit trail purposes.

Figure 1 shows the block diagram of the system, figure 2 shows the system architecture and figure 3 shows the flow of the system.

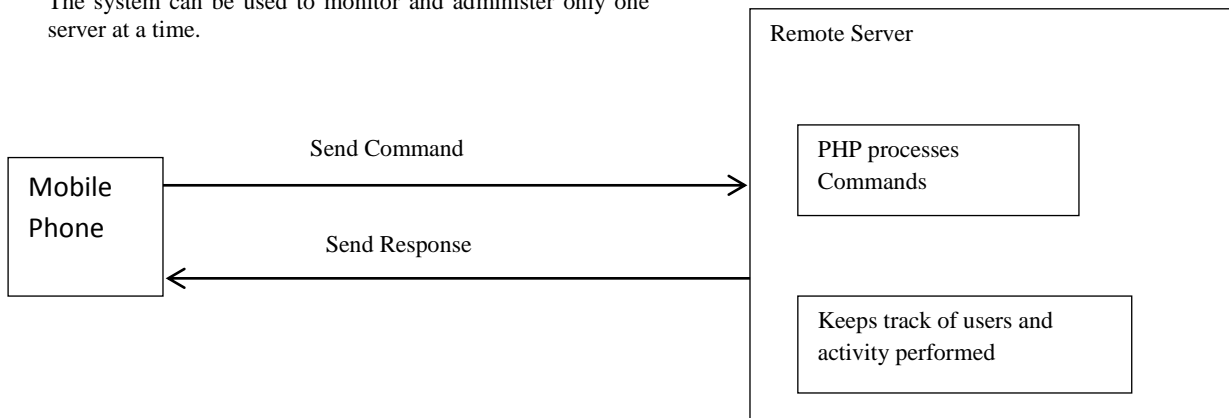


Figure 1. Block Diagram of System. Source Authors' Construct 2015

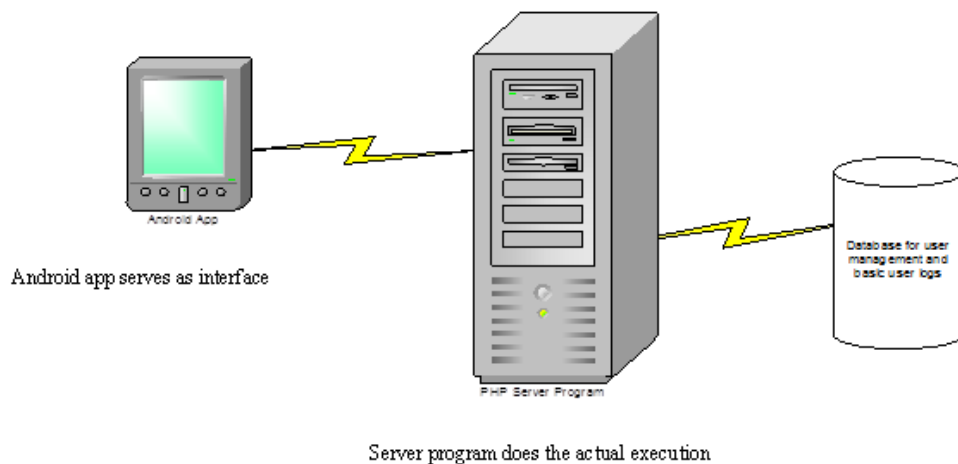


Figure 2. Architecture of system. Source Authors' construct 2015

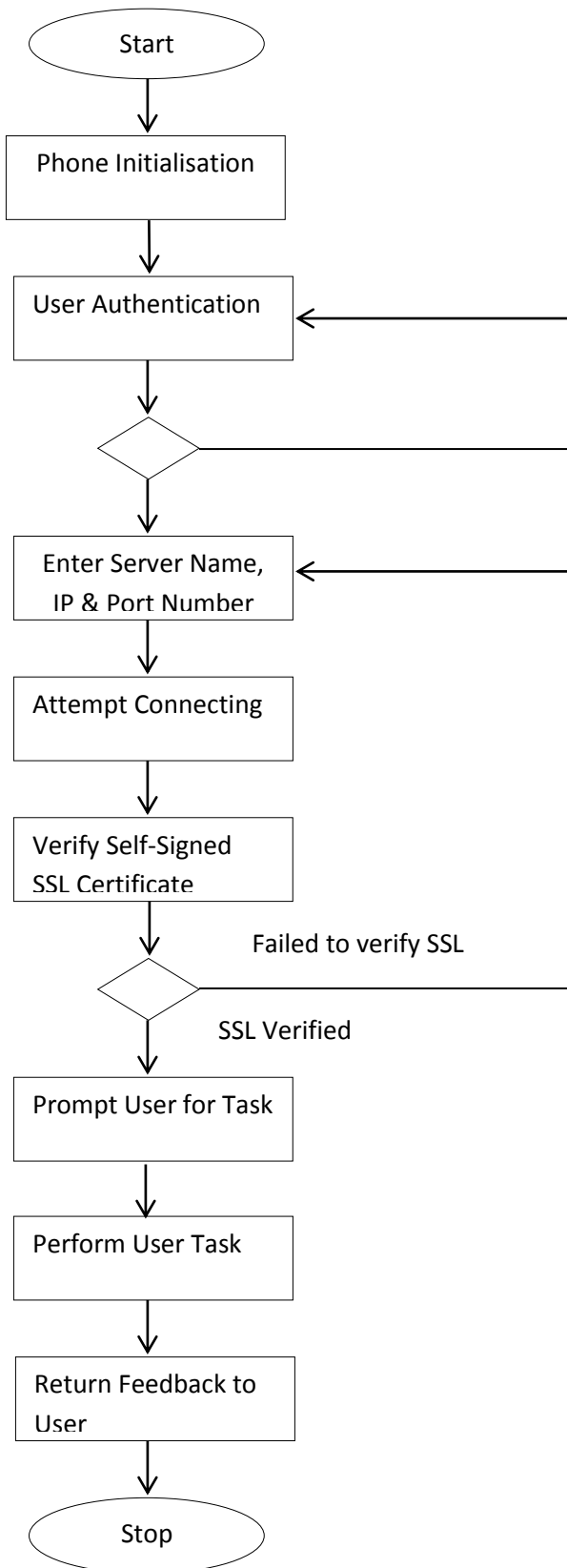


Figure 3: Flow of system. Source: Authors' construct 2015.

3.2 Evaluation of existing Remote Access Technologies

The All remote access systems or applications are developed based on existing and or appropriate technology or technologies. Some existing technologies available for developing remote access systems are:

i. The Remote Frame Buffer (RFB) protocol

The RFB protocol is a simple protocol for sending graphics to be displayed on a remote display or screen. RFB protocol places very little demand on the remote display in terms of processing power and memory demands since all processing is done at the server side. This protocol is a true thin client protocol because it has very low bandwidth requirements and shifts all processing demands to the RFB server instead of the RFB client (Kerai, 2010). The major interest in designing this protocol is to make very few requirements of the client in terms of processing (Richardson, 2010).

The two remote endpoints in the RFB protocol are referred to as the RFB client or viewer and the RFB server (Baig et al., 2012). It works by simply taking rectangles of screen data from the RFB server with a given position and size and puts them into its frame buffer so that they appear in the correct place on the RFB client's screen (Masthan et al., 2013).

Despite the fact that RFB protocol uses encrypted passwords and network, any communication over the network is vulnerable and can be attacked by a Man-In-The-Middle (MITM) by using a few tools and techniques (Kerai, 2010). Also, the applications of VNC which are developed based on RFB protocol are generally slower, offer fewer features and security options than Remote Desktop (RD) which is based on the RDP protocol (Masthan et al., 2013).

Virtual Network Computing (VNC) was developed based on the RFB protocol (Baig et al., 2012).

ii. The Remote Desktop Protocol (RDP)

RDP is a proprietary protocol designed by Microsoft for remote input and display of host running the windows operating systems which is based on the Multipoint Application Sharing (T.128) recommendation by Telecommunication Union (Youming, 2013).

By default, the data that travels between the terminal server and the client is protected by the RC4 symmetric encryption algorithm which provides three levels (high level, medium level and low level) of security (Kerai, 2010). The high level security encrypts data sent from the client to the server using a 128 bit key and does same to data sent from server to client, the medium level security encrypts both data sent from client and server using a 56 bit key if the client is using at least windows 2000 and low level security only encrypts data sent from client to server using 56 bit key or 40 bit key.

According to Montoro (2005), though the data sent between the server and client is encrypted, the RDP protocol may be prone to Man-In-The-Middle attack because there is no verification of the identity of the server when setting up the encryption keys for a session.

The MITM attack works as follows:

- ✓ When the client connects to the server, by DNS spoofing (making a DNS entry point to another IP

address than it was supposed to point to) or ARP poisoning (entering a fake IP address in a host ARP table) which causes diversion of traffic to a different host, the client is fooled to connect to the MITM instead and the MITM in turn sends a request to the server. This involves maliciously modifying the relation between an IP address and its matching MAC address (Behboodan & Razak, 2011)

- ✓ Through this, the server then sends its public key, in clear text through the MITM and the MITM now sends the packet further to the client, but exchanging the public key with another one for which it knows the private part.
- ✓ The client upon receiving this sends a random salt, encrypted with the server's public key, to the MITM. The MITM decrypts the client's random salt with its private key, encrypts it with the real server's public key and sends it back to the server.
- ✓ The MITM now knows both the server and the client salt, which is enough information to construct the session keys used for further packets sent between the client and the server.

This vulnerability occurs because the client by no means will try to verify the public key of the server. In other protocols such as the Secure Shell protocol (SSH), most client implementations solve this MITM attacks by allowing the user to answer a question whether a specific server's key fingerprint is valid (Montoro, 2005).

Microsoft confirmed the above problem and fixed the new versions of Remote Desktop Clients. Recent clients now check the Terminal Server's identity to verify its public key before allowing connections. The implication of this is that Remote Desktop has a very strong security, but of course, as time passes by, attackers develop more sophisticated tools to break through. Nam et al. (2012) also stated that ARP (Address Resolution Protocol) poisoning can be resolved by delivering the public key and the MAC address of the server to the client, however this is to be set by the network administrator manually.

Remote Desktop Protocol (RDP) 6.0 supports Secure Socket Layer (SSL) and Transport Layer Security (TLS) protocols which encrypt data sent between a server and a client (Boling, 2007). Quite a number of the Windows operating systems such as Windows Server 2003 SP1, Windows Server 2008, Windows XP, Windows Vista, Windows 7 and Windows 8 support SSL/TLS for RDP 6.0.

Despite the MITM security problem, RDP is designed to support different types of network topologies, multiple LAN protocols and just like VNC, RDP works on TCP/IP connections (Kerai, 2010).

4. The Proposed Secure RFB Protocol and Implementation of an Android Smartphone App for Remote System Administration

Based on the fact that the RFB protocol, a display protocol has some security lapses including being vulnerable to Man-In-The-Middle (MITM) attack using a few tools and techniques, the study in trying to secure the RFB protocol implemented a self-signed Secure Socket Layer (SSL) certificate on top of the RFB protocol. The purpose of this is to enable secure encrypted connections to be established

between the android app and the remote server to ensure end-to-end security against attacks such as Man-In-The-Middle (MITM)

Secure Socket Layer (SSL) certificate is a cryptographic protocol that creates an encrypted communication channel between a server and client that makes internet traffic indecipherable to third parties that might intercept them (Roosa & Schultze, 2010).

A self-signed certificate is one that is signed by the individual who created it rather than a trusted Certificate Authority (Code Project, 2014). This research used a self-signed certificate because they are very convenient in mobile development since mobile apps in most cases interact with only one server unlike web browsers. Also, if well implemented, they work like certificates from a certificate authority.

This is how the self-signed certificate was created on the server the android app will be communicating with:

- ✓ A KeyStore is created using "bcprov-jdk15on-146.jar" which is a java class. This class can be downloaded from www.bouncycastle.org/download/bcprov-jdk15on-146.jar. This file will be stored in "C:\androidproject". This file is used to generate the KeyStore.
- ✓ A keytool is then used to generate the key "keytool -genkey -alias androidproject -keystore C:\androidproject\androidprojectssl.keystore -validity 365".
- ✓ The above generated key is then exported from the .KeyStore file to .cer file using the command "-export -alias androidproject -keystore C:\androidproject\androidprojectssl.keystore -file C:\androidproject\androidprojectsslcert -cer"
- ✓ The keystore file is then saved in "/androidappdir/raw/".
- ✓ A class called MyAndroidClient is then written to hardcode the self-signed generated certificate in the android app.

In implementing this self-signed certificate created above in the android app, the study sets up a custom TrustManager that will trust the above self-signed certificate. This custom TrustManager is then provided with custom SSLContext as demonstrated in the code snippet shown in figure 4 below. The idea here is to do certificate pinning with this self-signed SSL certificate by hard-coding the certificate known to be used by the server in the android app so that the app will then ignore the smartphone's trust store and rely on its own trust store thereby terminating connections that do not match with this self-signed certificate.

```
import java.io.InputStream;
import java.security.KeyStore;

import android.content.Context;

public class MyAndroidClient extends DefaultHttpClient {

    private static Context context;

    public static void setContext(Context context) {
        MyAndroidClient.context = context;
    }

    public MyAndroidClient(HttpParams params) {
        super(params);
    }

    public MyAndroidClient(ClientConnectionManager httpConnectionManager, HttpParams params) {
        super(httpConnectionManager, params);
    }

    @Override
    protected ClientConnectionManager createClientConnectionManager() {
        SchemeRegistry registry = new SchemeRegistry();
        registry.register(new Scheme("http", PlainSocketFactory.getSocketFactory(), 80));
        registry.register(new Scheme("https", newSSLSocketFactory(), 443));
        return new SingleClientConnManager(getParams(), registry);
    }

    private SSLSocketFactory newSslSocketFactory() {
        try {
            InputStream in =
                MyAndroidClient.context.getResources().openRawResource(R.raw.androidprojectssl);
            try {
                trusted.load(in, "g@@@1984".toCharArray());
            } finally {
                in.close();
            }
            SSLSocketFactory sf = new SSLSocketFactory(trusted);
            sf.setHostnameVerifier(SSLSocketFactory.STRICT_HOSTNAME_VERIFIER);
            return sf;
        } catch (Exception e) {
            throw new AssertionError(e);
        }
    }
}
```

Figure 4. Code snippet for implementing self-signed SSL certificate

5. Evaluating the performance of the RDP, RFB, and the Proposed Secure RFB Protocol

The performance of the proposed secure RFB protocol implemented in the android app was compared with existing remote access software which are based on the RDP, and the RFB protocols respectively using ICMP ping command. Figure 5 below shows the ICMP ping results for the RDP protocol.

```
Pinging 27.0.0.1 with 32 bytes of data:  
Reply from 27.0.0.1: bytes=32 time=399ms TTL=47  
Reply from 27.0.0.1: bytes=32 time=412ms TTL=47  
Reply from 27.0.0.1: bytes=32 time=532ms TTL=47  
Reply from 27.0.0.1: bytes=32 time=404ms TTL=47  
  
Ping statistics for 27.0.0.1:  
Packets: Sent = 4, Received = 4, Lost = 0 (0% loss),  
Approximate round trip times in milli-seconds:  
Minimum = 399ms, Maximum = 532ms, Average = 436ms
```

Figure 5: RDP protocol ICMP ping results

Figure 6 below shows the ICMP ping results for the RFB protocol.

```
Pinging 27.0.0.1 with 32 bytes of data:  
Reply from 27.0.0.1: bytes=32 time=486ms TTL=47  
Reply from 27.0.0.1: bytes=32 time=405ms TTL=47  
Reply from 27.0.0.1: bytes=32 time=441ms TTL=47  
Reply from 27.0.0.1: bytes=32 time=652ms TTL=47  
  
Ping statistics for 27.0.0.1:  
Packets: Sent = 4, Received = 4, Lost = 0 (0% loss),  
Approximate round trip times in milli-seconds:  
Minimum = 405ms, Maximum = 652ms, Average = 496ms
```

Figure 6: RFB protocol ICMP ping results

Figure 7 shows the ICMP ping results for the secure RFB protocol



Figure 7: The Proposed Secure RFB protocol android app ICMP ping results.

6. Conclusions, Recommendation, and Acknowledgment

From the study, it was revealed through literature that by default the data that travels through the terminal server and client in the case of the RDP protocol is protected by the RC4 symmetric encryption algorithm which provides 3 levels of security. It was further revealed through literature that applications based on RFB protocol offer fewer features and security options than remote desktop which is based on the RDP protocol.

The study has successfully implemented a smartphone app for remote system administration based on a proposed secure RFB protocol. Self-signed SSL certificate was incorporated into the RFB protocol to make it a secure RFB protocol to ensure that secure encrypted connections are established between the smartphone and the server.

This research also revealed that the average response time of the RDP protocol (Remote Desktop) was 436ms, the average response time of the RFB protocol (VNC) was 496ms and the average response time of the android app which is based on a secure RFB protocol was 474ms.

It is recommended that in the future the android app be made to be able to monitor and administer at least two remote servers at a time.

We thank God for his mercies given to us to complete this work.

7. REFERENCES

- [1] Baig S, Rajasekar M. & Balaji P. (2012) Virtual Network Computing Based Remote Desktop Access. *International Journal of Computer Science and Telecommunications*. Volume 3, Issue 5. pp. 127.
- [2] Behboodian N. & Razak S. A. (2011) ARP Poisoning Attack Detection and Protection in WLAN via Client Web Browser. *International Conference on Emerging Trends in Computer and Image Processing*. pp. 20.
- [3] Boling D. (2007) Windows Embedded CE 6.0 R2 Remote Desktop Protocols and Internet Explorer. pp. 6. Retrieved from: <http://download.microsoft.com/download/5/8/e/58e0c008-fc15-4a3b-9728-c0103bab6473/Windows%20Embedded%20CE%206.0%20R2%20Remote%20Desktop%20Protocol%20and%20Internet%20Explorer%20whitepaper.pdf>.
- [4] Code Project (2014) Android Security-Implementation of Self-Signed SSL Certificate for your App. Retrieved from: www.codeproject.com/articles/826045/android-security-implementation-of-self-signed-SSL
- [5] Kerai P. (2010) Tracing VNC and RDP Protocol Artefacts on Windows Mobile and Windows Smartphone for Forensic Purpose. *In Proceedings of International Cyber Resilience Conference*. Australia. pp. 58. Retrieved from: <http://ro.ecu.edu.au/icr/7>

- [6] Masthan K, Kumar S. K. & Prasad H. V. (2013) Virtual Network Computing of User Appliances. International Journal of Computer Science and Mobile Computing. Volume 2, Issue 8. pp. 132.
- [7] Montoro M. (2005) Remote Desktop Protocol, the Good the Bad and the Ugly. pp. 1-2. Available from: www.oxid.it.
- [8] Nam Y. S, Jurayev S, Kim S, Choi K. & Choi S. G (2012) Mitigating ARP poisoning-base man-in-the-middle attacks in wired or wireless LAN. *EURASIP Journal on Wireless Communication and Networking*. pp. 2.
- [9] Richardson T. (2010) *The RFB Protocol*. pp. 3. Retrieved from: www.realvnc.com.
- [10] Roosa S. B. & Schultze S. (2010) The “Certificate Authority” Trust Model for SSL: A Defective Foundation for Encrypted Web Traffic and a Legal Quagmire. *Intellectual Property & Technology Law Journal*. Volume 22, Number 11. pp. 3.
- [11] Youming L. (2013) *Virtual Networking for Mobile Cloud Computing*. Master's Thesis, Aalto University-Finland. pp. 19. Retrieved from: https://into.aalto.fi/download/attachment/.../Lin_Youming_thesis.pdf?

Information Management System and Website Server Penetration Testing Case Study University

Agustinus Noertjahyana
Informatics Engineering
Petra Christian University
Surabaya, Indonesia

Richard Pangalila
Informatics Engineering
Petra Christian University
Surabaya, Indonesia

Justinus Andjarwirawan
Informatics Engineering
Petra Christian University
Surabaya, Indonesia

Abstract: A developing organization need information technology in its operational activity. However what is often considered is how to ensure that data saved in server is safe from unauthorized parties. Therefore, this thesis reviews how a person who is appointed as a security analyst do penetration testing in a system with variety tools given and how the report can be understood from by people from managers to programmers. Besides giving the how-to knowledge, this thesis also reviews how secure is the organization under review in keeping their data safe from other parties who are not supposed to get access to important operational activity data.

Keywords: Safety, Data, Evaluation, Penetration Testing, Security

1. INTRODUCTION

An organization who runs a system using IT-based always use computer in its operational activity. With development of IT, a need of storage medium or even data center is needed which called servers. However with such development, security is an aspect to be aware of by anyone who uses centralized system, because hacking, manipulation or even loss of data might happen if done by hacker who have bad deed to take sensitive data from an organization [1].

To reduce loss caused by hacker, the first step needed is to evaluate server securities. It's to reduce the risk of misconduct of available resources in an organization [2].

Most people within organization might get confused when requested to do a server security evaluation. This is because lack of knowledge in server evaluation. The method to evaluate an object security by penetrating it is called Penetration Testing or known as Pen testing [3].

Development in Petra Christian University is getting bigger and there's a lot of need in information system to run its operational activity. PCU has a lot of servers in each building such as P Building, T Building and RP Building. With network availability in each area of building throughout wireless and wired network, there's a need to pay attention it's relevancy between hacker and server within the network. Computer Center in RP Building held the main server which provides the basic system of students' academic activity.

Moreover things that also needed to be aware of is the student and staffs behavior because the one who conduct hacking is human themselves, sometimes a bad human behavior might bring bad effect directly or indirectly. Because of those problems, the most needed help is reducing and anticipate attacks from hackers which is monitoring servers in RP Building while doing penetration testing.

2. BASIC THEORY

2.1 Computer Security

The main goal of computer security is to protect information within it. Computer security is based on some aspects which listed on Ethical Hacking and Countermeasures module [3], such as:

Privacy, an object that is private which only limited few person who has access to it.

Confidentiality, data given to other party and being kept to select person.

Integrity, information not allowed to be changed unless by information owner.

Authentication, user verification through login window using user credentials and password, if matched it will be accepted and *vice versa*.

Availability, data availability when needed.

There are some steps to secure computer which explained in Ethical Hacking and Countermeasures module [3], such as:

Assets, assets protection is an important aspect and the first step from computer security implementation.

Risk analysis, identification to risk that might happen, such as a potential event to cause harm to systems.

Network security, all devices connected to network need to be assessed its security.

Tools, tools used on PC have an important role in security because the tools need to be secure.

Priority, whole PC protection.

2.2 Certified Ethical Hacking

Certified Ethical Hacker is a professional certification provided by International Council of E-Commerce Consultants (EC-Council).

Ethic hacker usually hired by organization who trusted them to do penetration testing o network or computer system with common method used by hacker to find and fix security vulnerabilities. If hacking done without organization authorization, it will be counted as cybercrime, but whereas authorized or requested it will be a legal action.

Certified hacker have certification in findings security vulnerabilities and system flaw using knowledge and tools like a real hacker.

Citing from EC-Council website, the certification code for CEH is 312-50 and it's in version 8 as of 2013. EC-Council also offers other certification which called Certified Network Defends Architect or known as CNDA. This certification is designed for America government agency and only available on certain agency with different names but have the same content, this certification code is 312-99.

2.3 Penetration Testing

Citing from CEH module, penetration testing is a method to evaluate computer system security or network by simulating attack from a dangerous source and a part of security audit [3]. This attack simulation is done like black hat hacker, cracker and others. The goal is to decide and know what kind of possible attack to be done to system and what risk might happen because of system vulnerability.

When doing penetration testing, intensive analysis is needed in each flaw caused by system weakness. Later on after the whole analysis is done, it will be documented and given to the owner along with solutions and effects caused by existing security vulnerability.

3. PEN TESTING METHODOLOGY

3.1 Penetration Testing Technique

There are a lot of things to be tested in penetration testing, it's because to give more picture to identify more threats such as communication failure, e-commerce, or even loss of private information. Moreover when facing public infrastructure such as e-mail gateway, remote access, DNS, password, FTP, IIS and site server, everything need to be tested from hardware through software.

There are some supporting factors like goals, limitation and procedure adaptation needed to maximize penetration testing. In spite of that there are some consideration between cost and the level of people doing the test. Finally there's also need of clear documentation and explanation of risk potential and findings results from analysis results and tests to client.

Citing from Licensed Penetration Tester module, there are some common techniques used in penetration testing, such as:

1. Passive Research : used to find all common information used in an organization
2. Open Source Monitoring : how open an organization to keep information integrity and private
3. Network Mapping and OS Fingerprinting : used to get network configuration being tested
4. Spoofing : system disguise testing in a computer registered to system, tested on both external and internal side
5. Network sniffing : running data capture in a network
6. Trojan Attacks : malware sent in a network in form of e-mail attachment or sent through a chat room
7. Brute-Force Attack : common technique to open password and able to overload a system or even denying access to whole requests
8. Vulnerability Scanning : overall checking on infrastructure target area of organization network
9. Scenario Analysis : final testing consists with testing and more accurate vulnerability security risk scoring in real-world case

3.2 Penetration Testing Scope

When doing penetration testing, there will be limitation to cover the need of clear analysis, such as how destructive the test will be. Based on the effect of testing, penetration testing divided into two types, they are destructive and non-destructive tests. Both of these tests will map all vulnerabilities and verify any findings with exploits available but the nondestructive type won't go as far doing Denial of Service and Buffer Overflow like the destructive test will do to prevent disruption on system.

3.3 Penetration Testing Types

As explained in LPT module there are two teams in penetration testing, red team and blue team [3]. Blue team is the one who test with the acknowledgement of IT staff, usually it comes

with lower cost and the need of main activity to think about how a sudden attack being launched. In contrary, the red team does the testing without the knowledge of IT staff but with the managers of the company's consent. The goal of red team is to detect network and system's flaw with security check from the attacker's perspective to infrastructure.

Apart from teaming, there are kinds of penetration testing such as black-box, white-box or grey-box. They are differentiated by how they do the penetration test. Black-box pen test uses external method which the tester given only the information of the organization without any blueprint or organization schema, they will do penetration testing like a real hacker and cost more time and money. Unlike black-box pen test, white-box pen test uses internal method which the tester given all of the information of the blueprint or organization schema while the test will be conducted like a real staff inside the organization and also the target of tests already decided beforehand. This kind of testing method might be conducted with or without any announcement to the internal IT staff. The last kind is grey-box, where the tester will do the test from inside the organization while analyzing each applications vulnerabilities. This test will need a complete knowledge and also test from black-box kind to get a whole picture of vulnerabilities.

3.4 Research Flowchart

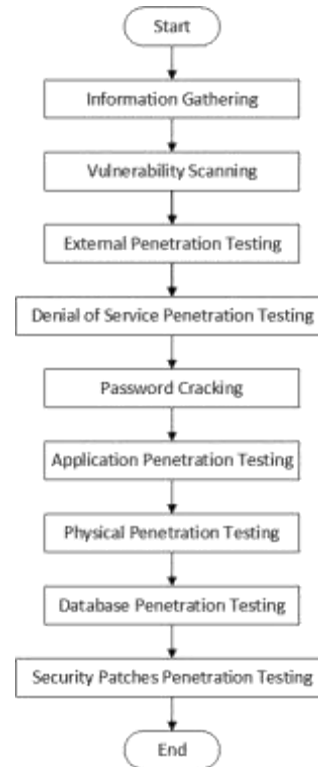


Figure 1. Research Flowchart

The flowchart on Figure 1 is based on LPT module and it will be implemented on this research. For the first step of research is to gather information regarding to physical server location, network type, and devices being used and other information related to PCU servers. After collecting all data, there will be a vulnerability scan. The next step will be external penetration testing to find out what information can be gathered and related to PCU servers from the sites. After collecting enough data, there will be a DoS pentest to find out how the servers managed to stay available under attack. Password cracking is needed to be done to find out weak passwords on systems [4].

Tests will be continued with application to evaluate PHP version, framework and additional services used on servers. Besides running softwares, physical access need to be tested such as how the servers being positioned, cabling arrangements, and other things related to physical access. Next step is to conduct database penetration testing such as MySQL, PostgreSQL, and its kind. The last step is to find out the security patch is applied or not in the system.

Later on after completing the whole tests, there will be a report based on LPT flowchart module as a standard that being used by analyst.

Based on the Penetration Testing module, this research will run under grey-box method to since some of the network schema already known and given from the foundation and also this test will be known as a blue team since it came from internal side of the foundation. To minimize service disruption this test will be on the non-destructive side.

4. APPLICATION IMPLEMENTATION

4.1 WHOIS

Citing from Internet Corporation for Assigned Names and Numbers (ICANN) website, WHOIS is a query and respond protocol that commonly used to query database regarding registered user or internet resources such as domain name, IP address block, or automated system, and also used for other information. This protocol save and send database content in a format readable by human [5].

4.2 NSLookup

Based on UNIX manual book inside the operating system, NSLookup is a command-line tool for network administration which available on all operating system to grab information about Domain Name System record [6]. Citing from Computer Hope said that during the development of BIND 9, Internet System Consortium wanted to deprecate NSLookup in favor of host and dig which provide higher level of industry acceptance, but later it was reversed during the launch of BIND 9.3 and finally there is a full support of NSLookup function NSLookup means Name Server Lookup, it didn't use DNS library to do query so the result might differ from other function dig.

NSLookup is operatable in interactive mode and non interactive mode. When the mode is interactive, it can be used as an argument like common applications. If operated on non interactive mode, information is searched based on argument which was set beforehand as destined.

4.3 NetCraft

Netcraft is an Internet Service Provider in England. Netcraft was paid to provide services like: internet security service, application testing, source code review and automated penetration testing. Netcraft also provide data and analysis from any internet aspect.

4.4 ID Serve

Based on GRC.com, the founder's site, ID Serve is a freeware developed by Steve Gibson and useful to investigate essential security [7]. The main function is to do general check of a webserver. This program can give information regarding operating system used in server and other additional functions also included such as cookie and reverse DNS. Gibson Research Corp. developed many softwares useful for users. Usually the tools developed including:

- Finding vulnerabilities in server
- Firewall filter configuration
- HTTP and non HTTP server identification
- Reverse DNS Lookup using DNS to find out IP address

ID Serve is useful to create a security test to webserver. ID Serve functioned to give out information in readable form for users, the application also shows a port status is closed or hidden. The other function of ID Serve is to track a domain name from an IP address which shown in users' computer firewall log and ensure the owner for the security of their commercial sites.

4.5 HTTPRecon

Based on the project owner Marc Ruef's site, HTTPRecon defined as a site fingerprinting tool, this project runs on HTTP fingerprinting research area. The goal is to find out HTTP implementation in a complete way and also help in identifying vulnerability potential. The approach method used is automated from many sources to simplify and increase efficiency in enumeration website. Other method like banner-grabbing, code enumeration status and analysis used on header is also being used in this program.

4.6 OpenVAS

Based on OpenVas.org site, OpenVAS (Open Vulnerability Assessment System) is a framework contains some services and tools to offer security vulnerability findings and giving solutions [8]. This program is available for free under GPL license and the newest version is 8.0. This research will run the virtual operating system version provided by OpenVAS on Virtual Machine Oracle VirtualBox.

4.7 Acunetix

Based on Acunetix.com, Acunetix Web Vulnerability Scanner is an automated security test application which checks security vulnerability like SQL Injection, cross site scripting and exploitable vulnerability. This program focused on variety of exploits and vulnerabilities which make this program better than other vulnerability scanners [9].

5. APPLICATION TESTING

5.1 Information Gathering

5.1.1 WHOIS

With site such as DomainTools, information regarding the history of a domain is listed and viewed in WhoIs format, where information like domain creation date, owner of domain and simple information such as server system being used, location and IP address included in it. The result shown that www.xxxxx.ac.id and its subdomain listed under the name Mr. Justinus Andjarwirawan.

5.1.2 NSLookup

Domain www.xxxxx.ac.id is listed in PANDI domain registrar and have the IP address 203.189.120.xxx, along with Mail Exchanger from Google and the Nameserver located on local server owned by Petra with name Peter and Jacob and a backup DNS on ZoneEdit. There's a TXT type DNS which list domain verification so when e-mail sent from xxxxx.ac.id domain it won't be blacklisted. Other subdomain dewey.xxxxx.ac.id alongside bakp.xxxxx.ac.id only show canonical name or other alias as digilib.xxxxx.ac.id for Dewey and cpanyel.xxxxx.ac.id for BAKP. While sim.xxxxx.ac.id site shows result 203.189.120.xxx as its IP address.

5.2 Webserver Footprinting

5.2.1 NetCraft

Www.xxxxx.ac.id site appeared for the first time on May 1996. This site is owned by Petra Christian University and there are few times hosting change from PT. Telkom Indonesia then developed by PCU foundation alongside the change there's also IP address change from 203.130.237.183 to 203.189.120.xxx and lastly to 203.189.120.xxx.

Sim.xxxxx.ac.id site first appeared on August 2011 with IP 203.189.120.xxx. No historical change of server for this site but there's a reboot activity shown 40 days ago during the test.

Dewey.xxxxx.ac.id site first appeared on November 2001, this site is an online library catalogue. This site is also under the foundation and there are changes to hosting for 3 times with IP address firstly shown as 202.43.253.210 to 203.189.120.xxx and lastly 203.189.120.xxx.

The last site, bakp.xxxxx.ac.id first appeared on June 2012, no historical changes on server or reboot activity shown because this site is not yet listed on NetCraft database before. Currently the IP address shown is 203.189.120.xxx.

5.2.2 ID Serve

From test result www.xxxxx.ac.id identified running an Apache based server with version 2.2.21 in UNIX operating system with OpenSSL module version 0.9.8. Sim.xxxxx.ac.id shown running under Debian with PHP version 5.2.6.1, the next site is Bakp.xxxxx.ac.id running under Apache version 2.2.27 with OpenSSL version 0.9.8. Lastly dewey.xxxxx.ac.id running a Debian OS with Apache version 2.2.16.

5.2.3 HTTPRecon

Differ from ID Serve result, www.xxxxx.ac.id shown using HTTP Apache webserver version 1.3.33, while dewey.xxxxx.ac.id and sim.xxxxx.ac.id both are running Apache 2.0.55. Lastly bakp.xxxxx.ac.id identified running Apache version 2.0.52.

5.3 Vulnerability Scanning

5.3.1 OpenVAS

From test result in Figure 2, Dewey.xxxxx.ac.id has 4 high, 3 medium, 2 low, and 28 log vulnerabilities. While Www.xxxxx.ac.id has 7 high, 19 medium, 2 low, and 97 log vulnerabilities. Bakp.xxxxx.ac.id has 8 high, 19 medium, 2 low, 96 log vulnerabilities. The last one is Sim.xxxxx.ac.id has the most vulnerabilities with numbers 19 high, 16 medium, 2 low, and 29 log vulnerabilities.



Figure 2. Vulnerabilities Numbers Graph Based On OpenVAS Scan Results

Vulnerability	WWW	SIM	BAKP	DEWEY
OpenSSL	✓	✓	✓	✓
Apache modules	✓	✓	✓	✓
HTTP Test Method	✓	✓	✓	✓
SSL	✓	✓	✓	✓
WordPress	✓	✓	✓	✓
Apache File Listing	✓	✓	✓	✓
Search	✓	✓	✓	✓

Figure 3. Vulnerabilities Summary Table Based On OpenVAS Scan Results

Based on vulnerabilities summary which have been summarized on Figure 3, even Sim.xxxxx.ac.id has a lot of vulnerabilities number but those number mostly showing the same issue faced by this site, which means most issues such as

OpenSSL and Apache can just be updated to the latest version to fix the issue shown. While Www.xxxxx.ac.id and Bakp.xxxxx.ac.id both have variety vulnerability which increased possibilities to be attacked from those vulnerabilities.

5.3.2 Acunetix

Vulnerability scan result from www.xxxxx.ac.id shows 476 warnings with 0 high, 166 medium, 17 low and 293 informational level warnings. While Bakp.xxxxx.ac.id shows 565 warnings with 67 high, 223 medium, 15 low, and 260 informational warnings. Less warning produced from Dewey.xxxxx.ac.id site with total of 93 warnings consist of 31 high, 18 medium, 19 low, and 25 informational warnings. The last site Sim.xxxxx.ac.id shows the lowest of all with 5 high, 32 medium, 10 low, and 40 informational warnings with total of 87 warnings. Details of diagram can be shown in Figure 4.

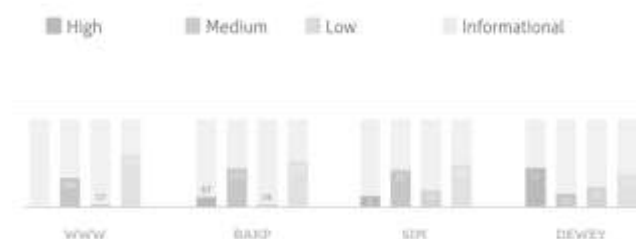


Figure 4. Vulnerabilities Numbers Graph Based On Acunetix WVS Scan Results

Vulnerability	WWW	SIM	BAKP	DEWEY
SQL Injection	✓	✓	✓	✓
404	✓	✓	✓	✓
SQL	✓	✓	✓	✓
Clickjacking	✓	✓	✓	✓
Cookies	✓	✓	✓	✓
Directory File Listing	✓	✓	✓	✓
Site Redirection	✓	✓	✓	✓

Figure 5. Vulnerabilities Summary Table Based On Acunetix WVS Scan Results

Based on scan summary results on Figure 5, each sites have identical vulnerabilities which means the sites can be attacked mostly using the same method such as DoS. To prevent those vulnerabilities summarized above, the server need to be reconfigured properly.

5.4 Analysis

5.4.1 Open VAS and Acunetix Web Vulnerability Scanner Scan Comparison

Both tools shows different scan results which tells how they check from different aspects. Open VAS focuses on external access to system which made this app inferior from Acunetix WVS when doing sites scan. The way Acunetix displays vulnerabilities scan result into a report needs to be praised because the program can limit how far the information should go when given to clients or programmers. However both software accuracy can't be assured since some of the method still rely on banner grabbing method.

These tools shows how a system is vulnerable but some still need to be proven through source code scan or configuration checkup to ensure these vulnerabilities are exists on system. And because of the limited access to system and its contents, this research can't go through detailed scan.

5.4.2 ID Serve and HTTPRecon Scan Comparison

HTTPRecon and ID Serve sometimes shows different result and there's a need to define which tools is better. Based on the testing method, ID Serve used only single method which is identifying server through its banner to identify the server whereas HTTPRecon uses fingerprinting method to compare server response with database to identify which is the most relevant version of server being used.

Banner-grabbing method is commonly used to identify servers, but nowadays to harden servers people reconfigure the banner identity to prevent further possibility of being attacked due to its' identity.

5.4.3 Problems Occurred During Penetration Testing

There are some factors which become limitation such as resource availability and time to test a site is too long (ie. Using Acunetix default scan profile might take weeks to finish a complex site) and might cause Denial of Service or the ISP might filter and block the connection between the tester and target sites because of the many requests given to sites tested.

Other problem mentioned is how PCU site not secured on some forms that tested which caused email spamming to lecturers and staffs on PCU while testing. This problem is caused because no captcha code exist on both resignation and deferral admission form. However after this event, programmers of PCU fixed this issue.

And to prevent further things happened, other testing needed such as password brute-forcing, DoS test and any testing was stopped.

5.4.4 Overall Security Test Results

System security for administration sites which tested in this research is categorized as not good, because there's no regular maintenance to system. From Acunetix security scan result, Sim.xxxxx.ac.id still has the best security amongst other site tested but there are need of some security patches to minimize vulnerabilities on system. Other sites that affected by SQL Injection and Cross Site Scripting need to be fixed soon because of mostly common attack that might be launched. Even though there are no access through system logs, it is suggested that every other sites not tested in this research need to be

evaluated thoroughly especially in the migration process of Single Sign On method that being implemented on most campus academic system. Denial of Service might also happen if servers not reconfigured properly.

Other than the vulnerability mentioned above, there is a possibility to have site information being leaked due to file listing not being restricted on sites servers.

6. REFERENCES

- [1] Hariwibowo, Dody. 2011. Keamanan Komputer | Pengantar Teknologi Informasi. 02 06. Accessed 10 21, 2014. <http://dhoddycreator.wordpress.com/makalah-pti/keamanan-komputer>.
- [2] Barnatt, Christopher. 2012. ExplainingComputer.com: Computer Security. 09 13. Accessed 10 20, 2014. <http://explainingcomputer.com/security.html>.
- [3] EC-Council. 2012. Certified Ethical Hacker v8 : Module 20 Penetration Testing. Amerika: EC-Council.
- [4] EC-Council. 2012. Certified Ethical Hacker v8 : Module 12 Hacking Webservers. Amerika: EC-Council.
- [5] Internet Corporation for Assigned Names and Numbers. n.d. WHOIS Primer | ICANN WHOIS. <http://whois.icann.org/en/primer>.
- [6] Computer Hope. n.d. Linux and Unix nslookup command help and examples. <http://www.computerhope.com/unix/unslooku.htm>.
- [7] Gibson, Steve. 2003. GRC | ID Serve - Internet Server Identification Utility. Oct 06. <https://www.grc.com/id/idserve.htm>.
- [8] OpenVAS. 2015. OpenVAS - About OpenVAS Software. <http://www.openvas.org/software.html>.
- [9] Acunetix. 2015. Web Application Security with Acunetix Web Vulnerability Scanner. <https://www.acunetix.com/vulnerability-scanner/>.

Characterization of Clay/Chitosan Nanocomposites and their Use for Adsorption On Mn(II) from Aqueous Solution

F. H. Abd El-Kader Department
Of Physics, Faculty of Science,
Cairo University, Giza
Egypt

A. M. Shehah
Department of Physics, Faculty
of Science, Cairo University,
Giza, Egypt

A.A. Bakr
Egyptian Petroleum
Research Institute
(Epri), Nasr City,
Cairo, Egypt

Omar T. Hussein
Department Of Physics,
Faculty of Science, Cairo
University, Giza, Egypt

Abstract: In this study, composites films were prepared from Chitosan biopolymer and Montmorillonite nanoclay (MMT) by dispersion of MMT into Chitosan solution with different weight percentage (2.5, 5, 7.5, 10, 12.5, 15 and 75% wt. /wt. nanoclay/chitosan), using both sonication and casting technique methods to obtain good dispersion of nanoclay. The structural properties of these nanocomposites samples examined by XRD and FTIR . The XRD patterns indicating that formation of an intercalated nanostructure as exfoliated and flocculated structure . Also the complexation of the dopant with the biopolymer was examined by FTIR studies. The experiments of Mn(II) ions adsorption were carried out on MMT/chitosan nanocomposites. The effect of various parameters such as pH, contact time, adsorption mass, initial Mn(II) concentration and temperature on the adsorption of Mn(II) removal onto MMT/chitosan nanocomposites was investigated. Two adsorption isotherm models were applied Freundlich and Langmuir to fit the experimental data. Langmuir isotherm modeling was suitable for description the data at equilibrium state. The kinetic isotherm was found to follow the pseudo-second-order model. Also, the thermodynamics parameters of the adsorption such as Gibbs free energy ΔG° , entropy ΔS° and enthalpy ΔH° were discussed and the results demonstrate that the adsorption process is spontaneous and endothermic.

Keywords: MMT/Chitosan; nanocomposites; XRD; IR; adsorption

1. INTRODUCTION

Recently, polymer/clay nanocomposites have attracted considerable interest because they combine the structure, physical and chemical properties of inorganic and organic materials. Most work with clay/polymer nanocomposites has concentrated on synthetic polymers, including thermosets such as epoxy polymers, and thermoplastics, such as polyethylene, polypropylene, nylon and poly (ethylene terephthalate) [1]. However, the opportunity to combine at nanometric level clays and natural polymers (biopolymers), such as chitosan, appears as an attractive way to modify some of the properties of this polysaccharide including its mechanical and thermal behavior, solubility and swelling properties, antimicrobial activity, bioadhesion, etc. [2].

Clay/Chitosan nanocomposites are economically interesting because they are easy to prepare and involve inexpensive chemical reagents. Chitosan, obtained from chitin, is a relatively inexpensive material because chitin is the second most abundant polymer in nature, next to cellulose [3]. In the same way, clays are abundant and low-cost natural materials. In addition, the successful preparation of the nanocomposites still encounters problems, mainly related to the proper dispersion of nano-fillers within the polymer matrix.

The degree of acetylation (DA) and the crystallinity of chitin molecules affect the solubility in common solvents. Reducing the acetylation level in Chitosan ensures the presence of free amino groups, which can be easily protonated in an acid environment, making Chitosan water soluble below pH about 6.5 [4, 5]. In acid conditions, when the amino groups are protonated Fig. (1), chitosan becomes a soluble polycation [6]. The presence of amino groups makes chitosan a cationic polyelectrolyte.

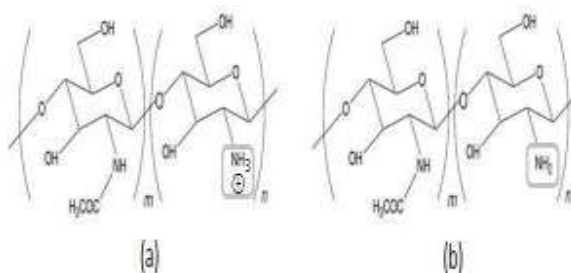


Fig. 1: Schematic illustration of chitosan: (a) at low pH (less than about 6.5), chitosan's amine groups become protonated (polycation); (b) at higher pH (above about 6.5), chitosan's amine groups are deprotonated and reactive.

Clays are classified on the basis of their crystal structure and the amount of the distributed electric charge and their location (deficit or excess) per unit cell. Crystalline clays range from kaolins, which are relatively uniform in chemical composition, to smectites, which vary in their composition, cation exchange properties, and ability to expand. The most commonly employed smectite clay for the preparation of polymeric nanocomposites is bentonite, whose main mineral component is Montmorillonite (MMT) [7]. Montmorillonite (MMT) is a 2:1 layered hydrated aluminosilicate, with a triple-sheet sandwich structure consisting of a central, hydrous alumina octahedral sheet, bonded to two silica tetrahedral sheets by shared oxygen ions as in Fig (2). Isomorphic substitution of Al^{+3} in the octahedral sheets by Mg^{+2} (less commonly Fe^{+3} , Mn^{+2} , and other) and, less frequently, of Si^{+4} by Al^{+3} in the tetrahedral sheet, results in a net negative charge on the crystalline layer, which is compensated by the presence of cations, such as Na^+ , K^+ , Ca^{+2} , or Mg^{+2} , sorbet between the layers and surrounding the edges. An idealized MMT has 0.67 units of negative charge per unit cell, in other words, it behaves as a weak acid. These loosely held cations do not belong to the crystal structure and can be readily exchanged by other cations, organic or inorganic.

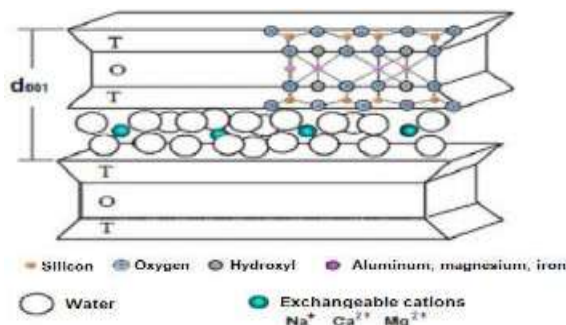


Fig. 2: Schematic of a Montmorillonite, layered clay mineral with a triple-sheet sandwich structure consisting of a central, hydrous alumina octahedral sheet(O), bonded to two silica tetrahedral sheets (T) by shared oxygen's

The system of the Chitosan as a matrix for the nanoclay (MMT) promising as enhancement adsorptive removal of heavy metal ions, quite efficient and fast adsorption, since, it is a perfect nano adsorbents because it has high specific area and there is not any internal diffusion resistance, so after studying the physical properties of this system, we looked for using this system in adsorption process for heavy metal ions such as Manganese (II).

Our target of these paper was the preparation of the biopolymer Chitosan as a matrix of nanoparticles MMT with different percentage ratios of the nanoclay to obtain new composites of specific physical property, as well as, using this system for adsorption the heavy metal ions under equilibrium isotherm modeling and obtaining its thermodynamics characteristics.

2. MATERIALS AND METHODS

2.1. Material

Commercially available chitosan powder (Sigma Aldrich) was used. According to the producer data, its deacetylation

degree DD was about 80%. Structural formula of Chitosan is presented in fig. (1), commercially available MMT (Sigma Aldrich) with average particle size 10-30 nm was used as a nano-filler.

Manganese chloride with purity of 99.9% ($MnCl_2 \cdot 4H_2O$) was purchased from Loba Chemie. Co.

2.2. Film preparation

Pure Chitosan film: The appropriate weight of biopolymer Chitosan (1gm) was dissolved in 100 ml of DI water and 2% acidic acid. The mixture was magnetically stirred continuously and heat ($80^\circ C$) for 4 hours, until the solution mixture becomes a homogenous viscous solution. The solution is poured into Petri dish and left for 3 days to solidify at room temperature. The thickness of the final film was about ($50\mu m$).

Clay/Chitosan nanocomposites: Different weights percentage of Clay nanoparticles were added to water and magnetically stirred vigorously for 3 hours and sonicated (by using 450 sonifier) for 1 hour to prevent the nanoparticles agglomeration. Each weight percentage of sonicated nanoclay was added to Chitosan viscous solution of the corresponding weight and magnetically stirred for 2 hours then sonicated again for 1 hour to get good dispersion without agglomeration as possible. The final nanoclay/chitosan mixture was cast in glass Petri dish; air bubbles were removed by shaking and blowing air and were left until dry. This procedure was repeated to make (2.5%, 5%, 7.5, 10%, 12.5% and 15% Nanoclay/Chitosan composites). The films were about $50\mu m$ in thickness. The thicknesses of films were controlled by using the same amount of total materials and the same glass Petri dish size. It is important to mention that we prepared the nanocomposites sample of highly ratio of the nanoclay with chitosan to obtain the optimum composite film to achieve maximum adsorption of manganese (II) as heavy metal ions, as well as seen in the discussion of the adsorption process nextly.

2.3. Characterization of the composites film

X-ray diffraction patterns were obtained using advanced refraction system XRD Scintag Ins., USA. The tube used was Copper radiation and the filter was Nickel. The range of x-ray spectra of 2θ was over the range $5-70^\circ$.

The infrared spectral analysis (IR) of the samples was carried out using PYE Unicam spectrophotometer over the range $500-4000\text{ cm}^{-1}$.

2.4. Adsorption method

The manganese $Mn(II)$ stock solution concentration of 150 mg/L was prepared by dissolving Manganese chloride ($MnCl_2 \cdot 4H_2O$, Loba chemie) in distilled water. The working $Mn(II)$ solution concentration ranging from 20 to 80 mg/L for all experiments was freshly prepared from the stock solution. Standard acid (0.01M HNO_3) and base solutions (0.125M NaOH) were used for pH adjustments at pH 3, 4, 4.5, 5, 5.5, 6, 7, 8 and 9. The pH of the solution was measured with a pH meter (Thermo Orion 5 Star)

The experiments for removal of manganese ions from dilute aqueous solutions by the addition of adsorbent (chitosan/clay) masses 0.10, 0.15, 0.20, 0.25, 0.30, 0.35 and 0.40 g/L were carried out at different temperatures (298, 308 and 318k). After continuous stirring over a magnetic stirrer at about 160 rpm for a predetermined time intervals (15, 30, 45, 60, 75, 90 and 105min), the solid and solution were separated by centrifugation at 3000 rpm for 15 min and slightly dried at ambient temperature. Mn(II) concentration was determined by Spectro-photometer, LaMotte, model SMART Spectro, USA and the solid phase was analyzed. The contact time, allows the dispersion of adsorbent and metal ions to reach equilibrium conditions, as found during preliminary experiments.

3. RESULT AND DISCUSSION

3.1. X-ray diffraction (XRD)

X-Ray diffraction is an advanced technique to understand the Skelton structure in semicrystalline polymers or clay minerals and these composites (organoclay). The XRD analysis was used to study the crystallinity and the structural change of the prepared samples as in fig. (3-1a) of the pure chitosan that indicates the peaks at around $2\theta \approx 10^\circ$, 20° and 23° confirm the semicrystalline nature of Chitosan. This result is consistent with that found in previous literature^[8,9]. The peaks over the range from 10° to 20° for Chitosan films showed that it could exist in two distinct crystal form I and II. This morphological structure varying from spherical to rods depending on the film processing condition. It is worthy to mention that the molecules does not affect the crystal form but does affect the crystallite size and morphological character (rod or spherulite) of the cast film. Also different solvent treatment enhance spherulite structure. The evaluation of form I related to crystal form of $a = 7.76 \text{ \AA}$, $b = 10.19 \text{ \AA}$, $c = 10.3 \text{ \AA}$ and $\beta = 90^\circ$ i.e. it is orthorhombic unit cell with two monomer units per repeat along the chain axis while form II related to crystal of $a = 4.4 \text{ \AA}$, $b = 10 \text{ \AA}$, $c = 10.3 \text{ \AA}$ and $\beta = 90^\circ$ ^[8]. Fig. (3-1b) shows typically XRD of MMT that characterized by peak at $2\theta = 8, 19.8, 20.8, 26.5,$ and 45.5° of highest relative intensity respectively nano clay as found previously^[10]. Many numbers of researchers were interesting to study the XRD of the clay at specific peak at 2θ around 7° corresponding to a basal spacing d_{001} ranging from $12 - 14 \text{ \AA}$.

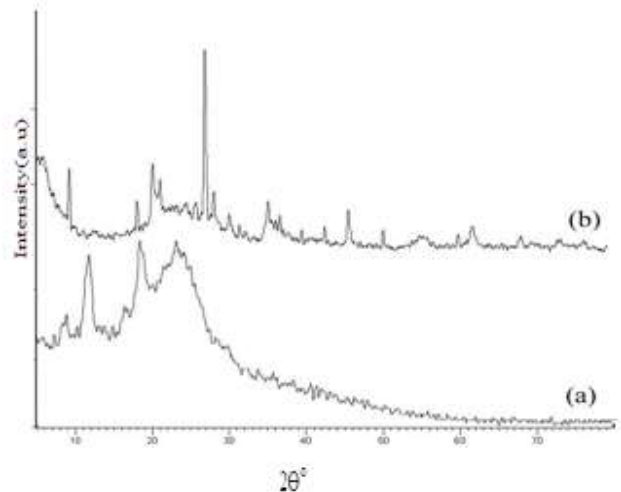


Fig. 3-1: X-ray diffraction pattern of (a) Pure Chitosan (b) Pure MMT.

The nanoclay dispersion within chitosan at different level of weight percentage for the composite samples has been characterized by XRD as in fig. (3-2). The XRD ranging up to $2\theta \approx 10$ to 25° sharing for both chitosan and nanoclay is quite different than that observed for XRD of the both two starting materials indicating the occurred complexation between chitosan and the nanoclay. This gives an evidence reason for taking inconsideration the changes occurred for the typical diffraction peak bellowing to MMT around $2\theta \approx 7^\circ$ to look for the structural changes occurred in the composites of the different levels of weight ratio^[11].

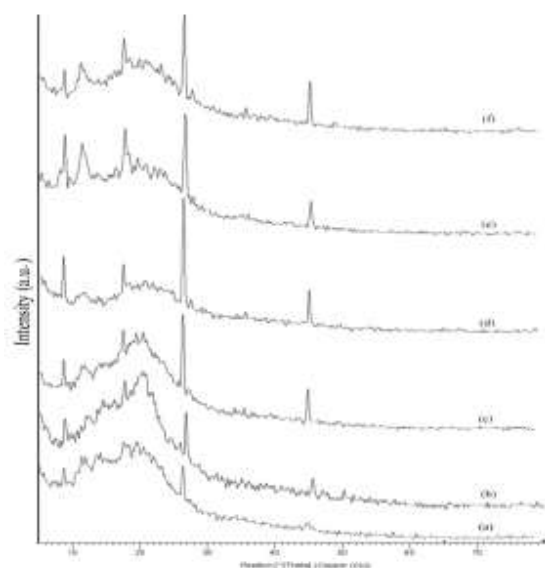


Fig. 3-2: X-ray diffraction patterns of (a) 2.5% (b) 5% (c) 7.5% (d) 10% (e) 12.5% (f) 15%.

Is well known that there are three types of the polymers layer silicate interaction possible to be occurred according to the relative distribution dispersion of the stacks of nanoclay particles in the biopolymers dissolved in water with acidic media [12, 13].

a. Phase separated structure :

When the organic polymer is interact with the inorganic clay and the polymer is unable to intercalate within the clay layers and the clay is dispersed as aggregate or particles with layers stacked together within the polymer matrix. The obtained composite structure is considered as phase separated.

b. Intercalated structure :

When one or more polymer chain are inserted into the interlayer space and cause to the increasing of the interlayer spacing, but the periodic array of the clay is still exist, the intercalated nanocomposites is formed. The presence of polymers chain in the galleries cause to the decreasing of the electrostatic force between the layers but is not totally dissolved. A well – ordered multilayers morphology built up with high interference interactions consisted of polymer chain and clay layer.

c. Exfoliated (Delaminated) structure :

This structure is obtained as the insertion of polymer chain into the clay galleries causes the separation of the layers one another and individual layers are dispersed within the polymer matrix. The exfoliated structure is occurred when the increasing of the inter layer spacing become more than 8 – 10 nm. Due to the well dispersion of the individual clay layer, high aspect ratio is obtained and lower clay content is needed for exfoliated nanocomposites. At that state a most significant improvement in polymers properties is obtained due to the large surface interaction between polymer and nanoclay.

Chitosan has good miscibility with the nanoclay (MMT) due to its hydrophilic and poly cationic properties in acidic media and can easily intercalate into the interlayers by means of cationic exchange. In our case, the specific reflection peak of d_{001} is detected at $2\theta = 8^\circ$ and the movement of the basal d_{001} of MMT were to higher angle because the prepared composite samples were in direction of increasing the percentage ratio of the nanoclay. The proper of the three types of interaction are available according to the ratio of the nanoclay and the chitosan.

The movement of the specific diffraction peak of MMT indicates formation of the flocculated-intercalated structure in the composites of the different percentage of the nanoclay-biopolymers under studying. This structure is due to the hydroxylated edge-edge interaction of the silicate layers [14], in addition to the electrostatic interaction of the amino groups in chitosan to adhere the negatively charge surface of the inter layers in nanoclay. Also the change of the intensity of the XRD confirms the new structural of the composite samples. Finally from fig. (3-3), it is possible to expect the

formation of an intercalated nanostructure as exfoliated and flocculated structure [12, 13].

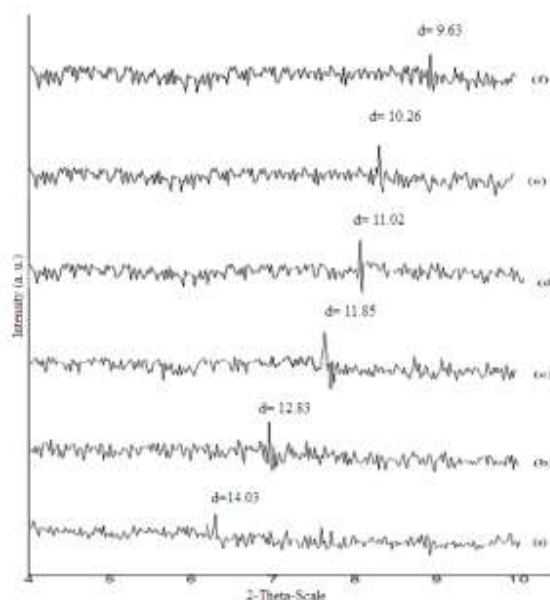


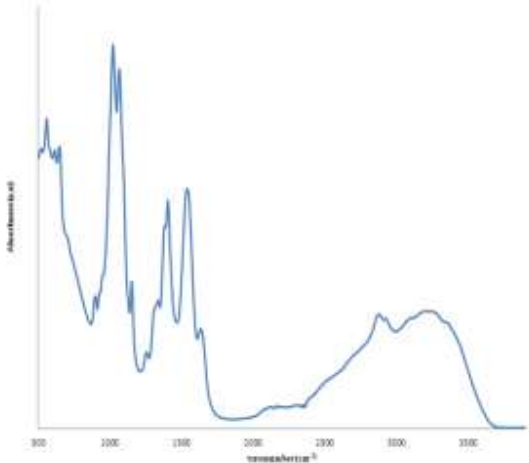
Fig. 3-3: The movement of the d-spacing for d_{001} of the (a) 2.5%, (b) 5%, (c) 7.5%, (d) 10%, (e) 12.5%, and (f) 15% nanoclay/chitosan composite films.

3.2. FTIR spectroscopy

Infrared absorption spectroscopy can be employed in quantitative analysis and structure determination of the compounds. Fig. (4) depicts characteristic bonds of the pure Chitosan as recorded. The main absorption bands at 3750 to 3000 cm^{-1} are due to the stretching vibration of O-H groups that overlapped to the stretching vibration of N-H band while the two absorption stretching band of C-H band in C-H_2 appear at $\nu_1 = 2921 \text{ cm}^{-1}$ and in CH_3 at $\nu_2 = 2875 \text{ cm}^{-1}$ respectively. The bending vibration of methylene and methyl groups were also visible at $\nu = 1377$ and $\nu = 1429 \text{ cm}^{-1}$ [14]. It is well known for Chitosan that the absorption range from 1680 to 1480 cm^{-1} was related to the vibration of the carbonyl bands C=O of the amide group CONHR as characteristic absorption bands [15]. It is worth to mention that the vibration of the amine group NH_2 is observed at $\approx 1580 \text{ cm}^{-1}$.

The amide I group is observed at $\nu_1 = 1646 \text{ cm}^{-1}$ while the vibration C=O of the protonated amine group (NH_3) is visible at $\nu_2 = 1540 \text{ cm}^{-1}$ that presented the amide II. The characteristic band of amide III is observed at 1255 cm^{-1} . The amide I and amide II absorption bands suggest that Chitosan is a partially deacetylated product [16]. It is well known that the reducing of the acetylation level in Chitosan ensure the presence of the free amino groups which can be easily protonated in an acid environment making Chitosan water soluble. The presence of the amino groups makes Chitosan a cationic polyelectrolyte. Also the absorption in the range of 1160 cm^{-1} to 1000 cm^{-1} has been attributed to vibrations of the CO group [16]. The band at $\nu = 1153 \text{ cm}^{-1}$ is due to C-O asymmetric vibration in the oxygen bridge

resulting from deacetylation of chitosan. The bands near 1080 to 1021 are attributed to ν_{CO} of the ring COH, COC and CH₂OH. The small peak at 894 cm⁻¹ is corresponding to the wagging (C-H) of the saccharide structure of Chitosan [17, 18,

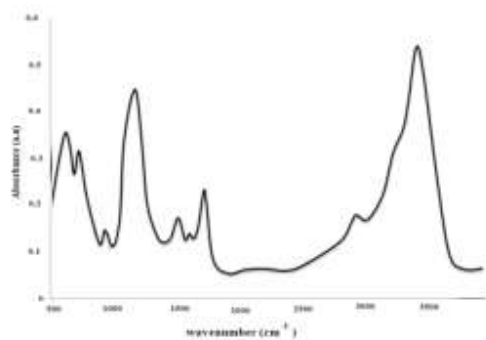


19].

Fig. 4: IR spectrum of pure chitosan film.

Consequently the I.R. of the pure Clay is illustrated in fig (5) where the vibration bands at 3648 cm⁻¹ is due to O-H stretching vibration and at 3449 cm⁻¹ referred to interlayer and interlayer H bonded O-H stretching. Also the band at 1650 cm⁻¹ is corresponding to the deformation bending vibration for H-OH. The stretching vibrational mode that observed at 1173 cm⁻¹, 1113 cm⁻¹, 1033 cm⁻¹ are certainly different vibrational mode of Si-O (such as stretching of quartz, longitudinal mode and normal stretching mode) [20].

The Al-Al-OH deformation vibrational mode is found at 928 cm⁻¹, while for Al-Fe-OH and Al-Mg-OH deformation mode are at 886 and 849 cm⁻¹ respectively [17]. The observed band at 797.4 cm⁻¹ is due to Si-O stretching vibration of quartz and silica as well as the Si-O stretching only of quartz at 774 i.e. we have diagnostic band of quartz as doublet at 797 and 774 cm⁻¹. Also we have doublet diagnostic bands for Si-O at 699 and at 1033 (normal stretching mode of quartz)



as mentioned above [21, 22].

fig. 5: I.R. spectrum of pure nanoclay (MMT).

The band at 624 cm⁻¹ mentioned to the coupled Al-O and Si-O vibration mode out of plane. The final bands at 525 cm⁻¹ and 468 cm⁻¹ that out of our scale are due to Al-O-Si and Si-O-Si deformation vibrational mode respectively [21].

The interaction between nanoclay particles and the polymers matrix significantly depends upon the hydroxyl groups and charges present in the nanoclay layers.

Accordingly as one pay an attention to fig. (6) that indicates the I.R. of the composites samples at different ratio of loading the nanoclay in the matrix of the chitosan biopolymer, one find that the O-H stretching frequencies of the composites in range 3000 cm⁻¹ to 3750 cm⁻¹ were broadened and displaced to lower frequencies by about 10 cm⁻¹ as well as the intensities of that absorption bands decrease dramatically to insure the formation of the hydrogen bonds in the all different composites.

Dissolution of Chitosan in the acetic acid resulted in reaction between an amino group of Chitosan and the acetic acid residue which lead to formation of amino acetic group (as NH₃⁺ AC⁻). The addition of the nanoclay as filler to the liquid system of Chitosan/CH₃COOH facilitated formation of hydrogen bonds [13, 23]. Also one may supposed that the amino groups of chitosan were exposed on the surface of the nanocomposites material which can be observed at 1250 to 1405 cm⁻¹ so that the soluble parts of the biopolymer chitosan containing OH and NH₂ may form hydrogen bonds with Si-O-Si groups of the silicate layer of the nanoclay (MMT). In addition, the intensities of Al-O vibration bands at 914, 839, 796 and 624 cm⁻¹ and the structural O-H stretching vibration are decreasing by increasing the loading filler of the nanoclay. This attributed to the relaxation of the hydrogen bonding between (Al-O)OH deformation as well as the hydrated water of exchangeable cationic metal ions on the nanoclay surface [24].

The amide I band at 1646 cm⁻¹ of chitosan may be overlapped with δ_{HOH} bending vibration band at 1628 cm⁻¹ of the water molecule associated to the starting clay as expected for the biopolymers with high water retention capability [25]. On the other hand the original bands of Chitosan component at 1540 cm⁻¹ for the amide II gave a great evidence for the interaction between Chitosan and the nanoclay particles, since the -NH₃⁺ group interact electro statically with negative charged sites of the clay. This frequency of the vibration mode 1540 cm⁻¹ as in the starting chitosan corresponding to the deformation of vibration δ_{NH3} of the protonated amino group is shifted gradually towards higher frequency values. The displacement of the vibration δ_{NH3} is depending on the loading ratio of the clay nanoparticles in the host matrix of the chitosan. At the same time one can observe a high decreasing in the intensity of this absorption band. This fact can be related to the electrostatic interaction between such groups and the negatively charged sites in the clay structure expressing the stronger interaction between cationic chitosan molecules and anionic clay surface nanoparticles [25]. Both result of X-ray diffraction and I.R. support each other indicating complexation of chitosan with nano MMT.

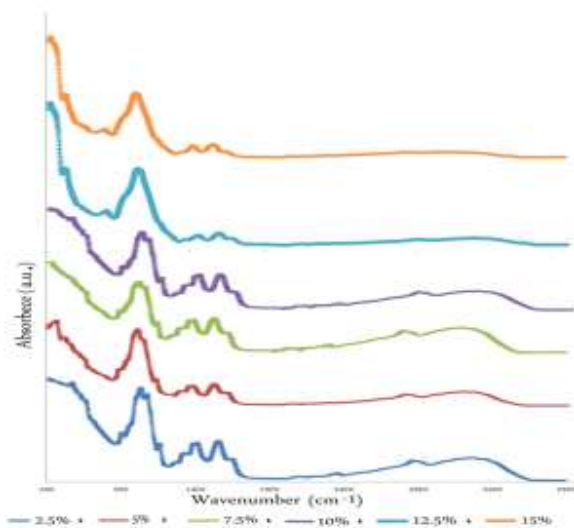


Fig. 6: IR Spectra of (2.5, 5, 7.5, 10, 12.5 and 15%).

3.3. ADSORPTION PROCESS

Montmorillonite (MMT) nanoclay has a negative net surface charge and has little or no affinity to anionic, in there; Chitosan a nature biopolymeric cation is an extent candidate to modify MMT for adsorption especially when we obtain composite thin film with good mechanical property.

Since the phenomenon of adsorption is largely depend on surface area and the pore structure , a composite thin film of nanoclay/chitosan is expected to achieve good condition for the adsorption of the heavy metal ions from the groundwater

Many attempts had been carried out in order to find the best film ratio of nanoclay/chitosan for enhancing the adsorption process, finally we found the composite films of highly percentage of the nanoclay such as 70:30, 75:25 and 80:20 were better than the less other selective ratios.

The percentage of the nanoclay more than 80% were brittle not a suitable to achieve good adsorption.

We choice the composite 75:25 because it was the optimum composite ratio achieving the highest adsorption of heavy metal ions as Manganese at the different conditions of adsorption such as pH, contact time, temperature and initial concentration.

3.4. ADSORPTION CALCULATION

The amount of adsorption q_e (mg/g) and the percentage of removal were calculated by the following equations [26]:

$$q_e = \frac{V(C_0 - C_e)}{m} \quad (1)$$

$$\text{Adsorption (\%)} = \frac{(C_0 - C_e)}{C_0} \times 100 \quad (2)$$

Where C_0 and C_e are the initial Mn(II) concentration and the concentration at equilibrium in mg/l, m is the mass of the adsorbent and V is the volume of solution.

Two adsorption isotherms models have been used to analyze the adsorption data equilibrium models to fit the experimental data by two equations [27]:

(i) Langmuir

$$\frac{C_e}{q_e} = \frac{1}{K_L b} + \frac{C_e}{b} \quad (3)$$

Where q_e (mg/g) is the equilibrium adsorption capacity and C_e (mg/l) is the equilibrium concentration. While, K_L (l/mg) and b (mg/g) are the Langmuir constants related to the sorption capacity and the adsorption energy, respectively.

(ii) Freundlich

$$\log q_e = \log K_f + \frac{1}{n} \log C_e \quad (4)$$

While, K_F (L/mg) is the Freundlich constant and $1/n$ is the heterogeneity factor.

Adsorption kinetics is used to explain the adsorption mechanism and adsorption characteristics. The pseudo-first-order and second-order kinetics equations [28, 29] in linear forms are expressed as:

$$\log(q_e - q_t) = \log(q_e) - \left(\frac{k_1}{2.303}\right)t \quad (5)$$

$$\frac{t}{q_t} = \frac{1}{(k_2 q_e^2)} + \left(\frac{1}{q_e}\right) t \quad (6)$$

Where q_t and q_e are the amounts of nano-composite material adsorbed at time t and at equilibrium, respectively; k_1 and k_2 are the pseudo-first-order and second-order rate constants for the adsorption process.

The thermodynamic parameters provide in-depth information on inherent energetic changes including Gibbs free energy change (ΔG°), enthalpy change (ΔH°), and entropy change (ΔS°) for the adsorption process which are obtained by the following equations [30, 31]:

$$\Delta G^\circ = -RT \ln b \quad (7)$$

$$\ln b = \frac{\Delta S^\circ}{R} - \frac{\Delta H^\circ}{RT} \quad (8)$$

Where R is the ideal gas constant ($\text{kJ mol}^{-1} \text{K}^{-1}$), T is the temperature (K), and b is a Langmuir constant related to the adsorption energy (from the Langmuir isotherm).

3.4.1. Effect of starting solution pH on the removal of Mn(II)

The effect of starting solution pH on the removal % of Mn(II) from solutions with an initial concentrations of 80 mg/L, on 0.25 g/L of adsorbent after 105 minutes is shown in Fig.(7). The data indicate that the amounts of Mn(II) adsorbed on the prepared clay/chitosan composite material decrease with decreasing pH for a starting solution $\text{pH} \leq 5$. These phenomenon can be explain by the presence of H^+ ions in to the solution were competing with the Mn(II) ions for active binding sites on the surface of the composite .

Fewer binding sites were available for Mn(II) cation to be adsorbed, in addition the most amine groups in chitosan become protonated NH^{+3} at lower pH which reduce the available binding sites for Mn(II) ions.

As Mn(II) transported from the solution to the adsorbent the protonated amino groups inhibit the approach of Mn(II) due to the electrostatic repulsion force exerted by NH^{+3} on the adsorbent surface^[32].

When pH increase to 5.5 the amino groups become deprotonated hence it is free to interact and bind with Mn(II) ions, however, pH range of 5 to 6 was optimum for Mn(II) to be adsorbed by the nanoclay/chitosan composite film 75:25, at pH higher than 6 the cumulative effect of adsorption and perception of the ions may be occurred.

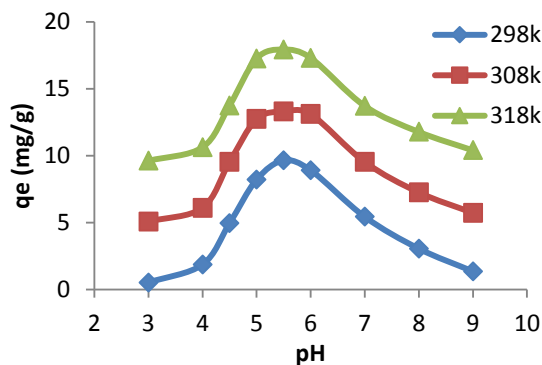


Fig.7: Effect of pH values on the adsorption capacity of Mn (II) at different temperatures onto Chitosan/Clay ratio 25:75 (initial concentration of 80 mg/L, adsorbent dosage of 0.25 g/L, stirring rate of 160rpm, contact time of 105 min).

3.4.2. ADSORBENT MASS

Different amounts of Chitosan/Clay composite materials (0.10, 0.15, 0.20, 0.25, 0.30, 0.35 and 0.40 g/L) were added to a series of 100mL of manganese solutions with initial concentration of 80 mg/L at pH 5.5 and stirring rate of 160 rpm for contact time 105min to reach the equilibrium. Then the aqueous samples were filtered, and the residual Mn(II) concentrations were analyzed by Spectrophotometer. The effect of the adsorbent mass on the Mn(II) adsorption in 80 mg/L solutions is shown in Fig.(8)

At all temperatures, the first removal percentage of Mn(II) decreased with increasing the composite dosage up to dose above 0.2 g/L [33].

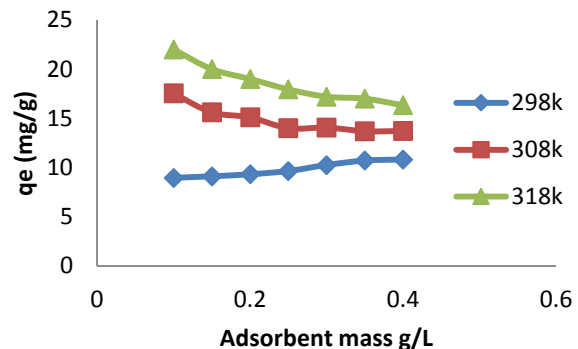


Fig. 8: Effect of adsorbent mass on the adsorption capacity of Mn (II) at different temperatures onto Chitosan/Clay ratio of 25:75 (initial concentration of 80 mg/L, pH value of 5.5, stirring rate of 160rpm, contact time of 105 min).

3.4.3. Initial Mn(II) concentration and adsorption isotherm

The effect of different Mn(II) concentrations determined after experimental studies were carried out for a range of metal concentrations (20-80 mg/L). A definite dosage of Clay/Chitosan composite materials (0.25g/L) was added to a series of 100mL of Mn(II) solutions with the different initial concentrations of 20, 30, 40, 50, 60, 70 and 80 mg/L at pH 5.5, and stirring rate at 160 rpm for contact time 105 min to reach the equilibrium. The removal of Mn(II) shown in Fig.(9) indicates that all ratios of Clay/Chitosan composite materials apparently remove a considerable amount of Mn(II) from the aqueous solutions. The adsorption efficiency for the composite ratio increases to a certain level (40 mg/L), and saturates beyond a certain concentration. Saturation resulted when no more metal ions could be adsorbed on the surface of the composites where the adsorption occurred. The removal with initial Mn(II) concentrations exhibit that the removal amounts are linearly proportional to the initial metal concentrations. However, the complete removal of Mn(II) was observed at initial concentration 20 mg/L at 308k and at initial concentrations 20 and 30 mg/L at 318k.

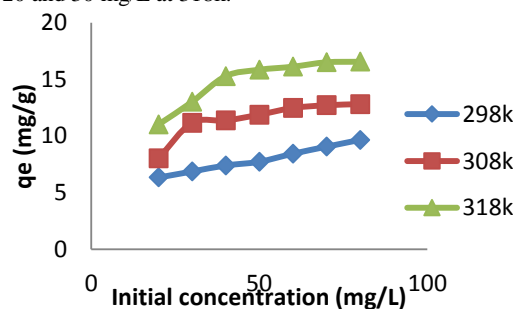


Fig. 9: Effect of initial Mn(II) concentration on the adsorption capacity at different temperatures onto Chitosan/Clay ratio of 5:75 (adsorbent dosage of 0.25g/L, pH value of 5.5, stirring rate of 160rpm, contact time of 105 min).

For better understanding of the mechanism of manganese adsorption was illustrated by adsorption kinetics. When the pseudo-second-order model considers the rate-limiting step as the formation chemisorptive bond involving sharing or exchange of electrons between adsorbate and the adsorbent [34], the above results obtained consistently suggests that the rate-determining step may be chemical adsorption and the adsorption behavior may involve the valence forces through sharing electrons between the Mn(II) ions and adsorbents [35, 36].

3.4.4. Contact time and adsorption kinetics

Fig.(10) shows the effect of contact time on the adsorption capacity of initial Mn(II) concentration (80 mg/L) onto Clay/Chitosan composite materials of ratio 75:25 (0.25 g/L) at pH 5.5, stirring rate of 160rpm and different temperatures, 298, 308 and 318k°. The fast Mn(II) removal rate in the beginning (within the first 60 minutes) is attributed to the rapid diffusion of Mn(II) from the solution to the external surfaces of adsorbent. The subsequent slow adsorption process is attributed to the longer diffusion range of Mn(II) into the inner-layers of Clay/Chitosan composite materials. Such slow diffusion will lead to a slow increase in the adsorption curve at later stages.

From Fig. (10), the adsorption rate increased with increasing the temperature and the concentration gradients becomes reduced as the time proceeds, owing to the accumulation of more than 12.5 mg of Mn(II) adsorbed per gram of Clay/Chitosan composite surface sites of ratio 75:25 after 60 min at temperature 318k, leading to the maximum adsorption capacity 17.92 mg/g after 105 min.

The increase in the amount of Mn(II) adsorbed at equilibrium with increasing the temperature may be due to the acceleration of some original slow adsorption steps or the creation of some active sites on the adsorbent surface. Increasing the temperature may also produce a swelling effect within the internal structure of the clay/chitosan composite, enabling a large number of Mn(II) ions to penetrate in to the pores. The adsorption process may involve chemical bonds and ion exchange since the temperature is the main parameter effecting the above two process [37].

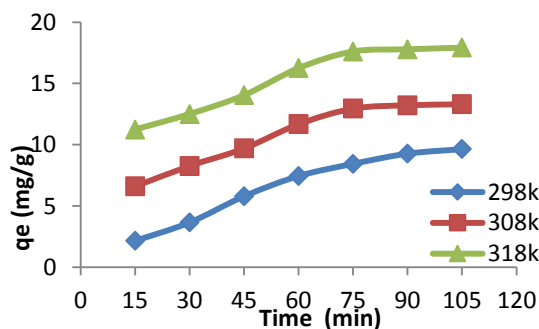


Fig. 10: Effect of contact time on the adsorption capacity of Mn(II) at different temperatures onto Chitosan/Clay ratio of 25:75 (initial concentration 80mg/l, pH 5.5, adsorbent mass 0.25g/l, stirring rate 160rpm).

3.5. Kinetic Isotherm

3.5.1. Pseudo-first and pseudo-second-order

To evaluate the adsorption kinetics of Mn(II) ions on Clay/Chitosan composite, the pseudo-first-order and pseudo-second-order models (Equations 5 and 6) were applied to analyze the experimental data. The kinetic parameters were obtained from fitting results and presented in Table (1). From the fit curve shown in Figs (11, 12) and the relative coefficient, it can be seen that the pseudo-second-order model fit the adsorption of Mn(II) onto Clay/Chitosan composite better than the pseudo-first-order model.

In this study, as illustrated in Figs (11, 12), the slopes and intercepts of the plot of t versus $\log(q_e - q_t)$ and t/q_t were used to determine the rate constants k_1 and k_2 and the equilibrium adsorption density q_e of the pseudo-first-order and pseudo-second-order, respectively, Table (1). The correlation coefficient for the pseudo-first-order model of Clay/Chitosan ratio of 75:25 ($R^2=0.942$) was lower than that of the pseudo-second-order ($R^2=0.990$) at 318k°, respectively. This suggests that the pseudo-first-order equation may not be sufficient to depict the kinetics of Mn(II) onto the Clay/Chitosan composites hence it appear that, the system under consideration is more appropriately described by pseudo-second-order mode which based on the assumption that the rate limiting step may be chemical sorption involving valency forces through sharing or exchange of electrons between sorbent and sorbate[38].

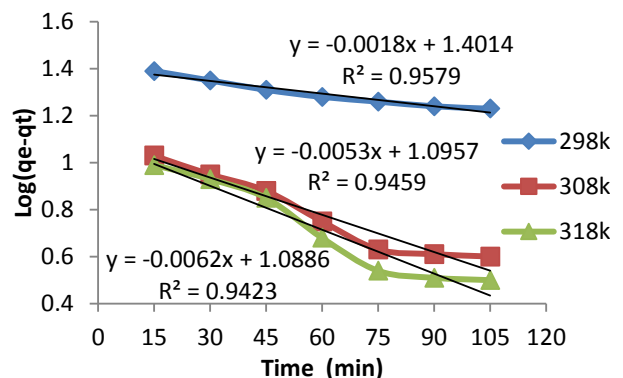


Fig. 11: Adsorption kinetics of the pseudo-first-order model for the Mn(II) adsorption of Chitosan/Clay ratio of 25:75 at different temperatures (adsorbent dosage of 0.25g/L, pH value of 5.5, stirring rate of 160rpm, contact time of 105min).

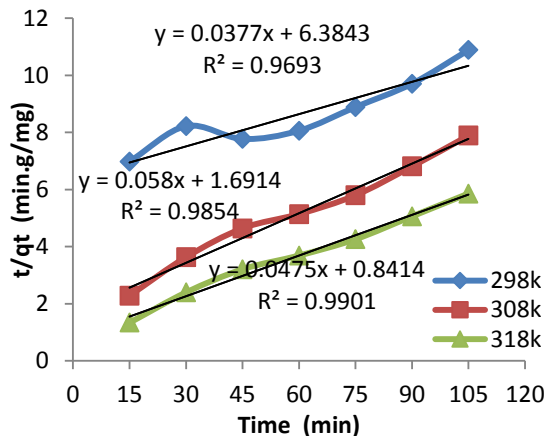


Fig.12: Adsorption kinetics of the pseudo-second-order model for the Mn(II) adsorption of Chitosan/Clay ratio of 25:75 at different temperatures (adsorbent dosage of 0.25g/L, pH value of 5.5, stirring rate of 160rpm, contact time of 105min).

Table (1): Kinetic parameters of the pseudo-first- and pseudo-second-order models for the Mn(II) adsorption at different temperatures onto Clay/Chitosan ratio of 75:25 (initial Mn(II) concentration 80mg/l, pH 5.5, adsorbent mass 0.25g/l, stirring rate 160rpm).

Pseudo-first-order model			
T (k)	K ₁ (min ⁻¹)	q _e (mg/g)	R ²
298	4.15×10 ⁻³	25.2	0.958
308	0.012	12.47	0.946
318	0.014	12.26	0.942
Pseudo-second-order model			
T (k)	K ₂ (g·mg ⁻¹ Lmin ⁻¹)	q _e (mg/g)	R ²
298	2.23×10 ⁻³	26.53	0.969
308	1.99×10 ⁻³	17.24	0.985
318	2.68×10 ⁻³	21.05	0.990

3.5.2. Langmaur and Freudlich isotherm

Adsorption isotherm models are usually used to describe the interaction between the adsorbent and the adsorbate at equilibrium state. The equilibrium data were analyzed using the Langmuir and Freundlich equilibrium models in order to obtain the best fitting isotherm (Equations 3 and 4).

According to Fig.(13), K_F and n are the Freundlich constants, which represent sorption capacity and sorption intensity, respectively and they can be evaluated from the intercept and slope of the linear plot of log q_e versus log C_e and given in Table(2). While, from Fig.(14), a line was obtained as the values of b and k_L can also be obtained by the slope and intercept of the line and given in Table(2).

The isotherm models of Mn(II) removal were studied by different initial concentrations ranging from 20 to 80 mg/L at different temperatures, 298, 308 and 318k^o, a pH of 5.5, adsorbent mass of 0.25 g and after 105 min. Table(2) summarizes the Langmuir and Freundlich constants and the calculated coefficients. The results show that the linear correlation coefficients for Langmuir models at higher temperature (318k^o) onto Clay/Chitosan composite materials of ratio75:25was 0.994, while the correlation coefficients for Freundlich models was 0.778. The higher regression coefficient R² for Langmuir model indicated that the Langmuir model fits the experimental data better than the Freundlich one. Moreover, the Langmuir constant b value, which is a measure of the monolayer adsorption capacity of the adsorbent, and the Langmuir constant, k_L, which denotes adsorption energy, were found to be17.83mg/g and 0.9 L/mg respectively at temperature 318k^o which are greater than the other value at temperature 298 or 308k^o.

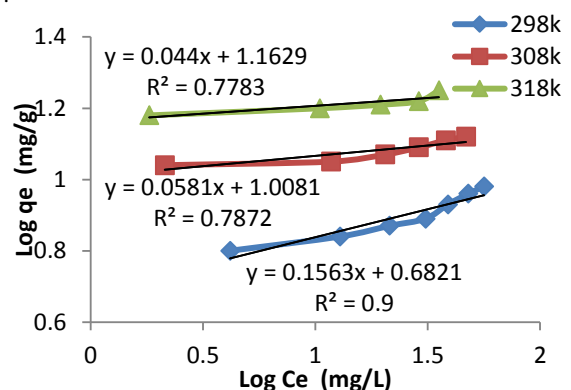


Fig. 13: Freundlich adsorption isotherm models for the removal of Mn(II) at different temperatures onto Chitosan/Clay ratio of 25:75 (adsorbent dosage of 0.25g/L, pH value of 5.5, stirring rate of 160rpm, contact time of 105 min).

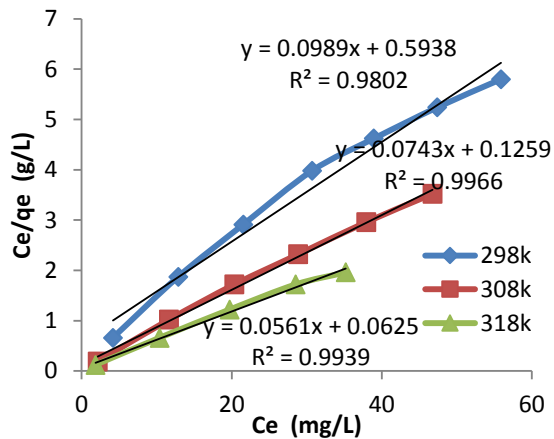


Fig. 14: Langmuir adsorption isotherm models for the removal of Mn(II) at different temperatures onto Clay/Chitosan ratio of 25:75 (adsorbent dosage of 0.25g/L, pH value of 5.5, stirring rate of 160rpm, contact time of 105 min).

Table (2): Isotherm parameters for Mn(II) removal at different temperatures onto Clay/Chitosan ratios of 75:25 (adsorbent dosage of 0.25g/L, pH value of 5.5, stirring rate of 160rpm, contact time of 105 min).

Langmuir isotherm model			
T (k)	K_L (L/mg)	b (mg/g)	R^2
298	0.67	10.11	0.98
308	0.59	13.46	0.997
318	0.9	17.83	0.994
Freundlich isotherm model			
T (k)	K_F (mg/g)	n	R^2
298	4.81	6.4	0.9
308	10.19	17.21	0.787
318	14.55	22.73	0.778

3.5.3. Temperature and thermodynamics

All experiments in this study were carried out at different temperatures 298, 308, and 318k°. The thermodynamic parameters were calculated and the nature of the adsorption processes was determined at different temperatures and the adsorption capacity of Mn(II) for Clay/Chitosan composite increased with increasing the temperature.

From equation 7 and Table (3), the negative values for the Gibbs free energy (ΔG°) at higher temperature for Clay/Chitosan ratio of 75:25 were -7.60 kJmol^{-1} . Showing that the adsorption process is

spontaneous and the degree of spontaneity of the reaction increased with the increase in the temperature and the value of ΔG° becomes more negative indicating that higher temperature facilitates the adsorption of Mn(II) on Clay/Chitosan composite due to a greater driving force of adsorption^[39].

Equation 8 represents the enthalpy (ΔH°) and the entropy (ΔS°) changes that were calculated from a plot of $\ln b$ (from the Langmuir isotherm) vs. $1/T$, Fig. (15). The results of these thermodynamic calculations are shown in Table (3). The positive value of ΔH° suggests that the interaction of Mn(II) adsorbed by Clay/Chitosan composite is endothermic process. Table (3), also shows that the ΔS° value was positive which revealed the increased randomness at the solid-solution interface during the process of adsorption^[39, 40].

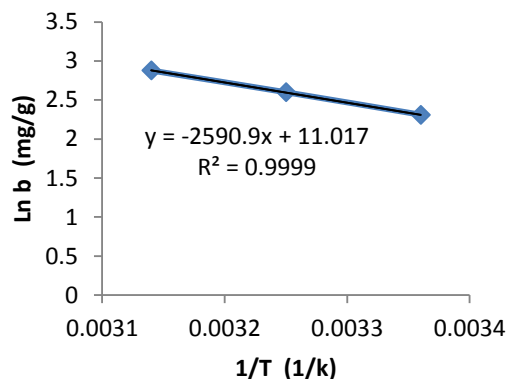


Fig.(12): Plot of the Langmuir isotherm constant ($\ln b$) vs. temperature ($1/T$) of Clay/Chitosan ratio of 75:25 (The thermodynamic parameters in Table 3 are determined from this graph).

Table3: Thermodynamic constants for the Mn(II) adsorption onto Clay/Chitosan ratio of 75:25 at different temperatures (initial Mn(II) concentration 80mg/l, pH 5.5, adsorbent mass 0.25g/l, stirring rate 160rpm).

T (k)	Lnb	ΔG° (kJmol ⁻¹)	ΔH° (kJmol ⁻¹)	ΔS° (kJmol ⁻¹ K ⁻¹)	R^2
298	2.31	-5.71	21.5	0.091	0.999
308	2.60	-6.65			
318	2.88	-7.60			

4. CONCLUSION

Preparation and characterization of nano MMT/Chitosan with different percentage loading of the nanoparticles were examined using XRD and I.R. The XRD confirm the existence and the interaction of the nanoclay within chitosan confirming the structural changes occurred in the different composites. The I.R. gave an evidence for the structural changes due to the interaction through OH and amino groups.

The adsorption process by nanoclay/chitosan composite is enhanced at certain condition as the weight ratio of the composite 75/25, pH = 5.5, the adsorbent mass about 0.25 g/L, the Mn(II) concentration 80 g/L and equilibrium contact time 105 min.

The kinetic isotherm referred to the pseudo-second-order model

The adsorption isotherm followed Langmuir model.

The calculated thermodynamics data indicated that the adsorption process is spontaneous and endothermic.

Accordingly the prepared composite system of material are very promising of removing Mn(II) from aqueous solution .

The adsorption is available tool for controlling the level of Mn(II) pollution. The utilizing of low cost adsorbents for treatment of groundwater containing metal ions is helpful as simple, effective and economical.

5. REFERENCES

- [1] Pandey, S. Mishra, Journal of colloid Interface Science, 2011, Vol. 361, p.p.: 509-520.
- [2] Han Y.; Lee, S.; Choi, K.H., Y\Journal of Physics and Chemistry of Solids, 2010, Vol. 71, p.p.: 464-467.
- [3] Chang, M.Y.; R.S.; Journal of Colloid and Interface Science, 2004, Vol. 278, p.p.: 18-25.
- [4] Krajewska, B.; Enzyme and Microbial Technology, 2004, Vol.35, p.p.: 126-134.
- [5] Lavorgna, M.; Piscitelli, F.; Mangiacapra, P.; Buonocore, G.; Carbohydrate Polymers, 2010, Vol.82, p.p.: 291-298.
- [6] Chivrac, F.; Pollet, E.; Averous, L.; Material Science and Engineering, 2009, Vol.67, p.p.: 1-17.2004
- [7] Utracki, L.A.; Clay-containing Polymeric Nanocomposites, p.p:73-96, Rapra Technology Limited, England.
- [8] Samuels R. J.; J. Polym. Sci. Phys. Ed.; 1981, 19:1081.
- [9] Ogawa, K.; Yui, T.; Miya and M.; Bioscience Biotechnology and Biochemistry, 1992, Vol. 56, p.p.: 858-862.
- [10] Bhattacharya S. S. and Mandot Adhar, 2014, Research Journal of Engineering Sciences, Vol. 3(3), p.p.: 10-16.
- [11] M. A. Khedr, A. I. Waly, A. I. Hafez and Hanaa Ali, 2012, Aust. J. Basic and Appl. Sci.; Vol. 6(6), p.p: 216-226.
- [12] Ray S. S. and Okamoto M.; Prog. Polym. Sci.; 2003, Vol.28, p.p.: 1539-1641.
- [13] S. F. Wang, L. Shen, Y. J. Tong, L. Chen, I.Y. Phang, P.Q. Lim, T.X. Liu, Polymer Degradation and Stability, 2005, Vol. 90, p.p.: 123-131.
- [14] Mano, J. F.; Koniarova D.; Reis R. L.; 2003, Journal of Materials Science, Vol. 14, p.p: 127-135.
- [15] Vhen Z.; Xiumei Mo, Oing F.; Materials Letters, 2007, Vol. 61, p.p: 3490-3494.
- [16] Xu X.; Ding Y.; Qian Z.; Wang F.; Wen B.; Zhou H.; Zhang S.; Yang M.; 2009, Polymer Degradation and Stability, Vol. 94, p.p.: 113-123.
- [17] Darder M.; Colilla M.; Ruiz-Hitzky E.; Chemical Material, 2003, Vol. 15, p.p.: 3774-3780.
- [18] Paluszkiwicz C.; Stodolak E.; Hasik M. and Blazewicz M.; Spectrochim Acta part A, 2011, Vol.79, p.p.: 784-788.
- [19] Yuan Q.; Shah J.; Hein S.; Misra R. D. K.; Acta Biomaterial, 2010, Vol. 20, p.p.: 1140-1148.
- [20] Madejova J.; Vibrational Spectroscopy, 2003, Vol. 31, p.p.: 1-10.
- [21] Z. Navratilova, P. Wojtowicz, L. Vaculikova and V. Sugarkova, Acta Geodym. Geomater, 2007, Vol.4, No. 3 (147), p.p.: 59-69.
- [22] X. Wang, Y. Du, J. Yang, X. Wang, X. Shi and Y. Hu, Polymer, 2006, Vol. 47, No.19, p.p.: 6738-6744.
- [23] E. Günister, D. Pestreli, C. H. Vnlü, O. Atici and N. Güngö, Carbohydrate Polym.; 2007, Vol.67, p.p.: 358-365.
- [24] Y. Han, S. H. Lee, K. H. Choi, In Pac J. Phys. And Chemis. Of Solid, 2010, p.p.: 464-467.
- [25] M. S. Mostafa, A. A. Baker, Gh. Eshaq, M. M. Kamel, Desalination and Water Treatment, DOI: 10.1080/19443994.2014.934725, p.p.: 1-9.
- [26] AL-Sayed A. Bakr, Yasser M. Moustafa, Mostafa M. Khalil, Mohamed M. Yehia and Eman A. Motawea, 2015, Vol. 93 (3), p.p.: 289-296.
- [27] A.A. Bakr, M.S. Mostafa, Gh. Eshaq and M. M. Kamel, Desalination and Water Treatment, DOI:10.1080/19443994.2014.934729, p.p: 1-8.
- [28] A. A. Bakr, Gh. Eshaq, A. M. Rabie, A. H. Mody, A. E. Elmetwally, Desalination and Water Treatment, DOI: 10.1080/19443994.2015.1051126, p.p.: 1-12.
- [29] AL-Sayed A. Bakr, Yasser M. Moustafa, Mostafa M. Khalil, Mohamed M. Yehia and Eman A. Motawea, Journal of Enviroment Chemical Engineering, 2015, Vol. 3 (3), p.p.: 1486-1496.

- [30] Yu L. and Ya-Juan L.; Sep. Purif. Technol.; 2008, DOI: 10.1016/j.seppur.2007.10.002, p.p.: 229-242.
- [31] Pham Xuan Nui, Petro. VIETNAM Journal,2014, Vol.6, p.p.: 62-68
- [32] D. P. Das, J. Das, K. Parida, J. Colloid Interface Sci.; DOI: 10.1016/S0021-9797(03)00082-1, P.P: 213-220.
- [33] C. Chen, J. L. Wang, J. Hazard. Mater.; DOI: 10.1016/j.jhazmat.2007.05.046, p.p.:65-70.
- [34] A. K. Bhattacharya, T. K. Naiya, S. N. Mondal, S. K. Das, Chem. Eng. J.; DOI:10.1016/J.CEJ.2007.05.021, P.P.: 529-541.
- [35] L. M. Zhou, J. Y. Jin, Z. R. Liu, X. Z. Liang, C. Shang, J. Hazard. Mater.; DOI:10.1016/j.hazmat.2010.10.012, p.p.: 1045-1052.
- [36] N. Zahra Pak, J. Anal. Environ. Chem.; 2012,Vol.13, No.1.
- [37] L. Ai, C. Zhang, Z. Chen, J. Hazard. Mater.; DOI:10.1016/j.jhazmat.2011.06.068.; p.p.: 1515-1524.
- [38] Ho Y. S. and McKay G.; Process Biochem.; 1999a, Vol.34(5), p.p.: 451-465.
- [39] K. H. Gho, T. T. Lim, Z. Dong, Environ. Sci. Technol.;2009, DOI:10.1021/es 802811n.; p.p.: 2537-2543.
- [40] M. Dakiky, M. Khamis, A. Manassra, Adv. Environ.;2002,DOI:10.1016/S1093-0191(01)00079X.; p.p: 533-540.

Effect of Adding Indium on Wetting Behavior, Microstructure and Physical Properties of Tin- Zinc Eutectic Alloy

Abu Bakr El- Bediwi
Metal Physics Lab.,
Physics Department,
Faculty of Science,
Mansoura University
Mansoura, Egypt

Mohammed Munther
Jubair
Ministry of Education
Iraq

Rizk Mostafa Shalaby
Metal Physics Lab.,
Physics Department,
Faculty of Science,
Mansoura University
Mansoura, Egypt

Mustafa Kamal
Metal Physics Lab.,
Physics Department,
Faculty of Science,
Mansoura University
Mansoura, Egypt

Abstract: Effect of adding indium on microstructure, wetting process, thermal, electrical and mechanical properties of tin- zinc eutectic alloy have been investigated. Microstructure (started base line, lattice parameters, unit cell volume, crystal size and the shape of formed crystalline phases) and measured physical properties of tin- zinc eutectic alloy changed after adding different ratio of indium content. A little variation occurred in thermo-graph (Endo-thermal peaks) of $\text{Sn}_{91}\text{Zn}_9$ alloy after adding indium. The contact angle, melting temperature and specific heat of $\text{Sn}_{91}\text{Zn}_9$ alloy decreased after adding indium content. Also elastic modulus and internal friction values of $\text{Sn}_{91}\text{Zn}_9$ alloy decreased after adding indium content. But electrical resistivity and Vickers hardness values of $\text{Sn}_{91}\text{Zn}_9$ alloy increased after adding indium content. The SnZnIn_5 alloy has adequate properties for solder applications.

Key words: tin- zinc eutectic alloy, thermal and mechanical properties, electrical resistivity, wetting process

1. INTRODUCTION

Over the past few years the study of lead free solder has become a hot subject. New lead free solder alloy has great attention from researchers around the world. Lead free solders fall into two groups: first has lower melting points and chiefly includes alloys of tin and bismuth. Second is group of alloys, those with higher melting points than tin-lead. The leading choice seems to be a tin-silver-copper alloy. There is a tin-rich ternary eutectic at about 217 °C. These alloys at 30 °C higher melting point are a challenge to use. Sn-Zn solder alloys are quite capable in terms of mechanical integrity but have poor oxidation and corrosion resistance. Many studies have been made on various alloy system solders based on Sn such as SnZn_9 , $\text{SnAg}_{3.5}$, $\text{SnAg}_3\text{Cu}_{0.5}$, etc. as possible replacements [1, 2]. T. Ohoak et al investigated the dependence of frequency over a range of 0-3 Hz on Young's modulus and internal friction in SnZn_9 and $\text{SnAg}_{3.5}$ eutectic lead free solder alloys [3]. Several researchers [4- 7] operated to improve the properties of Sn-Zn lead free alloy by adding small amount of alloying elements such as Bi, Cu, In, Ag, Al, Ga, Sb, Cr, Ni, Ge to develop ternary and even quaternary Pb free alloys. The microstructures of the tin- zinc- aluminum lead free solder alloys, which prepared from the Zn-5Al master alloy and Sn, using scanning electron microscopy were investigated [8]. The microstructures and mechanical properties of $\text{SnZn}_{8.55}\text{Ag}_x\text{Al}_{0.45}\text{Ga}_{0.5}$ ($x=0.5-3$ wt. %) lead free solder alloys were studied [9]. Small additions of Ag decreased the melting point of the $\text{SnZn}_{8.55}\text{Ag}_x\text{Al}_{0.45}\text{Ga}_{0.5}$ solder alloys while maintaining the same strength and ductility as the $\text{Sn}_{63}\text{b}_{37}$ solder alloy. The effects of adding alloying elements such as Ag, Al, and Ga, on melting temperature, microstructures and mechanical properties of the SnZn_9 lead free solder alloy were studied [10]. The results show, $\text{SnZn}_9\text{Ga}_{0.5}$ alloy has very good UTS and elongation, which are better than both those of the $\text{SnZn}_9\text{Ag}_{0.5}$ and $\text{SnZn}_9\text{Al}_{0.45}$ alloys. Also effect of adding Al and Cu on microstructural and mechanical properties as well as thermal behavior of SnZn_9 lead free solder alloy was investigated [11]. The results indicate the microhardness of the $\text{SnZn}_9\text{Al}_{0.5}$ alloy was also higher than that of the $\text{SnZn}_9\text{Cu}_{0.5}$ alloy. Tin- zinc is desired to have a lead free solder with a melting temperature close to the eutectic temperature of the tin- lead alloy.

Aluminum has a high melting temperature and good electrical conductivity. It may form solid solutions with tin and zinc. . So that, adding aluminum to tin- zinc solder alloy retain the melting point as low as possible but the soldering temperature higher than that eutectic tin- lead alloy. The aim of this work was to investigate the effect of adding different ratio from indium on microstructure, wetting behavior, thermal, electrical and mechanical properties of tin- zinc eutectic lead free solder alloy.

2. EXPERIMENTAL WORK

The alloys $\text{Sn}_{91-x}\text{Zn}_9\text{In}_x$ ($X=0, 1, 2, 3, 4$ and 5 wt. %) which used tin, zinc and indium elements with a high purity, more than 99.95%, were molten in the muffle furnace. The resulting ingots were turned and re-melted several times to increase the homogeneity of the ingots. From these ingots, long ribbons of about 3-5 mm width and ~ 80 μm thickness were prepared as the test samples by directing a stream of molten alloy onto the outer surface of rapidly revolving copper roller with surface velocity 31 m/s giving a cooling rate of 3.7×10^5 K/s. The samples then cut into convenient shape for the measurements using double knife cutter. Structure of used alloys was performed using a Shimadzu x-ray diffractometer (Dx-30, Japan) of Cu-K α radiation with $\lambda=1.54056 \text{ \AA}$ at 45 kV and 35 mA and Ni-filter in the angular range 2θ ranging from 20 to 100° in continuous mode with a scan speed 5 deg/min. Scanning electron microscope JEOL JSM-6510LV, Japan was used to study microstructure of used samples. The melting endotherms of used alloys were obtained using a SDT Q600 V20.9 Build 20 instrument. A digital Vickers microhardness tester, (Model-FM-7- Japan), was used to measure Vickers hardness values of used alloys. Internal friction Q^{-1} and the elastic constants of used alloys were determined using the dynamic resonance method [12- 14].

3. RESULTS AND DISCUSSIONS

Microstructure

X-ray diffraction patterns of $\text{Sn}_{91-x}\text{Zn}_9\text{In}_x$ ($x = 0, 1, 2, 3, 4, 5$ wt. %) rapidly solidified alloys show that sharp lines of body centered tetragonal Sn and hexagonal Zn phases as presented in Figure 1. From x-ray analysis, adding In content to SnZn_9 alloy produced a change in its matrix microstructure (lattice parameters, unit cell volume and crystal size) and the shape of formed phases such as peak intensity, peak broadness and peak position. That is because In atoms dissolved in $\text{Sn}_{91}\text{Zn}_9$ matrix formed a solid solution or and some In atoms formed a traces of undetected phases (In or In intermetallic phases). Also the calculated lattice parameters, (a and c), unit volume cell and crystal size of tetragonal tin phase in $\text{Sn}_{91-x}\text{Zn}_9\text{In}_x$ ($x = 0, 1, 2, 3, 4, 5$ wt. %) alloys are listed in Table 1. The results illustrated that, adding In content to $\text{Sn}_{91}\text{Zn}_9$ alloy caused a little variation in lattice parameters and unit cell volume with a significant variation in crystal size of tetragonal tin phase of $\text{Sn}_{91}\text{Zn}_9$ alloy after adding In content.

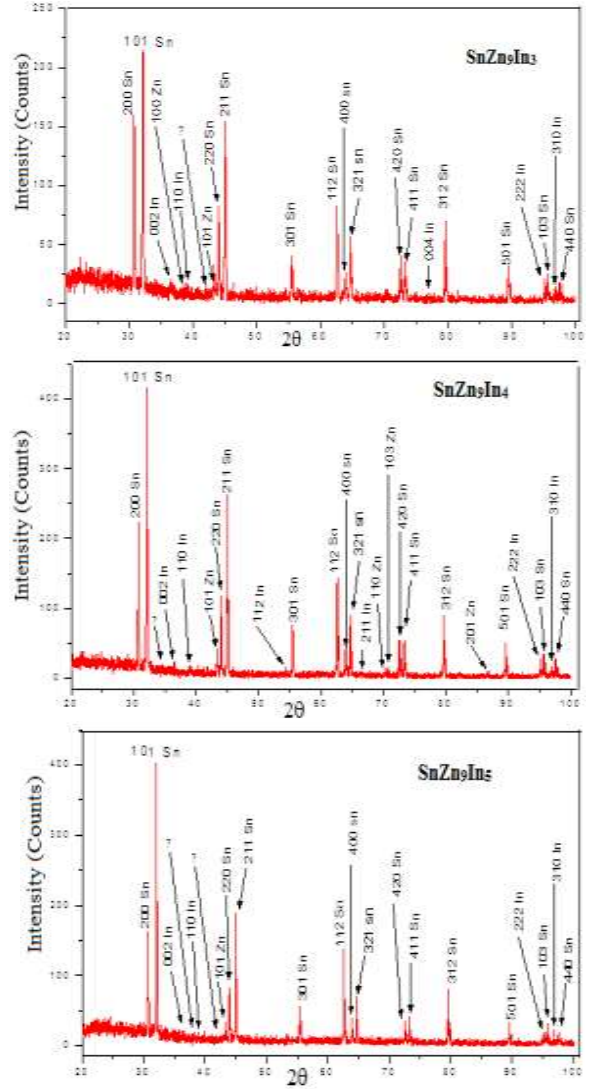
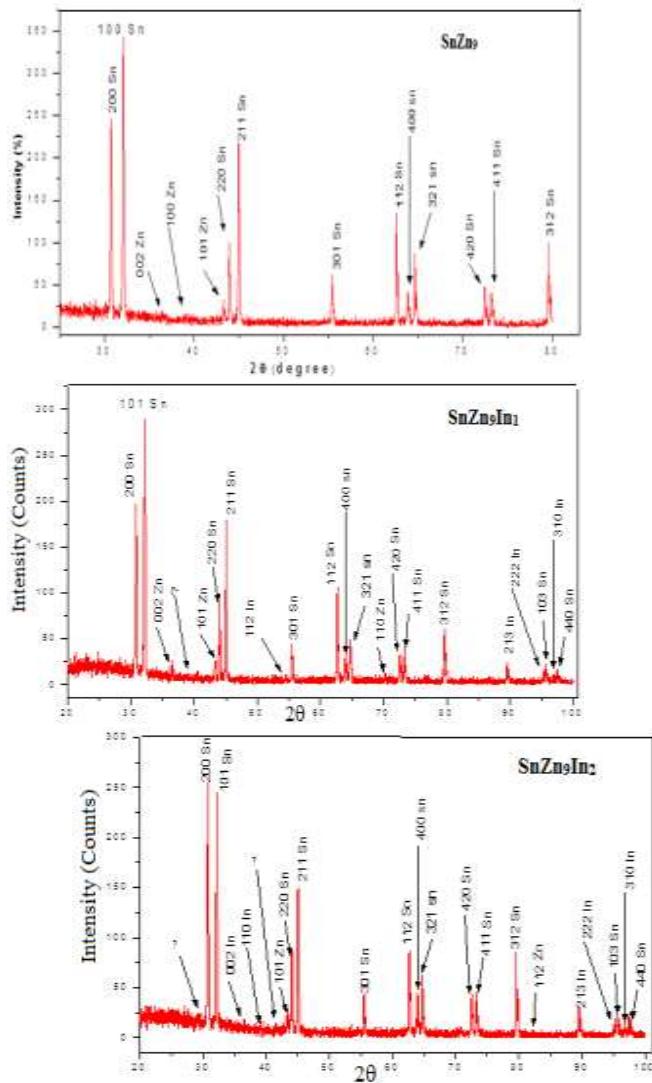


Figure 1:- x-ray diffraction patterns of $\text{Sn}_{91-x}\text{Zn}_9\text{In}_x$ alloys

Table 1:-lattice parameters, unit cell volume and crystal particle size of β -Sn in $\text{Sn}_{91-x}\text{Zn}_9\text{In}_x$ alloys

Samples	a Å	c Å	V Å ³	τ Å
SnZn_9	5.82	3.183	107.83	681.943
SnZn_9In_1	5.801	3.182	107.11	454.054
SnZn_9In_2	5.805	3.188	107.45	465.097
SnZn_9In_3	5.814	3.189	107.78	707.90
SnZn_9In_4	5.812	3.189	107.70	593.691
SnZn_9In_5	5.821	3.180	107.76	658.568

Scanning electron micrographs, SEM, of $\text{Sn}_{91-x}\text{Zn}_9\text{In}_x$ ($x=0, 1, 2, 3, 4, 5$ wt. %) alloys show heterogeneous structure (different features) as seen in Figure 2 and it's agreed with x-ray analysis.

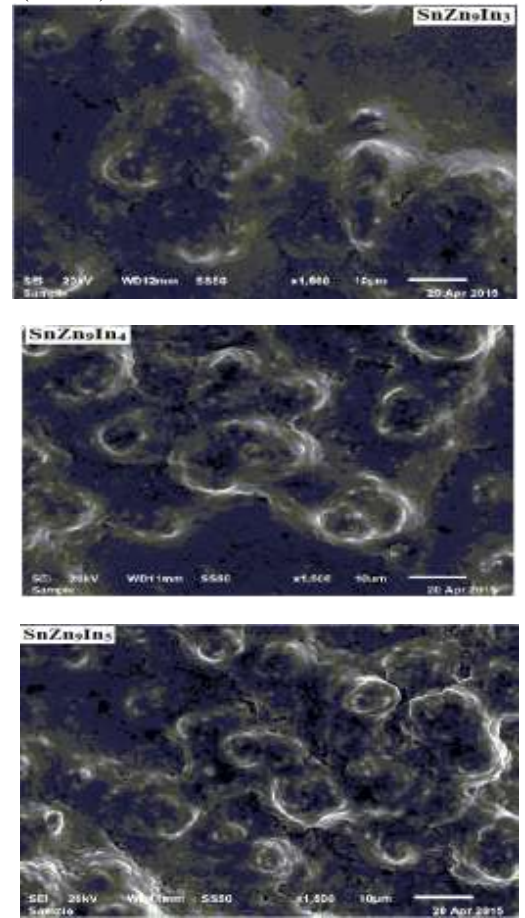
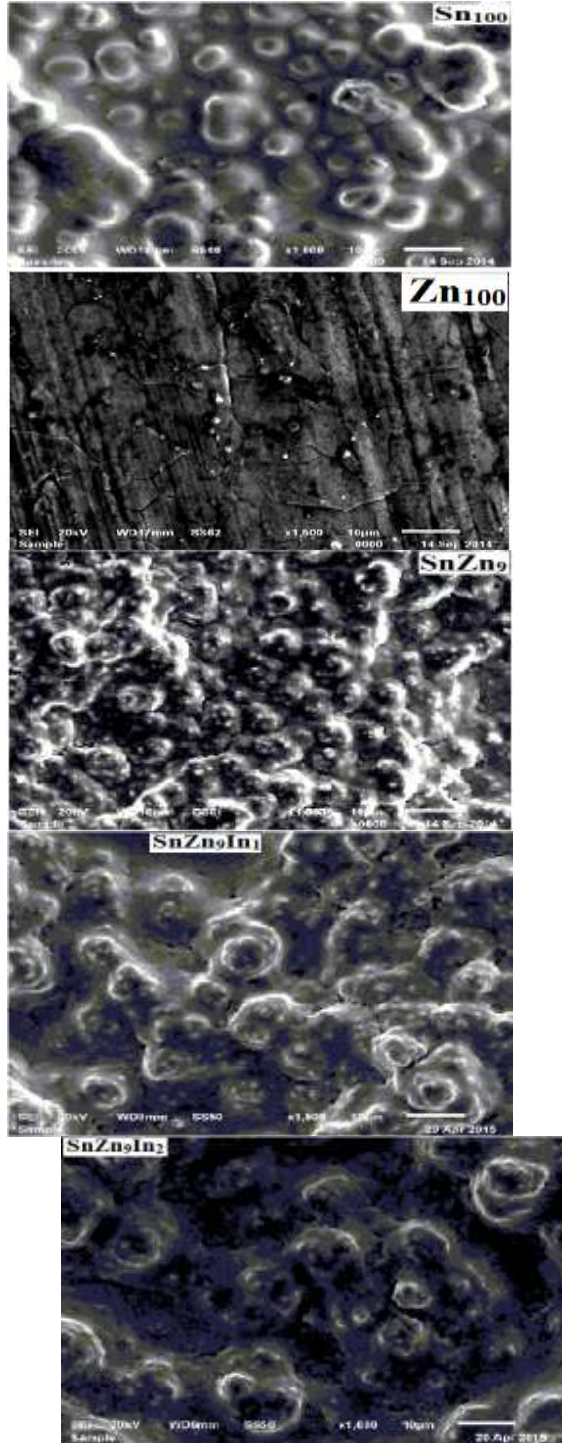


Figure 2:- SEM of $\text{Sn}_{91-x}\text{Zn}_9\text{In}_x$ alloys

Soldering properties
Wettability

Wettability is quantitatively evaluated by the contact angle formed at the solder substrate's flux triple point. The contact angles of $\text{Sn}_{91-x}\text{Zn}_9\text{In}_x$ ($x=0, 1, 2, 3, 4, 5$ wt. %) alloys on Cu substrate in air are shown in Table 2. The results show that, the contact angle of $\text{Sn}_{91}\text{Zn}_9$ alloy is variable decreased after adding In content. The $\text{Sn}_{86}\text{Zn}_9\text{In}_5$ alloy has low contact angle value and also adequate for solder applications.

Table 2:-contact angles of $\text{Sn}_{91-x}\text{Zn}_9\text{In}_x$ alloys

Samples	Contact angle (θ°)
SnZn9	46
SnZn9In1	42.5
SnZn9In2	45.75
SnZn9In3	45
SnZn9In4	42
SnZn9In5	38.25

Thermal properties

The amounts of thermal properties depend on the nature of solid phase and on its temperature. The DSC thermographs were achieved with heating rate 10 °C /min in the temperature range 0- 400 °C. The DSC thermographs of Sn_{91-x}Zn₉In_x (x= 0, 1, 2, 3, 4, 5 wt. %) alloys are shown in Figure 3. From these graphs the melting point, pasty range and other thermal parameters (specific heat, C_p, enthalpy, ΔH, entropy, ΔS) of Sn_{91-x}Zn₉In_x (x= 0, 1, 2, 3, 4, 5 wt. %) alloys are identified and then listed in Table 3. A little variation occurred in thermo-graph (Endo-thermal peaks) of Sn₉₁Zn₉ alloy after adding indium. That is because In atoms dissolved in matrix alloy changed its structure and that is agreed with x-ray diffraction analysis. The melting temperature of Sn₉₁Zn₉ alloy decreased after adding indium content. Also the pasty range and other thermal parameters of Sn₉₁Zn₉ alloy varied after adding indium content.

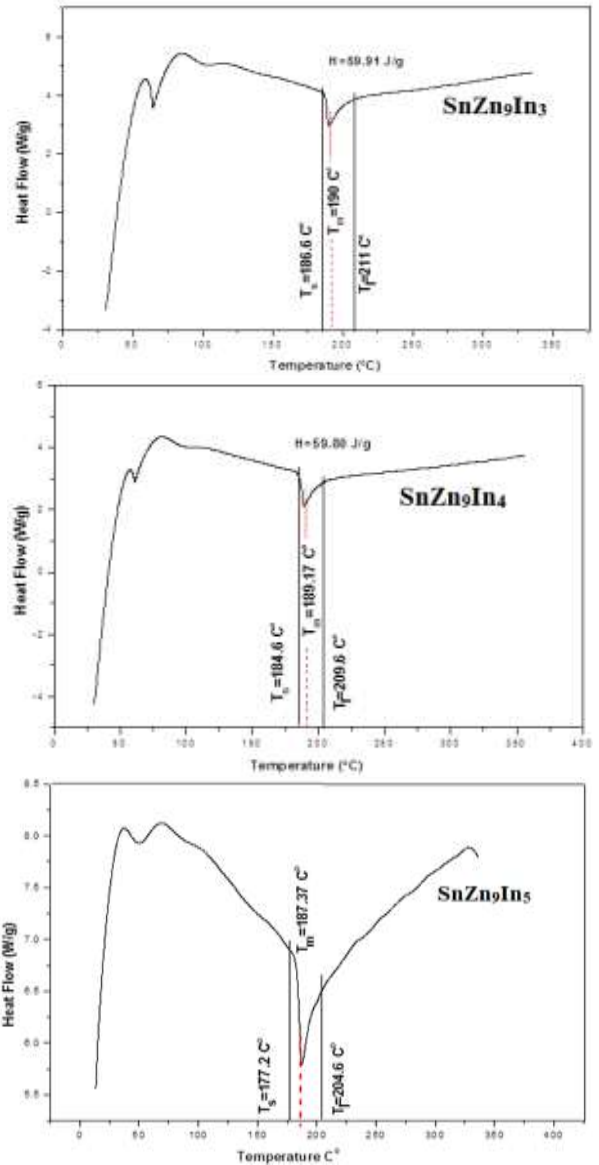
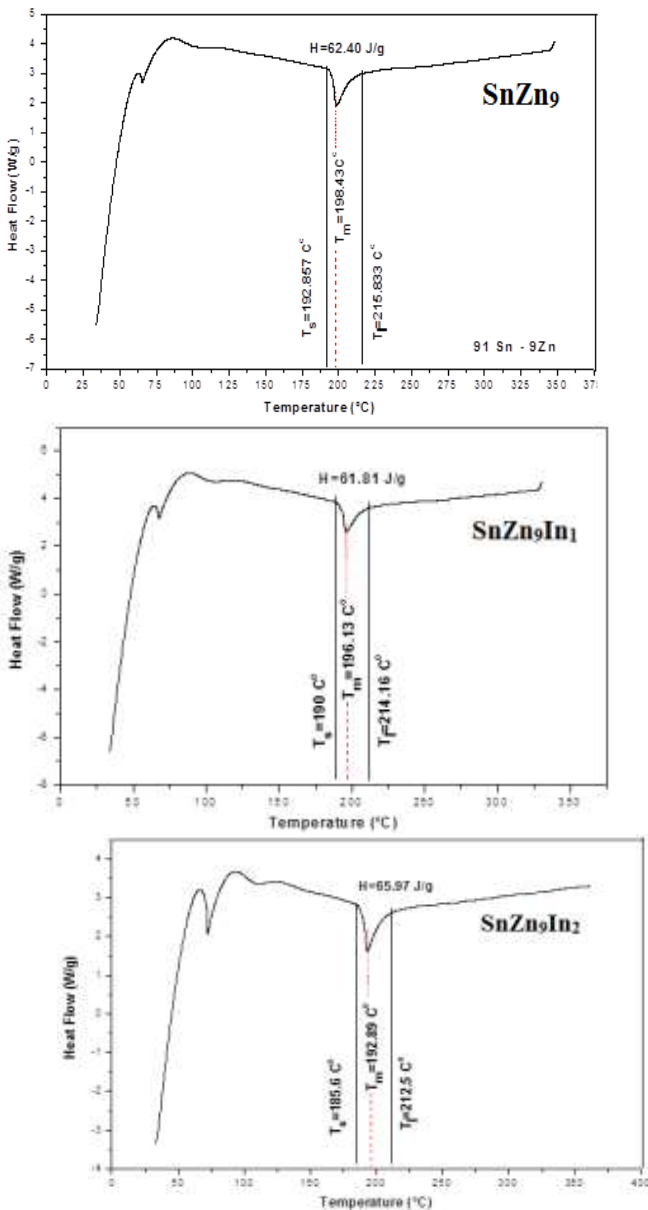


Figure 3:- DSC graphs of Sn_{91-x}Zn₉In_x alloys

Table 3:- melting point and other thermal parameters of Sn_{91-x}Zn₉In_x alloys

Samples	Melting point °K	C _p J/g. °K	Δ S J/g. °K	ΔH J/g
SnZn ₉	471.43	2.716	130.772	62.40
SnZn ₉ In ₁	469.13	2.558	130.155	61.81
SnZn ₉ In ₂	465.89	2.45	139.889	65.97
SnZn ₉ In ₃	463.12	2.46	127.025	59.91
SnZn ₉ In ₄	462.17	2.392	127.256	59.80
SnZn ₉ In ₅	460.37	2.271	151.858	71.45

Electrical resistivity

Crystalline imperfections and plastic deformation raises the electrical resistivity as a result of the increased number of electron scattering centers. The measured electrical resistivity of $\text{Sn}_{91-x}\text{Zn}_9\text{In}_x$ ($x=0, 1, 2, 3, 4, 5$ wt. %) alloys at room temperature using double bridge method are shown in Table 4. Electrical resistivity of $\text{Sn}_{91}\text{Zn}_9$ alloy variable increased after adding indium content. That is because indium atoms dissolved in the $\text{Sn}_{91}\text{Zn}_9$ matrix, formed solid solution/or and some traces, played as scattering center for conduction electrons increased electrical resistivity value.

Table 4:- electrical resistivity of $\text{Sn}_{91-x}\text{Zn}_9\text{In}_x$ alloys

Samples	$\rho \times 10^{-8} \Omega \cdot \text{m}$
SnZn_9	33.65
SnZn_9In_1	35.6
SnZn_9In_2	39.94
SnZn_9In_3	40.83
SnZn_9In_4	38.27
SnZn_9In_5	39.39

Mechanical properties

Elastic moduli

The elastic constants are directly related to atomic bonding and structure. It is also related to the atomic density. The measured elastic modulus and calculated bulk modulus, B, and shear modulus, μ , of $\text{Sn}_{91-x}\text{Zn}_9\text{In}_x$ ($x=0, 1, 2, 3, 4, 5$ wt. %) alloys are listed in Table 5. Elastic modulus value of $\text{Sn}_{91}\text{Zn}_9$ alloy is variable decreased after adding indium content as shown in Table 5. That is because the dissolved indium atoms, formed solid solution\ or stick on grain boundary/ or formed small cluster from phases in $\text{Sn}_{91}\text{Zn}_9$ matrix, affected on bond matrix strengths.

Internal friction and thermal diffusivity

Internal friction is a useful tool for the study of structural aspects of alloys. Resonance curves of $\text{Sn}_{91-x}\text{Zn}_9\text{In}_x$ ($x=0, 1, 2, 3, 4, 5$ wt. %) alloys are shown in Figure 4 and the calculated internal friction values are presented in Table 5. Also from resonance frequency at which the peak damping occur using the dynamic resonance method the thermal diffusivity value was calculated and then listed in Table 5. The results show that, internal friction value of $\text{Sn}_{91}\text{Zn}_9$ alloy is variable decreased by adding indium content.

Table 5:- elastic moduli, internal friction and thermal diffusivity of $\text{Sn}_{91-x}\text{Zn}_9\text{In}_x$ alloys

Samples	E GPa	μ GPa	B GPa	Q^{-1}	$D_{th} \times 10^{-7} \text{m}^2/\text{sec}$
SnZn_9	44.34±3.1	16.42	49.30	0.085	4.476
SnZn_9In_1	30.75±1.2	11.39	34.05	0.052	3.392
SnZn_9In_2	29.53±1.2	10.95	32.57	0.054	2.947
SnZn_9In_3	33.04±2.1	12.25	36.3	0.081	3.484
SnZn_9In_4	32.9±2.19	12.20	35.99	0.057	2.773
SnZn_9In_5	30.09±1.6	11.17	32.80	0.059	2.316

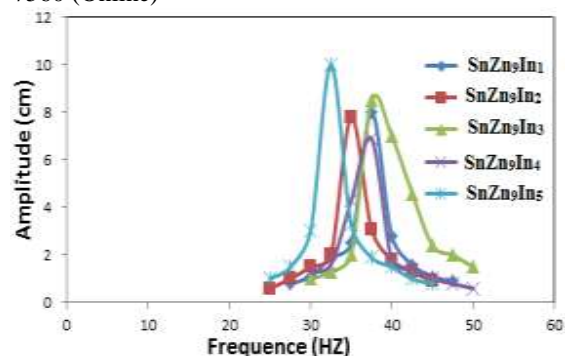


Figure 4:- resonance curves of $\text{Sn}_{91-x}\text{Zn}_9\text{Al}_x$ alloys

Vickers microhardness and minimum shear stress

The hardness is the property of material, which gives it the ability to resist being permanently deformed when a load is applied. The greater of material hardness is the greatest of the resistance to deformation. The Vickers hardness number of $\text{Sn}_{91-x}\text{Zn}_9\text{In}_x$ ($x=0, 1, 2, 3, 4, 5$ wt. %) alloys at 10 gram force and indentation time 5 sec are shown in Table 6. Also calculated minimum shear stress of $\text{Sn}_{91-x}\text{Zn}_9\text{In}_x$ ($x=0, 1, 2, 3, 4, 5$ wt. %) alloys are listed in Table 6. Vickers hardness value of $\text{Sn}_{91}\text{Zn}_9$ alloy is variable increased by adding indium content.

Table 6:- Vickers hardness and minimum shear stress of $\text{Sn}_{91-x}\text{Zn}_9\text{In}_x$ alloys

Alloys	$H_v \text{ kg/mm}^2$	$\mu_n \text{ kg/mm}^2$
SnZn_9	22.75±1.1	7.508
SnZn_9In_1	23.53±1	7.766
SnZn_9In_2	27.8±1.23	9.174
SnZn_9In_3	30.7±1.9	10.131
SnZn_9In_4	26.37±1.2	8.701
SnZn_9In_5	36.82±2.5	12.149

4. CONCLUSIONS

1. Adding indium content to SnZn_9 alloy produced a change in its matrix microstructure (lattice parameters, unit cell volume and crystal size) and the shape of formed phases
2. The contact angle, melting temperature, elastic modulus and internal friction values of SnZn_9 alloy are variable decreased after adding indium content. The SnZn_9In_5 alloy has low contact angle and melting point values.
3. The electrical resistivity and Vickers hardness values of SnZn_9 alloy are variable increased after adding indium content.
4. The SnZn_9In_5 alloy has adequate properties for solder applications

5. REFERENCES

- [1] Shiue R. K, Tsay L. W, Lin C. L and Ou J. L, J. Mater. Sci. 38 (2003) 1269
- [2] Miiyamoto A, Ogawa T and Ohsawa T, Mater. Sci. Res. Inter. 9 (2003) 16
- [3] Ohoka T, Nakamura Y, Ono T, J. Mater. Sci. 39 (2004) 4379
- [4] Kim K.S, Yang J.M, Yu C.H, Jung I.O, Kim H. H, J. Alloy.

Compd. 379 (2004) 314

- [5] Anderson I. E, Foley J. C, Cook B. A, Haringa J, Terpstra R. L, Unal O, J. Electron. Mater. 30: 9 (2001) 1050
- [6] McCormack M, Jin S, Kammlott G. W, Chen H. S, Appl. Phys. Lett. 63: 1 (1993) 15
- [7] Miric A. Z, Grusd A, Surf. Mount Technol. 10: 1 (1998) 19
- [8] Lin K. L, Hsing L and Liu T. P, J. electronic materials, 27: 3(1998) 97
- [9] Lin K. I and Lin K. L, J. of Electron. Mater. 31:8 (2002) 861
- [10] Chen K. I, Cheng S. C, Wu S and Lin K. L, J. alloy. Compd. 416 (2006) 98
- [11] Das S. K, Sharif A, Chana Y. C, Wongc N. B and Yung W. K. C, J. Alloy. Compd. 481 (2009) 167
- [12] Cullity B. D, "Element of x-ray diffraction" Ch.10 (1959) 297
- [13] Sppinert S and Teffit W. E, ASTM, Proc. 61 (1961) 1221
- [14] Schreiber E, Anderson O. L and Soga N, Elastic Constants and their Measurement, McGraw-Hill Book Company, Ch. 4 (1973)

Improvement in the Wear Resistance of Brass Impeller of Slurry Pump used in Variation of Operating Speeds

Ahmed M.M. El-Bahloul
Production Engineering and
Mechanical Design
Department,
Faculty of Engineering
University of Mansoura, Egypt

. M.Samuel
Production Engineering and
Mechanical Design
Department,
Faculty of Engineering
University of Mansoura,
Egypt

Mazin.K.I. AL-Mashhadani
Ministry of Science and
Technology,
Iraq

Abstract : Erosion wear is recognized as an engineering problem for Centrifugal slurry pumps it plays an important role in design and operation of slurry transportation systems. In most slurry pump applications the monetary loss due to pump failure consists of loss of production rather than the cost of the pump, since the process must be shut down when the pump fails. If the erosion rate can be estimated, the pump's impeller can be changed out in time, during scheduled maintenance, The present work reports experimental investigations on dependence of erosion wear of brass alloys in sand - water slurry. Systematic study on the failing impeller of a slurry pump used in irrigation has been carried out by means of scanning electron microscopy in order to clarify the failure mechanisms. The results show .The weight loss of the impeller due to the material removal from the impeller as result of erosion wear. In this investigation, experiments were carried out to evaluate the wear resistance using wear test rig designed and manufactured for this purpose. Three specimens of different brass alloys were used, namely (CuZn2Ge-CuZn4Ge-CuZn6Ge) Discs manufactured from. The accumulated loss of weight was measured and the wear rates were determined for each Case material at constant normal test load of 20kg and time 24hr. Number of revolutions of tests equals (1000- 1500-2000) r.p.m. were selected for the three test materials respectively during wear tests .The accumulated loss of weight was measured as a function of the number of revolutions. Wear rate was calculated. The results show Wear rate for material B3 (CuZn6Ge) is less than that of the wear rate for B2 (CuZn4Ge), B1 (CuZn2Ge) under the same testing conditions at (1000-1450-2000) r. p. m.

Keywords: Brass, Structures, wear test, Wear rate, hardness,

INTRODUCTION

Pumps play a key role in irrigation and moving and lifting fluids in general to high areas. A mechanical equipment lowly fluid lift from a low level to high level considered pumps Calendar Irrigation of very necessary and important equipment which are used in a wide areas and there was a need to study so that we can choose the appropriate pump for a particular performance as well as the possibility to run different speeds And the impact on its performance in use irrigation pumps efficiently and tak advantage of the increase Productivity the Iraqi farm[1] Erosive Wear is a phenomenon related to material removal from a surface due to interaction with a mating surface. Wear is a common industrial problem, leading to frequent maintenance and replacement of components, and loss associated with production or availability, which also carries economic penalties. In addition, wear may also decrease the operating efficiencies [2]. Wear can generally be divided into two main types that are mechanical wear and chemical wear [3]. It is generally held that the most common types of wear mechanism are the adhesive wear, abrasive wear, cavitation wear, corrosive wear, erosive wear, fatigue wear and fretting wear. Infect, more than a single mechanism can occur at the same time [4].However, there is always a primary mechanism that determines the material removal rate. Impellers wear rate in a slurry pump is an important factor. Slurry pumps are used almost universally to move mixtures of abrasive solid sand liquids. Pump useful life in these applications can range from a few weeks to a few years depending on the type of slurries handled. Major wet end components of a centrifugal

slurry pump including impeller wear occurs largely as a result of erosion [5].The term "erosive wear" refers to an unspecified number of wear mechanisms which occur when relatively small particles impact against mechanical components The major type of erosion wear in a slurry pump impeller is due to the Particle impingement.[6].Where the particles impact at angles substantially normal to the surface. The predominant type of wear in centrifugal pump impeller is sliding-bed erosion whereas erosion wear is caused by impact of liquid or solid particles on the solid surface. The main cause of the erosion wear is impact [7]. Particles impacting directly onto a surface can generate very high specific contact pressures. The actual value of the contact stress depends on the particle velocity, the mass, and the particle shape. Particles with sharp edges wear the surface faster because of their smaller contact area (and thus higher stresses). Material is removed by a process of cutting and/or pouching.[8] Pouching Erosion wear: is a two stage process involving localized plastic deformation of the surface from rounded particle impacts [9].Cutting Erosion wear: occurs when the particles are very sharp and interaction with the material surface causes a micromachining action [10].Deformation and Cracking: When cyclic forces are applied to parts found in the pump, a crack may appear over a period of time, in a target surface. Deformation and Cracking can occur on a surface, even though the loading produces stresses that are far less than the tensile strength of the material. after the crack has been introduced into the surface. the crack may grow with each cyclic loading until the surface finally Deformation and Cracking[11].Elemental analysis of the failed impeller blades, as well as the middle of blades, shows that the

base alloy used for this impeller is Brass. Physical examinations, that the leading edge of the impeller had undergone active corrosion with rough surface and visible pit like features. Chemical analysis of the blade surface at various locations indicated at the surface. This confirms that the erosion wear of surface has occurred on these alloys in the environment to which this impeller was exposed. To verify further the effect of velocity on the erosion rate of an impeller, simulated erosive wear tests were performed on a rotating disk on disk with of tested materials used in this investigation and samples from the failing impeller. Three speeds were used. The first is (1000) r. p. m and the second is (1450) r. p. m. The third (2000)

2. Experimental Work

2.1. Test Specimens

2.1.1. Materials: used in this investigation for impeller pump production in are as follows: (B1(CuZn2Ge), (B2(CuZn4Ge),(B3(CuZn6Ge)).The chemical composition for materials used in this investigation is given in table (1).

2.1.2. Specimen Dimensions:

Specimens were prepared from Base metal (CuZn2Ge), (CuZn4Ge), (CuZn6Ge), for wear test, Chemical composition of alloys as Table (1) microstructure and hardness.

2.1.3. Test specimens for wear:

Specimens were prepared from Base metal (brass)and(CuZn2Ge),(CuZn4Ge),(CuZn6Ge),80mm diameter & 15 mm length , shown in figure (1,a), which were turned ,shown in figure (1,b) , In this work 24 discs were used , 6 discs from each tested materials divided into 4 groups ;(2) discs for each group follows: shown in Table(2).it used speed (1000,1450,2000), r. p. m

(a)-Cu-Zn (Ge 2%, 4%,6%) 18 discs .

(b)-Base metal (brass) of (6) discs.

No.	Zn%	Ge %	Fe%	P%	S%	Cu %
B1	29.98 9	2.01 7	0.001 8	0.006	0.00 3	Rem
B2	29.98 7	4.01 4	0.002	0.001	0.00 1	Rem
B3	29.97 5	6.01 1	0.001	0.004	0.00 2	Rem
Base meta l	29.86 2	0.0	0.002 2	0.001 5	0.00 9	Rem

Table (1) Chemical composition

Speed(r.p.m)	B1(2%Ge)	B2(4%Ge)	B3(6%Ge)	Base metal
1000(r.p.m)	B11/B11"	B21/21"	B31/B31"	brass1/brass1"
1450(r.p.m)	B12/B12"	B22/B22"	B32/32"	brass2/brass2"
2000 (r.p.m)	B13/B13"	B23/B23"	B33/B33"	brass3/brass3"

Table (2) Test Specimens Materials for wear

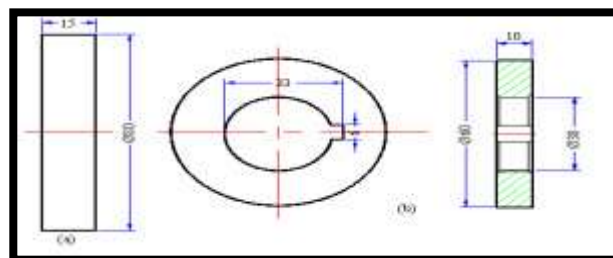


Fig (1, a, b) The shape and dimensions of test discs

3. Experimental Tests

3.1. Wear Test

Wear is usually measured by one of two methods either by measuring dimensional changes or by weight loss. In this study, wear was estimated and measured by weight loss. Precise digital balance was used. The accuracy of the balance and its capacity is 240 g. By weighting the specimens before and after each run, it was possible to calculate the weight loss due to wear. Thus the accumulated wear as a function of rolling distance can easily be investigated and plotted. From the plots and knowing the density of the material, it was possible to calculate the wear rate of tested materials. [12].

$$\text{Wear rate} = W / (P * N)$$

Where: W: Accumulated weight of removed metal (mg).

P: is normal applied load.(kg)

N : Total number of revolutions.

3.2. Wear Testing Machine Disc machine;

in the two-disc machine, one disc is mounted in a bearing supported by a swinging arm while the other is carried on a rigid bearing .The disc carried by a swinging arm is pressed against the other by a loaded lever. Wear machine manufactured in Gears laboratory in department production engineering and mechanical design: The machine consists of upper casing part (1) cast iron boxes and their housing (3) to carry the bearings support driven discs specimens, lower casing part (2) cast iron boxes and their housing (4) to carry the bearings support driver discs specimens. Bearing housing (3,4) to support the single row deep groove ball bearings (11) 6003zz . Driven and drive shaft (5,6) to carry the driven and drive discs (7) , spacing sleeve (8) to adjust the distance between the discs and ball bearing , key (9) to fix the discs with the shafts , Snap ring Φ 17 mm (10) to locate the bearing inner race with the shafts , spacer sleeve (12) , to adjust the distance between the ball bearing and the driven pulley (13) which fix by key (16) , the washer (14) and the bolt (15) to fixed the pulley. Base (17) Dimensions, 400 * 600 mm, the base is supported on four angles (legs) 50 * 50 * 300 mm (25). Driving motor (24) three phase, 2 horse powers, 1450 r.p.m and 380 volts was used to drive the machine.

A calibrated two springs (21) supported by two studs (18) and four bases (20, 22) to apply the required load between the drive and driven discs by the tightening nuts (19) to deflect the springs. Two dial gauges measurements range from 0 to 50 mm and accuracy 0.01 mm (23) were mounted to measure the deflection of the springs; this deflection represents the exerted load. Figures (2) represent a schematic layout of the machine.

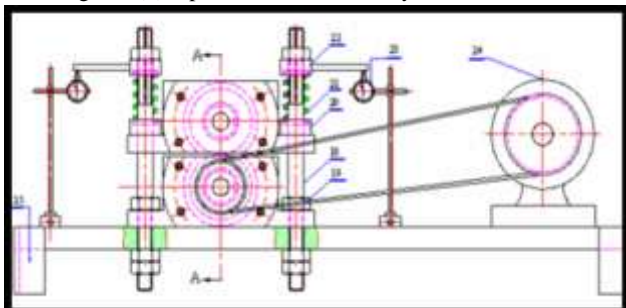


Fig (2) schematic layout of the machine test

3.3. Calibration Curve of spring: Calibrating curve for the two springs to apply the required load between the drive and driven rollers is shown in Fig. (3)

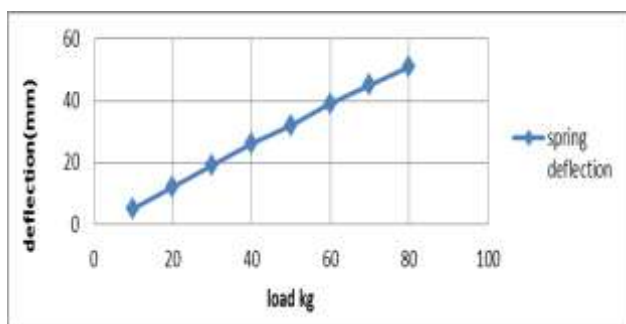


Fig (3) Calibration curve of spring

3.4. Wear Test Procedure

The procedure for wear test experiments can be summarized in the following steps: (1) Before each test, the discs were carefully cleaned. (2) Load: Tests were carried out at constant load of 20kg, the normal loads which were applied through two springs, were maintained constant during the period of test. (3) Speed : Speed designed rollers used for the purpose of converting speeds to obtain the required speeds and by country and energies of the electric motor from to(1000 - 1450 - 2000 r.p.m) .(4) The machine was stopped at time intervals for weighing the discs . Any loose debris at the surface of the disc specimens were removed by cleaning before weighing the specimens. (5) On restarting the wear tests, the discs were located in their supports in exactly the same orientation as before stopping the tests, in order to ensure that the wear in discs has occurred in the same direction throughout the test. (6) At the end of the test, the accumulated wear of the discs, expressed in mg. was plotted against the number of revolutions and the wear rate were calculated for each test material.

4. Results and discussion

4.1. Results of hardness test

Figure(4) represents the relationship between hardness and the percentage by additive of germanium, that the relationship between them is a direct relationship, the hardness of the alloy principally be the result of the solution rigid resulting from the melting of copper in zinc which is less hardness than other alloys, note the increased hardness with the increase in the proportion of germanium and be higher hardness ratio at adding of 6% germanium is due to increase hardness with increasing the proportion of germanium that this article has a high hardness its presence in the alloy increases the hardness as well as the work of minutes germanium to impede the movement of dislocations, and impeding the plastic deformation of the alloy, leading to increased hardness.

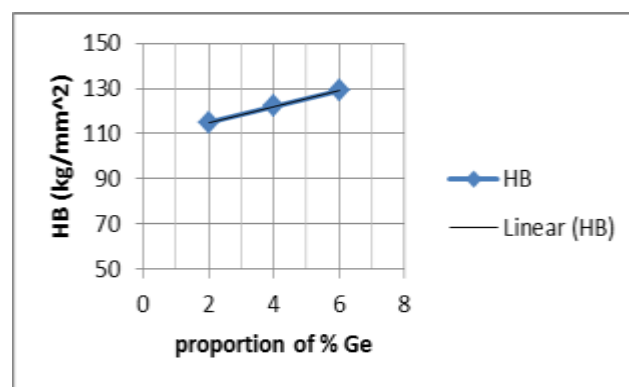


Fig (4) the relationship between hardness and the proportion of germanium.

4.2. Effect of percentage added germanium on the accumulated loss of weight to driving driven:

The major type of wear that take place in this experimental work is erosion. The weight loss of the impeller is due to the material removal from the impeller as a result of erosion wear. The entire testing was divided in three phases. The details of all three phases are mentioned below: First Phase: 1000 rpm, load 20kg as in Figure (5). Second Phase: 1450 rpm, load 20kg as in Figure (6), Third phase: 2000 rpm, load 20kg as in Figure (7). It was used in load all speeds of 20 kg and time 24 hr .The duration of each test rate three hours. Germanium has been studied weight ratios on the basis alloys and other alloys loss rate when the load (20kg) and different speeds (1000.1450.2000) rpm. the fig (5,6,7) note the relationship between the number of revolutions and weight losing rate where the relationship is directly proportional to each of the basis slug and alloys other and note that the basis slug have a loss larger than the other alloys weight rate and note less loss rate by weight in the alloy (B3_6%Ge). Any the element increase germanium least the of weight loss rate. This is due to the increase of the proportion of the added germanium element increases the hardness and as described in the hardness test where the hardness is inversely proportional to the rate of weight loss as reduce the (Plastic deformation). In the early stages of the sliding wear rate increase be greater than the closing stages when a high time periods, due to the time period

increase for the sliding lead increase .In flattening the bumps in both adjacent surfaces are obtained on the surface outcrops in which the proportion of a few, in addition to continuing to slide lead to a declamatory hardening of the surface of the Sample and thus lower metal loss rate. It is noted that the basis slug more affected by a time of sliding of overlapping material where noted that the metal loss rate decreases with the increase of the at germanium 6% and be less loss rate by weight and this goes back to the role of germanium element to increase the hardness of the sample and to reduce contact between surfaces adjacent and reduce the rate of loss by Weight.

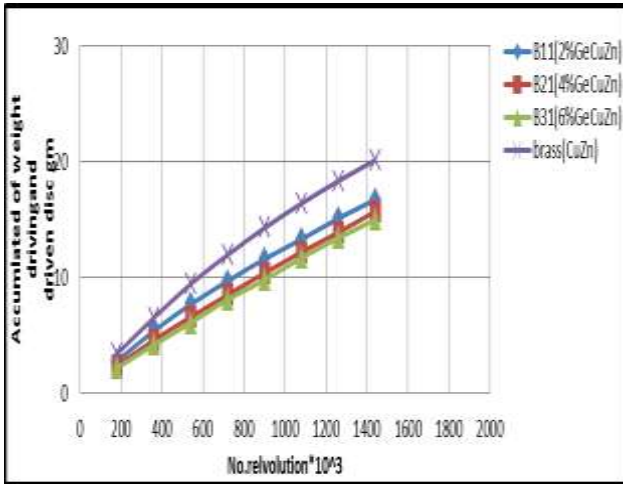


Fig (5) The variation of accumulated loss of weight of driving and driven discs versus the number of revolutions at different materials, (B11/B11”), (B21/B21”), (B31/B31”), at velocity (1000) r. p. m.

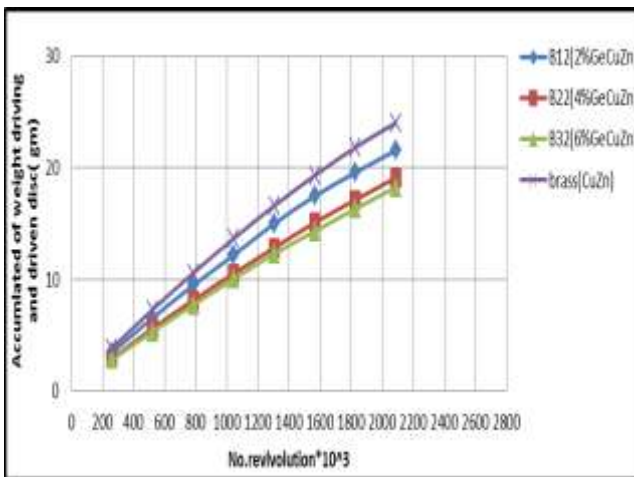


Fig (6) The variation of accumulated loss of weight of driving and driven discs versus the number of revolutions at different materials, (B12/B12”), (B22/B22”) (B32/B32”) at velocity (1450) r. p.m.

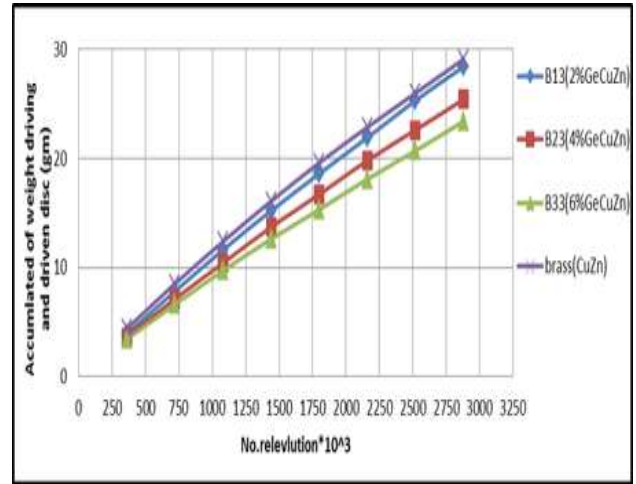


Fig (7) The variation of accumulated loss of weight of driving and driven discs versus the number of revolutions at different materials, (B13/B13”), (B23/B23”) (B33/B33”) at velocity (2000) r. p. m.

4.3. Effect of percentage of Added Ge% on the wear rate:

Effect add percentage of germanium on the wear rate of the basis alloy and other alloys at different speeds (1000-1450-2000) rpm and prove used load (20 kg) and time. It is the shape (8) note the relationship between the ratios added and the wear rate is where the relationship is inverse of each of the basis alloy and other alloys note that the basis alloy have the wear rate high and note less the rate wear in the alloy (B3_ 6% Ge) . Any that top element Germanium at wear rate least. This is due to the increase of the proportion of the additives element germanium increases the hardness

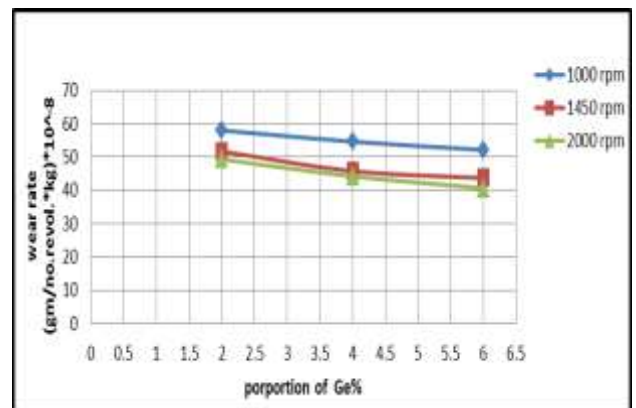


Fig (8) effect of the proportion of germanium on the wear rate at different speed

4.4. Effect of speed on the wear rate:

The effect of speed on the wear of the basis slug with other alloys prove load rate (20kg) and time (24 hours.). Where note of the form (9) with low wear rate increase the speed of the basis alloy and other alloys that wear rate Higher when a speed few can be Attributed to obtain partial fusion between the protrusions sliding surface due to the heat seeping from the sample surface at low velocities high and thus the force required to cut the points of contact between the protrusions is greater than the power of the metal interconnection, either low wear rate the speed increase of the slide it may be due to the heat leaking at speed few high slip and so result formed oxide layer on the contact surface which helps to decrease in the rate of wear.

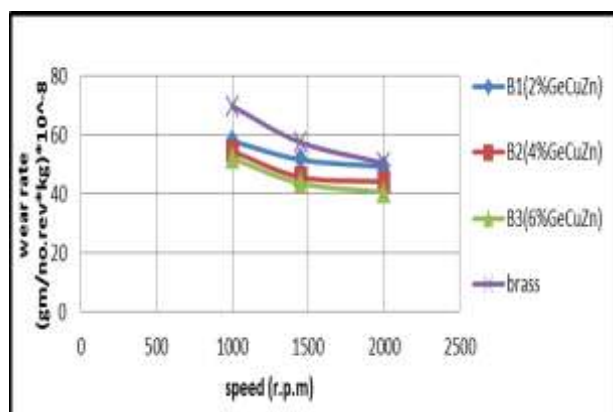


Fig (9) Effect of speed on the wear rate

4.5. Microstructure test:

Figure shows (10.a) which pictures the microscopic structure of brass when cast in sand .Which should, if cooled at an equilibrium rate, have shown nothing but a single solid solution. The photograph shows a marked dendritic structure indicating the gradation in composition in the crystals as they formed. If this casting should be annealed for a long time, the structure should become homogeneous. but for the forms (b,c,d),(fig 10) which shows the Microscopic structure of the alloy after the addition of germanium element and different proportions (Ge%2-6).

The Installation begins dendritic Change and improvement in infrastructure because of the work centers Terms of minutes, and noticed that the element germanium is distributed almost other inside the alloys. We also note that there is a light-colored area, which represent ground which is the solution solid such as copper and zinc.



(a)- Brass (Cu-Zn), 100 x



(b) - B1(2% GeCuZn) ,100x



(c)- B2 (4% GeCuZn), 100 x



(d) - B3 (6% GeCuZn), 100x

Fig (10) the microscopic structure of the alloys

5. CONCLUSIONS

1. Wear rate for all materials under investigation decreases with the increase of their case hardness. Minimum wear rate was obtained at hardness 129 HB.
2. Wear rate for all tested materials decreases with the increase of germanium. The addition of germanium to reduce the wear the alloys and the wear rate decrease increases with added lineage of germanium element and less wear rate was found when the proportion addition at 6%Ge.
3. Notes through graphics that increase the element germanium leads to the gradually reduce the rate of wear due to the increase of germanium element which increases the hardness and reduce the wear and tear of the metal.
4. Wear rate for material B3 (6%GeCu Zn) is less than that of the wear rate for B2 (4%GeCu Zn), B1 (2%GeCu Zn) and Base metal respectively under the same testing conditions at (1000-1450-2000) r.p.m.
5. Wear rate is reduced to basis alloy and other alloys and increase speed
6. Best alloy through the results that have been reached are B3(6%GeCuZn)at different speeds, which gives better resistance to wear and erosion that can through these specifications manufacturing pumps impeller.
7. Through the results obtained B3(6%GeCuZn) can be designed to pump speeds, which gives impeller erosion rate less, maintenance less and a possible pump to reduce the economic cost and long life impeller.

6. ACKNOWLEDGEMENTS

It is hard to begin to put into words how someone took me from a place I can only Describe as being in the dark into a place of light.Prof.Dr.Ahmed-EL-Bahloul,Ball provided that ray of sunshine that enabled me to complete this study. I will be indebted to him always.I would like to express my sincere gratitude. Dr.Miajdi.Samuel for his support and guidance, above and beyond the technical during my research

7. REFERENCES

- [1].Suhane.A,"Experimental Study on Centrifugal Pump to Determine the Effect of Radial Clearance on Pressure Pulsations, Vibrations and Noise",(*IJERA*),Vol.2, Issue4, July-August (2012), pp.1823-1829.
- [2]. majid.Z.A,mohsin R. and yusof .M.Z,"erosion wear of natural gas pipes due to high velocity jet physical examination and experimental study", *jurnal teknologi*, 56 (Sains & Kej.) Keluaran Khas (1), Dis. (2011),pp. 1–25.
- [3].Aiming.F, Jinming. L. and Ziyun.T. "Failure analysis of the impeller of a slurry pump subjected to corrosive wear", *Wear*, Vol. 181-183, (1995), pp. 876-82.
- [4].Sharma.A. K," numerical study of erosion wear on a Centrifugal slurry pump",MS,mechanical engineering deperment,thapar unversity patila, JUNE (2008),pp.11-14.
- [5].Jirout.T,F..I," Study of erosion wear of pitched blade impellers in a solid-liquid suspension", *Prosimy cytować jako: Inz. Ap. Chem.* (2009), 48, 4, pp. 58-59.
- [6].Gnanavelu.A.B,"A geometry independent integrated method to predict erosion wear rates in a slurry environment",Ph.D, University of Leeds, School of Mechanical Engineering, December(2010),p.13.
- [7].Patil. M. S, Deore E. R, Jahagirdar .R. S, Patil.S. V ,," Study of the Parameters -Affecting Erosion Wear of Ductile Material in Solid-Liquid Mixture, *World Congress on Engineering*, U.K,(2011), Vol III,p.1
- [8].dhinda.D.S,"parametric study of erosion wear of solid-liquid matrix",Ms,production and industrial engineering,thapar university , june(2011),p.6.
- [9].Kumar.R,"investigation of erosion wear of ductile material with and without coating" ,Ms,production industrial engineering,thapar university ,july (2011),ch1.p.4
- [10].www.Wikipedia.com,wear,this page was last modified on 13 may (2014) at 07:40.
- [11].Kristoffer.K.,McKee,Forbes.G,Mazhar.I, Entwistle.R and Howard.L.," A review of major centrifugal pump failure modes with application to the water supply and sewerage industries", *ICOMS Asset Management Conference*, May 16,(2011),PP.8.

Applications of Nano Technology in Pyro Industries located in Sivakasi

D. Edison Selvaraj
Dept. of EEE
Panimalar Engineering College
Chennai, India
edisonsivakasi@gmail.com

C. Pugazhendhi Sugumaran
Division of High Voltage
Engineering, College of
Engineering, Guindy
Anna University, Chennai
India

M. Rajkumar
Dept. of EEE
Dhanalakshmi Srinivasan College
of Engineering and Technology
Mamallapuram
Chennai, India

S. Geethadevi
Dept. of EEE
Aurora Scientific and
Technological Institute
Uppal, Hyderabad, India

J. Ganesan
Dept. of EEE
Sree Sowdambika College of
Engineering
Aruppukottai, India

Abstract: This paper deals with the application of nano technology in the pyro industries located in Sivakasi. This paper also gives information about the geography, history, location of industries, pyro powder manufacturing companies, application of SEM, ball mill present in Sivakasi. Sivakasi is one of the most mega industrial centres present in India. Sivakasi is also called as Kutti Japan due to the enormous amount of industries present in the heart of the city. It is one of the important holy places present in the country. It is having hot climate throughout the day. Nowadays, due to El - Niño the climate conditions were changed. There is an abundant rainfall in the summer season also. This paper is useful for the students to study about the pyro industries present in sivakasi and the applications of nano technology in the pyro industries present in the city. Hereafter, the pyro industries using the nano technology for the improvement of the quality and performance of the fireworks present in Sivakasi shall also be called “Nano pyro industries” and the city can also be called as “Nano Pyro Industrial City”. Pyro industries are present in the city due to the low annual rainfall and the dry climate present in the city throughout the year. The land in Sivakasi is also called as “Sulphur land” due to the heavy temperature in the city. Nowadays, the trend is changed due to the climatic changes caused by El – Niño. In the year 2015, the summer season in sivakasi was converted into rainy season by the climatic changes caused by the unstable changes in the winds from the Bay of Bengal.

Keywords: Ball Mill, Nano Powder, SEM, Pyro Industries

1. INTRODUCTION

This introduction chapter has three sub divisions:

1. A brief History and Geography of Sivakasi
2. A History of Industries in Sivakasi
3. A brief of Pyro industries in a Sivkasi

motors were widely used in fans, centrifugal pumps, blowers, lifts, cranes, hoists and so on. The efficiency of the induction motor depends upon the insulation used. For motors, the enamel was used for three purposes: impregnation, coating and adhesion. The efficiency of the induction motor can be increased by adding the nano fillers with the enamel which was used as coating for the windings of the motor. In this paper, the efficiency of the normal three phase squirrel cage induction motor and the Al_2O_3 nano filled enamel coated three phase squirrel cage induction motor was analyzed and the results were compared with each other [1].

1.1 A brief History and Geography of Sivakasi

Sivakasi has a history of more than 600 years. Its story starts from the 14 th century. Kaasi is a place where every devout Hindu is expected to visit once in their lifetime. Apart from that there are two other Kasi's in India - Tenkasi (meaning the Southern Kaasi) located near Courtallam, close to Kerala and Sivakasi (Kaasi of Siva) located at South of Madurai. It is interesting to note how Sivakasi came to be called so. The story starts as follows. Between 1428 and 1460 AD, King Harikesari Parakkirama Pandian then King of Tenkasi ruled the southern region of Madurai, with his capital at Tenkasi. He wanted to construct a temple for LORD SIVA at his place. Therefore he went to Kasi Varanasi and worshiped Lord Siva there and brought a Sivalingam from there. While returning to his place with the prized Linga a few miles past Madurai, he took rest under a groove of Vilva trees. The cow which carried Sivalingam, refused to move and also the King's wife (the Princess) attained puberty that night, which prohibited the carrying of the Linga to Tenkasi. He found that it was hard to

reach Tenkasi in time, to install the Sivalingam and he realised that the wishes of Lord SIVA were different from his own. As events thus overtook auspicious time for the already proposed plan of consecrating the Linga at Tenkasi, the king reverentially placed the Linga in the place where he had halted and proceeded to Tenkasi. The place which was sanctified by the "Sivalinga brought from Kasi", henceforth came to be called Sivakasi. Later on King Pandia and King Thirumalai Naicker did a lot for this temple, named it "KASI VISWANATHA SWAMY" Temple [1]. The period of construction was between 15th and 16th century. Aanaiaappa Gnani reconstructed this temple. Under the rule of King Naickers, the temple was developed more. In 1659, the Ratham (the chariot) was constructed by Muthu Veerappa Naicker. The Title Name 'KUTTY JAPAN' was given by Mr. Jawaharlal Nehru (First Prime Minister of INDIA) to Sivakasi. 'Kutty' in Tamil means Mini. So Kutty Japan, means Mini Japan. During early 1960's India was under great famine and lots and lots of people are unemployed and it was the time, the people of Sivakasi came in hand in hand with each other to promote themselves without expecting any aid from the Government and stood on their own to achieve self reliant, high industrial growth rate (especially Matches, Fireworks, Printing and sub industries related to those industries). Until 1985 Sivakasi was a part of Ramanathapuram District. When Ramanathapuram District was trifurcated Sivakasi became a part of Virudhunagar District. It is 70Kms south of Madurai. Sivakasi is a black soil plains region. The soils are of poor productivity and are mainly black loamy soil (locally known as (Karisal). Cotton, pulses, oilseeds and millets, which do not require much irrigation, are the main crops grown. The climate of the Sivakasi is semi-arid tropical monsoon type. It has a high mean temperature and a low degree of humidity. The temperatures range from 20° C to 37° C. April, May and June are the hottest months of the year. Sivakasi receives scanty rainfall with an annual average of 812 mm. The South West monsoon which sets in June and lasts till August brings scanty rain. The bulk of the rainfall is received during the North East monsoon in the months of October, November and December. Vembakottai Reservoir supplies the drinking water to Sivakasi.

1.2 A History of Industries in Sivakasi

Like JAPAN (world leader in Electronics), Sivakasi is leader for Printing, Fireworks, Safety matches Production. So the name was given to Sivakasi. This happened only because of the people of Sivakasi, who are more dedicated committed to hard work and their togetherness to achieve attitude. The key behind this success story of each and every Sivakasians is "QUALITY with QUANTITY, HARD WORK & Commitment to work, and Attitude of Togetherness. Hats off especially to the Nadar Community whose contributions are lot to this achievement. Like Ayya Nadar, Graha Durai Nadar, Shanmuga Nadar, KAKA Kaliappa Nadar. In 1922 Mr. P.Ayya Nadar and Mr. A.Shanmuga Nadar went to Calcutta and learnt the art of safety matches manufacture. Next year they established the company 'The South India Lucifer Match Industry'. It was the starting point of the modern industrialized Sivakasi which caters safety matches, fireworks and printing to the whole India. In turn, Sivakasi

- Contributes 80 % of India's Total Safety Matches Production
- Contributes 90 % of India's Total Fireworks Production
- Contributes 60 % of India's Total Offset Printing Solutions.

- Is one of the high Sales / Excise / Customs Duty paying town.
- Is 100 % employment achieved town (which is among a few towns in India rather world)

In Short, Sivakasi is a big industrial centre in Virudhunagar district of Tamilnadu state in India and well known all over India for its fireworks, safety matches and printing. Sivakasi is one of the highest Sales / Excise / Customs Duty paying towns in India. Enterprising and work conscious people of Sivakasi have made it one of the leading industrial towns of India in short span of time. Sivakasi is the town in India where unemployment does not exist. On witnessing the industriousness of Sivakasi people. Pandit Jawaharlal Nehru, the first Prime Minister of India optly nick named Sivakasi as "Mini Japan" ("Kutty Japan" in Tamil and "Chotta Japan" in Hindi). Sivakasi is India's fireworks hub. 90% of India's fireworks is produced in Sivakasi. A not only firework, Sivakasi is the hub of safety matches and offset printing solutions also. 80% of India's safety matches are produced in Sivakasi and 60% of India's offset printing solutions is produced in Sivakasi [2].

1.3 A brief of Pyro industries in Sivakasi

Sivakasi is the natural choice for fireworks production. Low rain fall and a dry climate prevailing in the Sivakasi area contribute to unabated production. What could have been consumed in three hours of the Diwali Day came to be produced in 300 days, almost with overtime jobs throughout the year. In Sivakasi the first fireworks industry was started in the early 20th century. Having achieved a measure of success in Safety Matches, Colour Matches and Star Matches, Mr. A Shanmuga Nadar and Mr. Iya Nadar ventured upon the making of sparklers –then the most popular item in the Small Fireworks family, which were at the time imported from the UK and Germany. The germinal seed for the making of modern family Fireworks or Small Fireworks was planted in the year 1934 when the Central Excise Duty on Matches was promulgated. Until the outbreak of World War II in 1939, there were only a handful of factories in Sivakasi, Trichur and rimjalakuda in Kerala State. From 1938 to 1944 the import of fireworks and firecrackers was obstructed by war. This shortage gave a fillip to the indigenous industry, which was in its infancy. During the year 1940, the Indian Explosives Rules were enacted whereby a system of licensing was introduced for manufacture, possession and sale. Thus came to be set up in the year 1940 the first organized factory with several precautions and safety measures. The shortage in the market helped these, then seasonal, factories to work even during off-season and build up stocks. With World War II coming to an end and the gateway for import of raw materials having been reopened, the indigenous industry enlarged itself. Not only the existing factories broadened their efforts, there came into existence several new units, of which National Fireworks, Kaliswari Fireworks and Standard Fireworks were prominent in the year 1942. These three factories started marketing their products throughout the length and breadth of India. These were later supplemented by new units at the average of 10 per year. What started as 1 or 2 factories in 1923, rose to 3 in 1942, and by the year 1980 the number of factories had risen to 189. By the end of 2011 the total number of factories was 850 in Sivakasi alone. Sivakasi is known throughout the world for fireworks production. 90% of India's fireworks is produced here. The fireworks industry in Sivakasi is worth between Rs 2000-6000 crore. The market for fireworks is

likely to grow at the rate of 10% per annum. There are nearly 850 fireworks factories giving direct employment to about 40,000 workers and about 4 lakh indirect such as paper tube making, wire cutting, box making in the country side. Fireworks in Sivakasi also produce Military Weapons training items. They are used for training in armed forces. Some airports are using Sivakasi rocket to scare away birds to avoid bird hits of aircrafts.

2. APPLICATIONS OF ALUMINIUM POWDERS IN PYRO TECHNOLOGY

Aluminium powders are used in pyro industries for the manufacture of

- Heavy Crackers
- Garland Crackers
- Wheels
- Heavy Volcanoes
- Aerial Display Fireworks

Pyrotechnic Aluminium powders are manufactured by Sri Kaliswari Metal Powders Private Limited, Sivakasi. They are the leading manufacturers of the following products:

- Aluminium powders,
- Aluminium paste,
- Aluminium oxide powder,
- Ferro aluminium powder,
- Air atomized aluminium powder,
- Pyrotechnic aluminium powder,
- Cellular concrete aluminium powder and
- Aluminium paste in MTO, naphtha, toluene & xylene bases,
- Aluminium oxide powder,
- Industrial metal powder

3. MANUFACTURING PROCESSES INVOLVED IN METAL POWDER COMPANIES

The following processes are carried out in this manufacturing company:

- Pyrotechnic Aluminium Powder or foil is propelled into a charging bin along with grease
- The milling process is carried out in the ball mill
- After a pre-determined time, the powder is pneumatically driven into a cyclone
- In the cyclone, the heavier particles get separated and are returned to the ball mill for further milling.
- SEM analysis of prepared powders

3.1 Ball Milling

Ball mill is an efficient tool for grinding many materials into fine powder. The ball mill is used to grind many kinds of mine and other materials. It is widely used in chemical industry. There are two ways of grinding: dry process and the wet process [2]. The ball mill is key equipment for regrinding. It is widely used for the cement, the silicate product glass, ceramics and etc. Here Aluminium trioxide nano material is synthesized by using ball mill to convert micro particles to nano particles.

- The pulverisette 6 planetary monomill is universally applicable for quick dry or wet grinding of inorganic and organic samples for analysis, quality control, materials.

- The sample material is crushed and disintegrated in a grinding bowl by grinding balls.
- The grinding balls and the material in the grinding bowl are acted upon by the centrifugal forces due to the rotation of the grinding bowl about its own axis and due to the rotating supporting disc.
- As a frictional effect, the grinding balls running along the inner wall of the grinding bowl, and impact effect, the balls impacting against the opposite wall of the grinding bowl.

3.2 SEM Analysis of Alumina powders used in Pyro Industries

Scanning electron microscopy uses a focused high energy electron beam to image the surface of a variety of samples and collect information on morphology and elemental composition [3]. A scanning electron microscope is a highly versatile tool and can be used to study biological specimens, geological materials, nano particles, circuit boards, and many other sample types [7]. A SEM consists of an electron gun, focusing lenses, stage or specimen holder, and several types of detectors. The electron gun contains a heated metallic filament, usually tungsten, which provides the source of electrons. These electrons are accelerated toward an anode plate and then focused by condenser lenses and an objective lens. A deflector coil causes the focused electron beam to be scanned across the surface in a raster pattern [4].

There are two types of electron microscope – the scanning electron microscope (SEM) and the scanning transmission electron microscope (STEM). The samples must be conducting (in order to accelerate electrons into the sample) and hence a biological sample must have a gold layer deposited on its surface if it is to be investigated by SEM or STEM. In the STEM, the sample is a very thin specimen and contrast within the image is due to the spatial variations in intensity of the transmitted electron beam through the specimen, as the beam is raster scanned over the specimen. In SEM, the image may be produced in a number of ways from variations in the intensity of secondary electrons back-scattered from the specimen through to X-ray emission produced by inelastic collisions of the primary beam with bound electrons in the specimen [6]. The idea that gave rise to the electron microscope is that, just as light is refracted and focused by an optical lens, the electron, due to its charge, will produce Cambridge Instruments Ltd.

The electrons are emitted by an incandescent cathode source, accelerated towards more positive grids through either electrostatic or magnetic field lens onto an object. The specimen is supported on a very thin film to minimize the scattering of the electrons as they pass through the sample. Depending on the thickness and composition of the object, the electron beam experiences different attenuation as a function of position. The beam travels through two more lenses before being imaged onto a fluorescent screen (in original models) or photographic plate or directly onto a scintillator placed on the face of a photomultiplier tube or a CCD device [5].

(A scintillator is a semi-transparent material, which emits a flash of light when a charged particle traverses it) The spatial resolution of this type of microscope is determined by the wavelength associated with the electrons and this wavelength may be 100,000 times smaller than optical wavelengths at the typical accelerating voltages used in electron microscopy. Figures 1 – 3 show the SEM images before ball mill whereas figures 4 – 6 show the SEM images after ball mill of alumina powders used in Pyro industries [8].

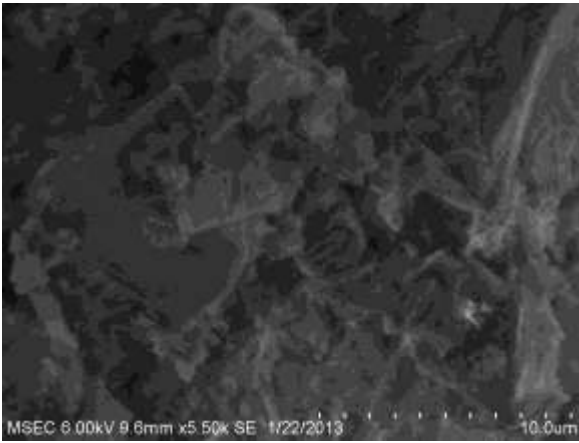


Figure 1

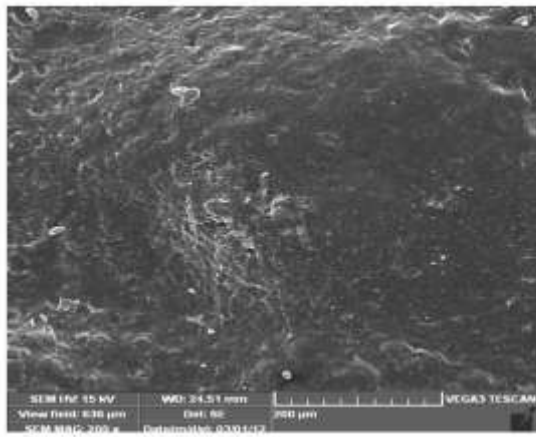


Figure 2

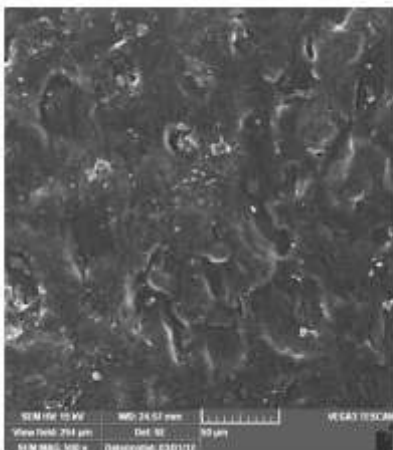


Figure 3

Figures 1 - 3 SEM analysis before ball mill

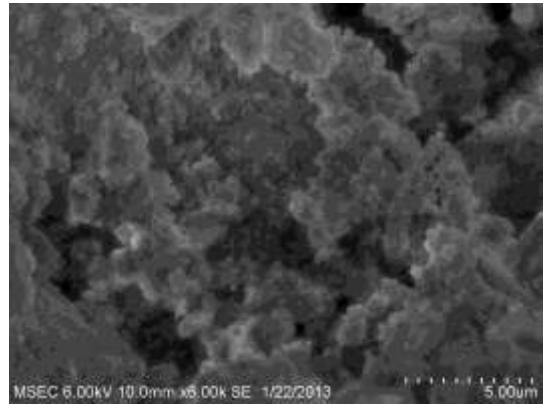


Figure 4

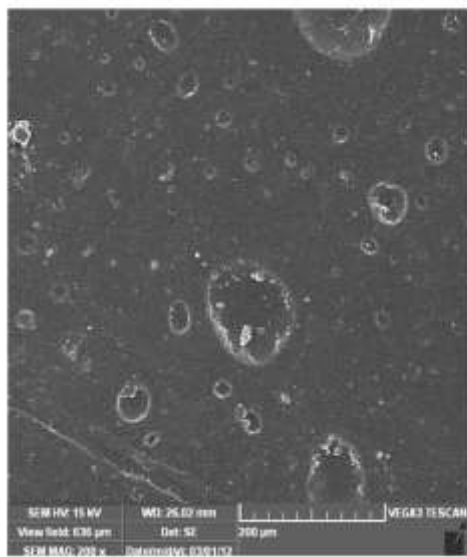


Figure 5

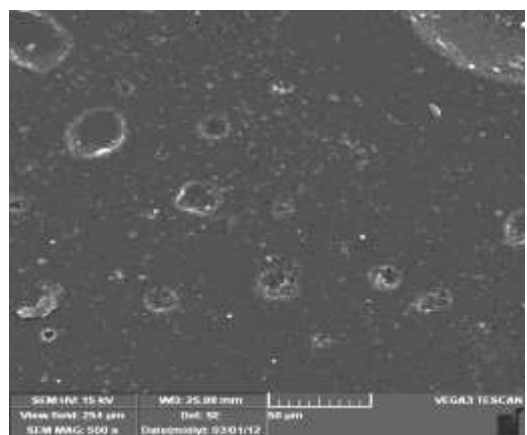


Figure 6

Figure 4 – 6 SEM Analysis after ball mill

4. PROBLEMS FACED BY INDUSTRIES IN SIVAKASI

The most important problems faced by the pyro industries present in Sivakasi are

1. Introduction of china crackers in Indian Market caused some decrease in the manufacture of pyro products and selling of pyro products.
2. Heavy summer in North India caused low pyro orders from North Indians to celebrate Diwali with pyro products.
3. Small roads causing frequent traffic in Sivakasi
4. Accidents in Sivakasi due to fireworks causing fear among the workers to work in pyro industries.
5. Poorly equipped Hospitals for the treatment of persons affected by fire accidents.
6. Encroachments in roads present in Sivakasi causing heavy traffic and congestion in the city for the workers and causing road accidents in the city.
7. Poor infrastructure in the city to handle the road traffic and persons affected by fire accidents.
8. People are affected by low income for their hard work. North Indians are replacing the native workers present in Sivakasi for low wages offered to them.

Government has to take necessary steps to improve the roads, infrastructure of Sivakasi to avoid road accidents and death caused by fire accidents during the movement of persons to the Hospitals. Government has to take necessary steps to improve the wages to the workers. Government has to extend the roads, construct flyovers to avoid road accidents and to avoid traffic in the city.

5. CONCLUSION

This paper has dealt with the important information about the pyro industries present in Sivakasi. This paper has also suggested some necessary steps to improve the quality of pyro industries present in Sivakasi to avoid frequent accidents in the plants. Workers have to be well equipped with necessary development programmes and safety equipments to handle the explosive elements present in the industries. Infrastructure in Sivakasi has to be improved to avoid traffic, deaths during fire accidents under their movement to hospitals by the small roads present in the city. Hospitals should be well equipped with fire treatment devices and medicines. The nano technology would improve the quality and performance of pyro industries present in Sivakasi.

6. REFERENCES

- [1] <http://www.sivakasonline.com>
- [2] <http://www.kuttyjapan.com>
- [3] Edison Selvaraj. D, et.al "Estimation of Losses on 3Φ Nano Coated Induction Motor" Applied Mechanics and Materials Vol.666 (2014) pp. 213-217 (2014) Trans Tech Publications, Switzerland.
- [4] Edison Selvaraj. D, Pugazhendhi Sugumaran. C, Lieutenant Ganesan. J, Ramathilagam. J, "Analysis of Dielectric and Thermal Properties of Polyamide

Enamel Filled with Carbon Nano tubes"
International Journal of Nano science, Vol.12,
Issue 3, June 2013.

- [5] Edison Selvaraj, D., C. Pugazhendhi Sugumaran, and A. Sivaprakash "Characterization of Electrical and Thermal Properties of Enamel Filled with Carbon Nanotubes", Proceedings of the Third International Conference on Trends in Information, Telecommunication and Computing, Springer New York, 2013.
- [6] Selvaraj, D. E., Priyan, S. S., Joshi, M. R., Sugumaran, C. P., Kannan, R., Raj, R. A., Kumar, B. M., Prakash, R., Ganesan, J., Krishnamoorthi, D., & Kumar M. R, "A Review on The Nano Fillers Used for Electrical Apparatuses", Journal Club for Electrical Engineering (JCEE), Vol.1, Issue 1, pp 8 - 17, Aug 2014.
- [7] Selvaraj, E. D., Priyan, S. S., Joshi, M. R., Sugumaran, C. P., Kumar, B. A., Kumar, M. A., Kumar, S. A., Khan, A. H., Kannan, R., Ganesan, J., Kumar, R., Kumar S. D, "A Review on the Fabrication Methods Used in Nano Technology for The Fabrication of Nano Fillers Used in Electrical Apparatuses", Journal Club for Electrical Engineering (JCEE), Vol.1, Issue 1, pp , Aug 2014.
- [8] Joshi MR Selvaraj DE, Kumar GS, Mohan BR, Sugumaran CP, Kumar RM, Ganesan J, "A Lecture Notes for Understanding the Fundamentals of Fabrication of Nano Fillers", Journal Club for Electrical Engineering (JCEE), Vol.1, Issue 2, pp 1 - 16, Oct 2014.

Fatty Acid Pattern and Alkaloids of *Echium Rauwolfii*

Abdelaziz M. Dawidar
Chemistry Department
Faculty of Science
Mansoura University
Egypt

Abdul-Sattar H. A Ghani
Chemistry Department
Faculty of Science
Mansoura University
Egypt

Maha M. Alshamy
Botany Department
Faculty of Science
Mansoura University
Egypt

Eman H. Tawfik
Chemistry Department
Faculty of Science
Mansoura University
Egypt

Mamdouh Abdel-Mogib
Chemistry Department
Faculty of Science
Mansoura University
Egypt

Abstract: The GC/MS analysis of hexane extract revealed the presence of palmitic acid as saturated fatty acid (1.05%), versus oleic acid (2.18%), linoleic acid (1.13%), cis-8,11,14-eicosatrienoic acid (2.12%) as unsaturated fatty acids. On the other hand, CH₂Cl₂ extract contained palmitic acid methyl ester (3.55%), and methyl isostearate (1.17%) as saturated fatty acids, versus linoleic acid methyl ester (3.57%) and linolenic acid methyl ester (10.01%) as unsaturated fatty acids. The GC/MS analysis of the alkaloid-rich fraction indicated the presence of the pyrrolizidine alkaloids petranine (2.97%), 7-angeloyl-9-(2-methylbutyryl) retronecine (4.22%), 7-angeloylretronecine (0.59%) and 9-angeloylretronecine (0.47%).

The butanol extract showed the heights DPPH radical scavenging activity (IC₅₀ = 14.3 µg), while ethyl acetate extract was very weak in activity (IC₅₀ = 432.3 µg) and no activity with hexane and methylene chloride extract.

The antimicrobial potentials of *E. rauwolfii* extracts were examined. The inhibition of the fungi species by ethyl acetate extract exert was comparable to Amphotericin B. The inhibition zone of the butanol extract against *Streptococcus pneumonia* was comparable to Ampicillin, against *Pseudomonas aeruginosa* was comparable to Gentamicin and *Escherichia coli* was comparable to Gentamicin.

The cytotoxicity against HePG-2 of ethyl acetate extract and butanol extract were “very strong”, and that of hexane extract and methylene chloride extract were “moderate”, against MCF-7 of ethyl acetate extract and butanol extract were “strong”, that of methylene chloride extract was “moderate”, and that of hexane extract was “weak” and against HCT-116 of butanol extract was “very strong”, of ethyl acetate extract was “strong”, of methylene chloride extract and hexane extract were “moderate”.

Keywords: fatty acids, pyrrolizidine alkaloids, *Echium rauwolfii*, Boraginaceae

1. INTRODUCTION

Echium rauwolfii Delile (Boraginaceae) is an erect or ascending hispid-setose annual winter herb with branched stems [1]. About 40 species of *Echium* are known that are mainly distributed in the Mediterranean region, Western Asia and Southern Europe [2, 3]. The genus is represented by about 7 species in Egypt, including *E. rauwolfii* [1].

Echium seeds contain specialty oil; it has many potential uses in the pharmaceutical industry for treatment of eczema, acne, and other skin disorders and in the cosmetic and personal care products industry. *Echium* oil is applied topically to reduce skin wrinkles and protects and moisturizes the skin from sun exposure [4]. As a chemical class, pyrrolizidine alkaloids are some of the leading plant-based toxins associated with

harmful effects in both humans and animals [5, 6]. However, the antioxidant, antimicrobial and anti cancer (Hep-G2, HCT-116 and MCF-7) activities, that we will introduce here, do not confirm this situation, so that, we have interested here to introduce the results of inspection of both the fatty acid and the pyrrolizidine alkaloid patterns.

2. EXPERIMENTAL

2.1 GC/MS

The GC/MS analysis was performed at Agriculture Research Center, National Research Center (NRC), Dokki, Cairo, Egypt, using a Thermo Scientific, Trace GC Ultra / ISQ Single Quadrupole MS, TG-5MS fused silica capillary column (30 m, 0.251 mm, 0.1 mm film thickness). For GC/MS detection, an electron ionization system with ionization energy of 70 eV was used, Helium gas was used as the carrier gas at a constant flow rate of 1 mL/min. The

injector and MS transfer line temperature was set at 280°C. The oven temperature was programmed at an initial temperature 40°C (hold 3 min) to 280°C as a final temperature at an increasing rate of 5°C /min (hold 5 min). The quantification of all the identified components was investigated using a percent relative peak area. A tentative identification of the compounds was performed based on the comparison of their relative retention time and mass spectra with those of the NIST, WILLY library data of the GC/MS system.

2.2 Solvents

Hexane (60-80°C) was obtained from Alpha Chemika; methylene chloride was obtained from SDFCL sd fine-chem limited; ethyl acetate, methanol, butanol and acetone were obtained from Adowic.

2.3 Cell lines

Hepatocellular carcinoma HePG-2, mammary gland breast cancer MCF-7 and colorectal carcinoma HCT-116. The cell lines were obtained from ATCC via Holding company for biological products and vaccines (VACSERA), Cairo, Egypt.

2.4 Chemical reagents

The reagents RPMI-1640 medium, MTT, DMSO and 5-fluorouracil (sigma co., St. Louis, USA), Fetal Bovine serum (GIBCO, UK). 5-fluorouracil was used as a standard anticancer drug for comparison.

2.5 Plant material

Echium rauwolfii Delile was collected in March 2014 at Hibis Temple from arable land-side of cultivation in EL Kharga Oasis which, Western Desert, Egypt. It was identified by the 4th author according to [1, 7] and [8]. A herbarium specimen was deposited in the Herbarium of Botany Department, Faculty of Science, Cairo University.

2.6 Processing of plant material

The collected plant material was dried in shade and grinded at room temperature to give (181.760 g) of dried powder material. The plant material was extracted by soxhlet extractor with hexane, followed by methylene chloride, then ethyl acetate, and finally butanol to give extracts (5.780, 2.200, 1.49, 58.21g, respectively).

A sample of hexane extract was analyzed using GC/MS technique to give: 1-hexadecanol (R_t 31.09 min, 2.26%), 1-octadecanol (R_t 36.51 min, 4.18%), nonadecane (R_t 39.18 min, 0.91%), 1-eicosanol (R_t 41.43 min, 3.27%), eicosane (R_t 41.57 min, 1.15%), palmitic acid (R_t 45.67 min, 1.05%), oleic acid (R_t 45.93 min, 2.18%), linoleic acid (R_t 48.16 min, 1.13%), cis-8,11,14-eicosatrienoic acid (R_t 48.32 min, 2.12%), pentacosane (R_t 52.12 min, 2.70%), heptacosane (R_t 55.79 min, 1.81%), nonacosane (R_t 59.21 min, 1.96%), nonacosanol (R_t 61.12 min, 1.19%), hentriacontane (R_t 62.42 min, 2.97%).

A sample of CH₂Cl₂ extract was analyzed by GC/MS technique to give: hexadecane (R_t 31.29 min, 1.31%), octadecane (R_t 36.68 min, 0.94%), palmitic acid methyl ester (R_t 39.91 min, 3.55%), eicosane (R_t 41.57 min, 0.60%), linoleic acid methyl ester (R_t 43.82 min, 3.57%), linolenic acid methyl ester (R_t 43.97 min, 10.01%), methyl isostearate

(R_t 44.54 min, 1.17%), docosane (R_t 46.04 min, 0.45%), tetracosane (R_t 50.16 min, 0.47%), pentacosane (R_t 52.09 min, 0.86%), hexacosane (R_t 53.97 min, 0.90%), heptacosane (R_t 55.77 min, 0.72%).

A sample of plant material (135.000 g) was soaked in methanol (1L) for 24 h filtered, and the filtrate was evaporated to 1/4 the initial volume. The extract was diluted with water and acidified with hydrochloric acid, then extracted by CH₂Cl₂. The aqueous acidic layer was basified to pH 9 by adding ammonium hydroxide and then extracted again by CH₂Cl₂ to give the alkaloid-rich fraction (22.610 g).

A sample from the alkaloid-rich fraction gave by GC/MS: trans 3-pinanone (R_t 19.80 min, 3.90%), petranine (R_t 21.12 min, 2.97%), endobornyl acetate (R_t 23.78 min, 1.90%), 7-angeloyl-9-(2-methylbutyryl)retronecine (R_t 27.50 min, 4.22%), 7-angeloylretronecine (R_t 28.22 min, 0.59%), 9-angeloylretronecine (R_t 29.28 min, 0.47%), 14-methylpentadecanoic acid methyl ester (R_t 42.26 min, 0.40%), eicosane (R_t 43.98 min, 0.58%), heneicosane (R_t 46.30 min, 0.87%), docosane (R_t 48.52 min, 1.50%), tricosane (R_t 50.66 min, 2.42%), hexanedioic acid, dioctyl ester (R_t 52.72 min, 24.04%), pentacosane (R_t 54.68 min, 4.48%), hexacosane (R_t 56.57 min, 4.16%), heptacosane (R_t 58.41 min, 2.75%), octacosane (R_t 60.17 min, 1.69%).

2.7 Evaluation of biological activity of the plant extracts

2.7.1 Antioxidant activity

The antioxidant activity of extract was determined at the Regional Center for Mycology and Biotechnology (RCMB) at Al- Azhar University by the DPPH free radical scavenging assay in triplicate and average values were considered. Freshly prepared (0.004% w/v) methanol solution of 2,2-diphenyl-1-picrylhydrazyl (DPPH) radical was prepared and stored at 10°C in the dark. A methanol solution of the test compound was prepared. A 40ml aliquot of the methanol solution was added to 3ml of DPPH solution. Absorbance measurements were recorded immediately with a UV-visible spectrophotometer (Milton Roy, Spectronic 1201). The decrease in absorbance at 515 nm was determined continuously, with data being recorded at 1 min intervals until the absorbance stabilized (16 min). The absorbance of the DPPH radical without antioxidant (control) and the reference compound ascorbic acid were also measured. All the determinations were performed in three replicates and

averaged. The percentage inhibition (PI) of the DPPH radical was calculated according to the formula:

$$PI = \left[\frac{(AC - AT)}{AC} \times 100 \right]$$

Where AC = Absorbance of the control at t = 0 min and AT = absorbance of the sample+DPPH at t = 16 min [9].

2.7.2 Antimicrobial activity assessment

Extracts were individually tested against a panel of Gram positive (*Staphylococcus aureus*), Gram negative bacteria (*Escherichia coli*) and fungi (*Candida albicans*). Each of the extracts was dissolved in DMSO (1 mg /ml). Whitman filter paper discs were cut with standard size (5 mm) and sterilized in an autoclave. The paper discs were soaked in the desired concentration of the extracts and placed aseptically in the Petri dishes containing nutrient agar media (agar 20 g + beef extract 3 g + peptone 5 g) and seeded with *Staphylococcus aureus*, *Escherichia coli* and *Candida albicans*. The Petri dishes were incubated at 36°C and the inhibition zones were recorded after 24 h of incubation. Each treatment was replicated three times. The antibacterial activity of a common standard antibiotic Ampicillin, Gentamicin and antifungal Amphotericin B was also recorded using the same procedure as above at the same concentration and solvents. The % activity index for the extract was calculated by the formula:

$$\% \text{ Activity Index} = \frac{\text{Zone of inhibition of test extract (diameter)}}{\text{Zone of inhibition by standard (diameter)} \times 100}$$

2.7.3 Cytotoxicity MTT assay [10, 11]

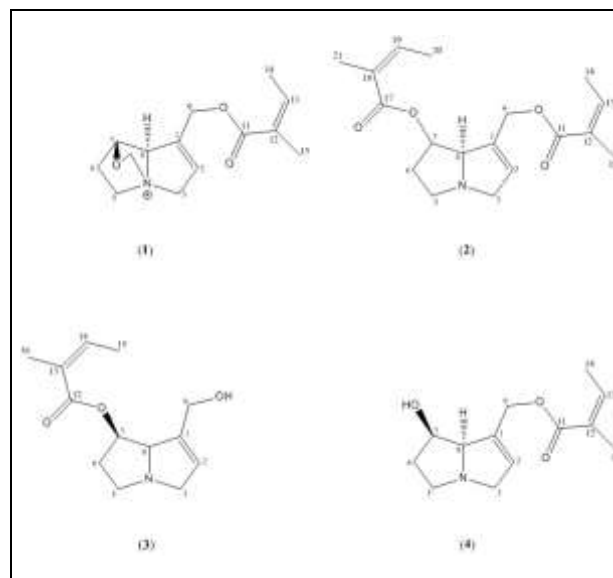
The cell lines HePG-2, MCF-7 and HCT-116 were used to determine the inhibitory effects of extracts on cell growth using the MTT assay. This colorimetric assay is based on the conversion of the yellow tetrazolium bromide (MTT) to a purple formazan derivative by mitochondrial succinate dehydrogenase in viable cells. The cells were cultured in RPMI-1640 medium with 10% fetal bovine serum. Antibiotics added were 100 units/ml penicillin and 100 µg/ml streptomycin at 37°C in a 5% CO₂ incubator. The cells were seeded in a 96-well plate at a density of 1.0 x 10⁴ cells/well [12]. At 37°C for 48 h under 5% CO₂. After incubation the cells were treated with different concentrations of extracts and incubated for 24 h. After 24 h of treatment, 20 µl of MTT solution at 5 mg/ml was added and incubated for 4 h. Dimethyl sulfoxide (DMSO) in volume of 100 µl is added into each well to dissolve the purple formazan formed. The colorimetric assay is measured and recorded at absorbance of 570 nm using a plate reader (EXL 800). The relative cell viability in percentage was calculated as (A₅₇₀ of treated samples/A₅₇₀ of untreated sample) X 100.

3. RESULT AND DISCUSSION

3.1 Fatty acid and alkaloid pattern

Many *Echium* species are characterized by the presence of polyunsaturated fatty acids [13]. The GC/MS analysis of the volatile fractions (hexane extract and methylene chloride extract) revealed the presence of palmitic acid as saturated fatty acid (1.05%), versus oleic acid (2.18%), linoleic acid (1.13%), cis-8, 11, 14-eicosatrienoic acid (2.12%) as unsaturated fatty acids in the hexane extract. On the other hand, the GC/MS analysis of CH₂Cl₂ extract gave palmitic acid methyl ester (3.55%) and methyl isostearate (1.17%) as saturated fatty acids, versus linoleic acid methyl ester (3.57%) and linolenic acid methyl ester (10.01%) as unsaturated fatty acids.

The GC/MS analysis of the alkaloid-rich fraction indicated the presence of the pyrazolidine alkaloids petranine **1** (2.97%), 7-angeloyl-9-(2-methylbutyryl) retronecine **2** (4.22%), 7-angeloylretronecine **3** (0.59%) and 9-angeloylretronecine **4** (0.47%). **1** and **4** was identified previously from *Echium glomeratum* [14], **2** and **3** was identified previously from *Echium rauwolfii* and *horridum* [15]. The structures as the following figures:



3.2 Antioxidant activity evaluation

The free radical of 2, 2-diphenyl-1-picrylhydrazyl (DPPH) is used for detection of the antioxidant activity of the extracts [8]. The butanol extract showed the heights scavenging activity (IC₅₀ = 14.3 µg, Table 1), while ethyl acetate extract was very weak in activity (IC₅₀ = 432.3 µg, Table 1) and no activity with hexane and methylene chloride extract when tasted at concentration ranged from (10- 5000 µg/ml).

Table 1: DPPH radical scavenging activity (IC₅₀ µg/ml)

Sample code	DPPH radical scavenging activity (IC ₅₀ µg/ml)
Hexane extract, Er1	-ve
Methylene chloride extract, Er2	-ve
Ethyle acetate extract, Er3	432.3
Butanol extract, Er4	14.3
Ascorbic acid	14.2

-ve: no activity even when tasted at concentration ranged from (10- 5000 µg/ml).

3.3 Antimicrobial activity assessment

The antimicrobial potentials of *E. rauwolfii* extracts were examined by the disc diffusion assay method, using eight pathogenic microbial species; *Aspergillus fumigates*, *Syncephalastrum racemosum*, *Geotricum candidum*, *Candida albicans*, represent pathogenic fungal species. *Streptococcus pneumonia*, *Bacillis subtilis*, represents Gram positive bacteria, *Pseudomonas aeruginosa*, *Escherichia coli*, represent Gram negative bacteria. The data were presented in Table 2. The results showed that there were remarkable inhibitions of the microbial growth against the tested extracts. The inhibition zones of ethyl acetate extract (Er3) against the fungi species were comparable to Amphotericin B. The inhibition zone against the Gram-positive bacteria *Streptococcus pneumonia* of the butanol extract (Er4) was comparable to Ampicillin. The inhibition zones of the butanol extract (Er4) against the Gram-negative bacteria *Pseudomonas aeruginosa* were comparable to Gentamicin. The inhibition zones of the ethyl acetate extract (Er3) and the butanol extract (Er4) against the Gram-negative bacteria *Escherichia coli* were comparable to Gentamicin.

3.4 Cytotoxicity assessment

Table 3 indicated the relative viability of cells (%) and table 4 indicated the in-vitro cytotoxicity IC₅₀ (µg/ml). The cytotoxicity against HePG-2 of ethyl acetate extract (Er3) and butanol extract (Er4) were “very strong”, and that of hexane extract (Er1) and methylene chloride extract (Er2) were “moderate”, against MCF-7 of ethyl acetate extract (Er3) and butanol extract (Er4) were “strong”, that of methylene chloride extract (Er2) was “moderate”, and that of hexane extract (Er1) was “weak” and against HCT-116 of butanol extract (Er4) was “very strong”, of ethyl acetate extract (Er3) was “strong”, of methylene chloride extract (Er2) and hexane extract (Er1) were “moderate”.

Table 2: The inhibition zone in mm of extracts of *E. rauwolfii* compared to standard antibiotics.

Extract	Hexane, Er1	CH ₂ Cl ₂ , Er2	ethyl acetate, Er3	Butanol, Er4	Standard antibiotic
Fungi					Amphotericin B
<i>Aspergillus fumigate</i> (RCMB 02568)	N A	NA	19.2 ±0.72	NA	23.7 ± 0.1
<i>Syncephalastrum racemosum</i> (RCMB 05922)	N A	NA	18.3 ±0.58	NA	19.7 ± 0.2
<i>Geotricum candidum</i> (RCMB 05097)	N A	NA	21.6 ±0.63	NA	28.7 ± 0.2
<i>Candida albicans</i> (RCMB 05036)	N A	NA	20.2 ±1.2	NA	25.4 ± 0.1
Gram positive bacteria					Ampicillin
<i>Streptococcus pneumonia</i> (RCMB 010010)	N A	16.3 ±0.58	18.6 ±0.63	20.3 ±0.58	23.8 ± 0.2
<i>Bacillis subtilis</i> (RCMB 010067)	N A	17.6 ±1.2	21.6 ±1.2	23.4 ±1.2	32.4 ± 0.3
Gram negative bacteria					Gentamicin
<i>Pseudomonas aeruginosa</i> (RCMB 010043)	N A	15.2 ±1.2	16.8 ±1.2	18.2 ±0.72	20.6 ± 0.58
<i>Escherichia coli</i> (RCMB 010052)	N A	13.7 ±0.72	19.2 ±0.58	20.6 ±0.58	19.9 ± 0.3

NA: No activity.

Table 3: Relative viability of cells (%) of *E. rauwolfii* extracts against human tumor cell lines HePG-2, MCF-7 and HCT-116

Concentration	HePG-2	MCF-7	HCT-116
5-FU			
100 µg/ml	8.6	7.9	7.4
50 µg/ml	17.1	14.8	12.1
25 µg/ml	24.0	21.0	19.8
12.5 µg/ml	33.1	34.5	31.4
6.25 µg/ml	56.8	47.3	49.9
3.125 µg/ml	70.6	58.2	60.5
1.56 µg/ml	88.7	76.0	73.6
Hexane extract, Er1			
100 µg/ml	31.7	44.1	34.0
50 µg/ml	42.6	56.3	45.2
25 µg/ml	55.3	67.5	57.6
12.5 µg/ml	68.2	78.6	69.8
6.25 µg/ml	87.4	95.2	93.9
3.125 µg/ml	100	100	100
1.56 µg/ml	100	100	100
Methylene chloride extract, Er2			
100 µg/ml	24.5	33.7	20.8
50 µg/ml	35.4	45.1	27.4
25 µg/ml	46.8	58.6	38.5
12.5 µg/ml	57.2	69.3	52.3
6.25 µg/ml	71.7	90.5	73.6
3.125 µg/ml	92.6	100	91.2
1.56 µg/ml	100	100	100
Ethyl acetate extract, Er3			
100 µg/ml	9.3	17.6	13.4
50 µg/ml	17.2	25.0	20.2
25 µg/ml	24.7	33.5	27.1
12.5 µg/ml	36.4	45.3	38.7
6.25 µg/ml	55.1	70.7	67.9
3.125 µg/ml	73.8	86.1	75.6
1.56 µg/ml	95.6	100	96.5
Butanol extract, Er4			
100 µg/ml	8.0	18.8	8.8
50 µg/ml	15.8	26.3	15.9
25 µg/ml	23.4	35.7	24.7
12.5 µg/ml	31.9	47.2	35.2
6.25 µg/ml	54.6	68.9	58.1
3.125 µg/ml	67.1	89.4	74.0
1.56 µg/ml	85.3	100	92.3

Table 4: Cytotoxicity assessment of *E. rauwolfii* extracts against human tumor cell lines HePG-2, MCF-7 and HCT-116

Extract	In vitro Cytotoxicity IC50 (µg/ml)*		
	HePG-2	MCF-7	HCT-116
5-FU*	7.9±0.25	5.4±0.18	5.3±0.33
Hexane, Er1	36.4±2.81	67.3±3.73	41.2±2.64
Methylene chloride, Er2	22.9±1.34	40.9±3.12	17.6±1.35
Ethyl acetate, Er3	8.6±0.36	14.2±0.97	10.7±1.10
Butanol, Er4	7.1±0.30	15.1±1.06	8.5±0.78

IC50 (µg/ml)*: 1 – 10 (very strong). 11 – 20 (strong). 21 – 50 (moderate). 51 – 100 (weak) and above 100 (non-cytotoxic);
5-FU*= 5-fluorouracil, a standard cytotoxic.

4. ACKNOWLEDGMENTS

I would like to thank Ministry of Science and Technology in Iraq for funding my M.Sc. study and Chemistry Department, Faculty of Science, Mansoura University, for providing some research facilities.

1. REFERENCES

1. Täckholm, V. 1974. Students Flora of Egypt, Cairo University, Cooperative Printing Co. Beirut. 2nd. Ed; pp. 450-451.
2. Feinbrun-Dothane, N. 1978. Flora Palaestina, The Israel Academy of sciences and Humanities. Vol. 3, pp. 74-77.
3. Jafri, S. M. H. and El-Gadi, A. 1979. Flora of Libya, Al Faateh University, Tripoli. Vol. 68, pp. 33-49.
4. Nicholls, P., 2000. Viper's bugloss and related species *Echium* spp. John King & Sons Ltd. www.dweckdata.com/Published_papers/Echium.pdf
5. Schmeller T., El-Shazly A., Wink M., 1979. Allelochemical activities of pyrrolizidine alkaloids: interactions with neuroreceptors and acetylcholine related enzymes. J. Chem. Ecol. 23, 399-416.
6. Stegelmeier B.L., Edgar J.A., Colegate S.M., Gardner D.R., Schoch T.K., Coulombe R.A. and Molyneux R.J. 1999. Pyrrolizidine alkaloid plants, metabolism and toxicity. J. Nat. Toxins 8, 95-116.
7. Boulos L. 2000. Flora of Egypt. Al Hadara Publishing, Cairo, Egypt. Volume 2 pp. 303,302.
8. Boulos L. 2009. Flora of Egypt (Checklist). Revised annotated addition, Al Hadara Publishing, Cairo, Egypt. pp.190.
9. Yen G.C. and Duh P.D. 1994. Scavenging effect of methanolic extracts of peanut hulls on free radical and active oxygen species, J Agric Food Chem, 42: 629-632.
10. Mosmann T. 1983. Immunol. J. Methods 65, 55-63.

11. Denizot F. 1986. Lang. R.; Immunol. J. Methods 22, 271-277.
12. MauceriHJ, HannaNN, BeckettMA, GorskiDH, StabaMJ, StellatoKA, BigelowK, Heimann R, Gately S, Dhanabal M, SoffGA, Sukhatme VP, Kufe DW, Weichselbaum RR Nature 1998. Combined effects of agiostatin and ionizing radiation in antitumour therapy. 394:287-291.
13. Sakineh Abbaszadeh S., Radjabian T., Taghizadeh M., Fazeli F. and Salmaki Y. September 2011. Characterization of fatty acids in different organs of some Iranian *Echium* plants. Vol. 5(19), pp. 4814-4821, 23.
14. Alali F.Q., Tahboub, Y.R., Ibrahim, E.S., Qandil, A., Tawaha, K., Burgess, J.P, Sy, A., Nakanishi, Y., Kroll, D.J., Oberlies, N.H. 2008. Pyrrolizidine alkaloids from *Echium glomeratum* (Boraginaceae). Phytochemistry. 69, 2341–2346.
15. El-Shazly A., Abdel-All M., Tei, A., Wink, M. 1999. Pyrrolizidine alkaloids from *Echium rauwolfii* and *Echium horridum* (Boraginaceae). Z. Naturforsch. 54c, 295–300.

Investigation of Eigen Frequencies and Eigen Modes of Rooms Due To Low Frequency Noise

A.M.Shehap
Professor of Physics
Department of Physics, Faculty
of Science, Cairo University,
Giza,Egypt

Hany A.Shawky
Department of Acoustics, Mass
and force metrology division
National institute for
standards(NIS)
Tersa st.,Giza,Egypt

Tarek M.El-Basheer
Department of Acoustics, Mass
and force metrology division
National institute for
standards(NIS)
Tersa st.,Giza,Egypt

Abstract: There are rapid social, economic and technological changes, and the numbers of industrial noise sources are growing higher which are affecting a large number of individuals in past decades. Low frequency noise (LFN), the frequency of which ranges below 250 Hz, is generated by many machines commonly used in the working environment, such as fans, ventilation systems, heat pumps, diesel engines, blowers, compressors, and so on. Sound pressure levels (SPLs) at low frequencies (20 to 200 Hz) are strongly dependent on measurement position in normal-sized rooms. The variation of SPL can be above 20 dB between different measurement locations. Resonance frequency, called modes are present in every room. For low frequency modes we have to investigate the resonance behavior of room as a whole. This paper demonstrates the use of COMSOL multiphysics to predict the acoustic response of a room such as laboratory in Shopra Elkheima electrical power plant.

Keywords: low frequency noise(LFN), electrical power plant, resonance frequency, eigenmodes, eigenfrequencies.

1. INTRODUCTION

The generation of the standing waves due to LFN is a commonly confronted problem in everyday life. The increment of noise can be caused by standing waves, if some requirements are fulfilled. Usually at these conditions the people complaints about insomnia, migraines, lack of concentration, or other, even more serious, health problems.[1-3]. The sound fields in rooms at low frequencies are complicated because of individual room modes. The SPL measurements become very uncertain because measurement in one position, or even a few positions, cannot be used to describe the experienced sound field in general. Some measurement methods have been specially designed to reduce the uncertainty and to improve the reproducibility at low frequencies, but still it is not clear worldwide which method are the most appropriate for practical use. Some methods focus on the experienced sound field. That is, they suggest measurements only on occupant's positions in the room. The repeatability can be low because different measurement technicians may have different criteria to choose the measurement locations. Other methods perform the measurements close to the corners where the maximum SPL is normally found. The repeatability of those methods is better but it is not clear how the measured values should be compared against the target values.

Uneven distribution of sound leads to uncertainties in noise level measurements in rooms especially at low frequencies. All standardized room acoustic measurement methods, e.g., ISO 10052, ISO 140 series, ISO 354, and ISO 374x series, presume that the acoustic field of the room is diffuse. Ideally, the diffuse sound field presupposes that the sound enters to any point of the room evenly from all directions, that is, the sound intensity vector is zero.

2. ROOM MODES

Room modes, sometimes called standing waves, result from a coincidence where the sound wave, examined in a certain point, returns to the same point after two or more reflections

from the room boundaries and interferes with the original sound wave in the same phase. The sound travels the same path ideally infinite times. As a result of this, the sound pressure level depends strongly on location. Room modes appear at certain frequencies, called room resonance frequencies or eigenfrequencies where the length of the path described above is a multiple of wavelength.

At room modes there will be fixed points in the room where the waves will amplify each other to produce antinodes (sound pressure is high) and other points where complete or partial cancellation occurs to produce a node (sound pressure is zero). These points determine the highest and lowest sound pressures in the room. In spaces with parallel walls, no furniture or fittings, and low sound absorption, repeated reinforcement and cancellation may lead to very strong nodes and antinodes.

The resonance frequencies of a box-shaped room can be calculated according to

$$f_{n_x, n_y, n_z} = \frac{c_0}{2} \left[\left(\frac{n_x}{L_x} \right)^2 + \left(\frac{n_y}{L_y} \right)^2 + \left(\frac{n_z}{L_z} \right)^2 \right]^{0.5} \quad (1)$$

Where c_0 is the speed of sound (m/s); L_x , L_y , L_z are the characteristic dimensions of room (m) and n_x , n_y , n_z are equal to 1,2,3,..... . Eq. (1) does not give information about the spatial variation of SPL at the resonance frequencies or the location of the maximum and minimum sound pressure levels (SPLs). Sophisticated modelling methods which solve the wave equation of sound at every point in the space can be applied. Modes occurring along one dimension of the room are called axial modes. If the room walls are parallel and $L_x > L_y > L_z$, the first axial mode $l_{mn}=100$ occurs along the length of the room. Its node would be in the middle of the room and the antinodes by the walls. According to Eq. (1) the first resonance mode occurs at the frequency whose wavelength is

half the length of the room. The second axial mode would be $l_{mn}=200$ if $L_x > 2L_y$, otherwise $l_{mn}=010$. Modes happening along two dimensions of the room are called tangential modes, i.e. $l_{mn}=110$ or $l_{mn}=201$. Finally, oblique modes occur along the three dimensions, i.e. $l_{mn}=111$ which runs along the grand diagonals from opposite corners. A representation of the axial, tangential and oblique modes is shown in figure (1).

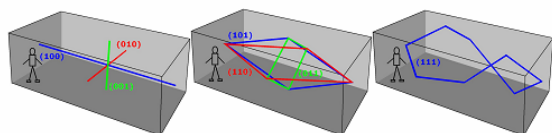


Figure 1: Left) Axial modes (100), (010) and (001). Center) Tangential modes(110), (011) and (101). Right) Oblique mode (111).

Room modes are mostly responsible of spatial SPL variations within rooms. Spatial variations are the largest at low frequencies where the lowest room modes occur. When the sound field is studied one frequency at a time, the strongest SPL differences between different points are expected at the resonance frequencies. When the measurements are performed in frequency bands, e.g. 1/3-octave bands, the variation of SPLs becomes smaller because several room modes belong to the same frequency band and they interfere with each other producing a more diffuse field. Ideally, the diffuse sound field presupposes that the sound enters to any point of the room evenly from all directions, that is, the sound intensity vector is zero. The density of room modes increases with the frequency. Therefore, the higher the frequency is, the smaller is the spatial variation of SPL, and the more diffuse becomes the sound field. The spatial variation of SPL means the difference between the maximum and minimum SPL.

2.1 Axial room modes

Axial modes: Involve two parallel surfaces - opposite parallel walls, or the floor and ceiling. These are the strongest modes. There are always sound pressure maxima (anti-nodes) at the walls.

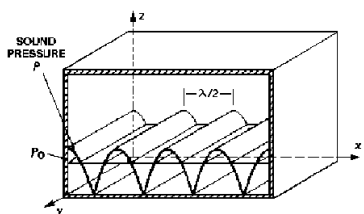


Figure 2: Represent axial mode

2.2 Tangential room modes

Tangential modes : Involve two sets of parallel surfaces - all four walls, or two walls the ceiling and the floor. These are about half as strong (energy) as the axial modes (-3 dB). There are always sound pressure maxima (anti-nodes) at the walls.

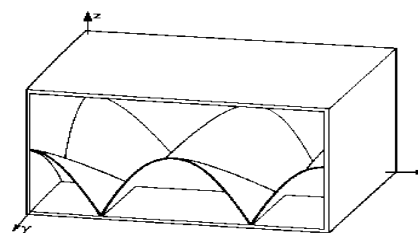


Figure 3: Represent tangential mode

2.3 Oblique room modes

Oblique modes : Involve all six surfaces - four walls, the ceiling and the floor. These are about one quarter as strong (energy) as the axial modes, and half as strong as the tangential modes (-6 dB). Oblique modes are rarely much relevant. There are always sound pressure maxima (anti-nodes) at the walls.

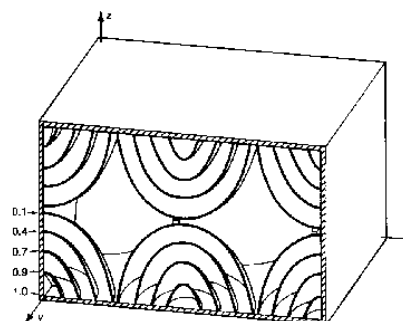


Figure 4: Represent oblique mode

3. MATERIALS AND METHODS

The experimental part of this paper aimed to solid understanding about the distribution of low frequency noise inside laboratory of Shopra Elkheima electrical power plant, what is the location of the maximum and minimum SPLs, what is the variation of SPL, and how different parameters, like dimensions of the room, amount of fittings and absorption, affect the spatial variation of SPL. Experimental methods and modelling methods were applied.

3.1 Measurement of the noise:

Sound level Meter model 2260 (Brüel &Kjaer, Denmark) of accuracy 0.7 dB and resolution 0.1dB is used to measure low frequency noise in different places. By analyzing the spectra of acoustic noise frequencies, the equipment was positioned at a height of 1.2 m above the ground.

3.2 Model analysis

With the help of Comsol multiphysics® software 4.3b.

4. RESULTS AND DISCUSSION

4.1 Sound frequency analysis

Noise analysis was performed at Laboratory near turbine in electric (Shopra Elkheima)[4]. Figure 5 shows the noise spectra measured at laboratory within frequency range of 16-250Hz. It was found that the difference between L_C-L_A for laboratory exceed 15 dB. This difference is an indicator for

the presence of the amount of low frequency noise energy in the noise. From figure 5, we can found that turbine which is near laboratory is the source of low frequency noise. It is clear also that the sound pressure level in 1/3 octave band is 5dB or more between some of neighboring bands, the noise is said to be tonal in this case.

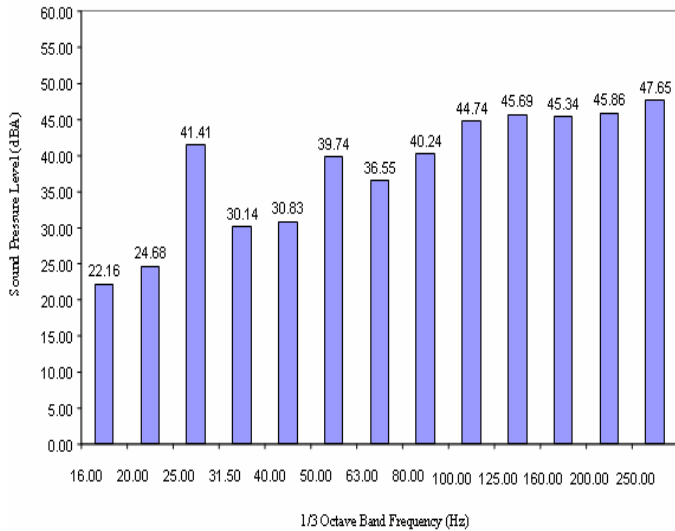


Figure 5: Represents the noise spectra measured at laboratory in Shopra Elkheima electrical power plant.

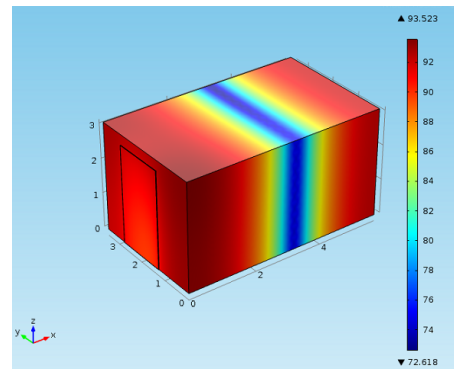
Table 1: Represent laboratory modes.

Freq.(Hz)	Mode index			Type
	n_x	n_y	n_z	
29.31	1	0	0	Axial
48.57	0	1	0	
56.66	0	0	1	
58.62	2	0	0	
87.93	3	0	0	
97.14	0	2	0	
113.33	0	0	2	
117.24	4	0	0	
145.71	0	3	3	
146.55	5	0	0	
170.0	0	0	3	
175.86	6	0	0	
194.28	0	4	0	
205.17	7	0	0	
226.66	0	0	4	
234.48	8	0	0	
242.85	0	5	0	
56.72	1	1	0	Tangential
63.79	1	0	1	
74.63	0	1	1	
76.12	2	1	0	
81.53	2	0	1	
101.46	1	2	0	
112.46	0	2	1	

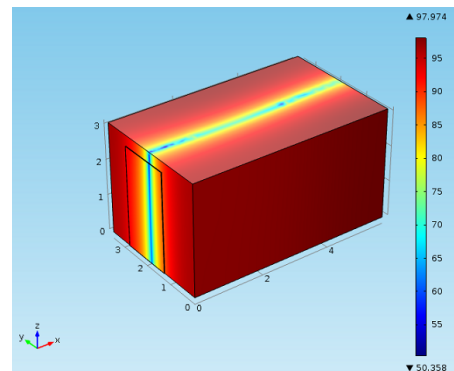
117.06	1	0	2	
123.30	0	1	2	
146.53	1	3	0	
152.25	4	2	0	
172.50	1	0	3	
176.80	0	1	3	
187.02	4	3	0	
195.79	0	2	3	
202.93	2	4	0	
213.25	3	4	0	
223.90	0	3	3	
243.12	3	0	4	
250.19	4	0	4	
80.18	1	1	1	Oblique
94.90	2	1	1	
116.21	1	2	1	
126.73	1	1	2	
136.52	2	1	2	
152.11	1	2	2	
160.36	2	2	2	

4.2 Acoustic behavior

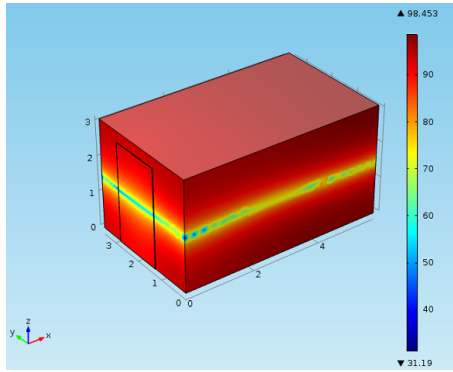
To illustrate the effects, we are going to calculate every eigenfrequencies below 200Hz, together with their corresponding eigenmodes. Table 1 shows both eigenfrequencies and eigenmodes of the laboratory.



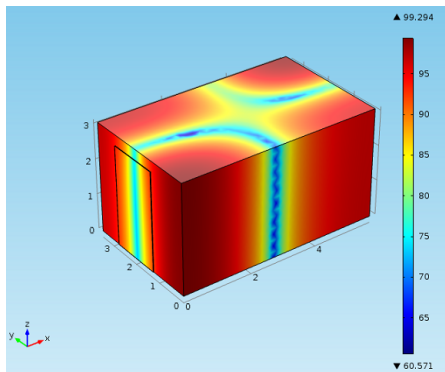
(a) Mode(1,0,0) frequency (28.3)



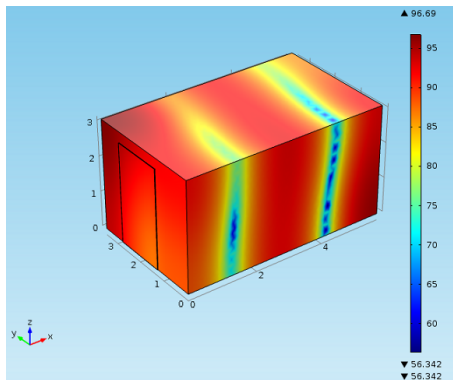
(b) Mode(0,0,1) frequency (43.19)



(c) Mode(0,1,0) frequency (49.14)



(d) Mode(1,1,0) frequency (50.66)



(e) Mode(2,0,0) frequency (53.56)

Figure 6: Shows a few mode shapes a,b,c,d and e.

From figure 6 we can found that if source is at a node, it cannot excite the mode; but if it is at an antinode, it gives maximum excitation of that mode. At a node, microphone reads nothing; at an antinode, it gets maximum reading for that mode. It is clear that eigenmodes differ slightly from the exact solution for an empty room. To eliminate the generation of standing wave is by building rooms with no perpendicular walls or with dimensions which are not multiples of $\lambda/2$ of source characteristic wavelength.

5. CONCLUSION

This work demonstrates the capabilities of COMSOL Multiphysics to solve the complex problem of acoustic performance of rooms. Most rooms have their fundamental resonances in 20-200Hz region.

6. REFERENCES

- [1] Pawlaczyk-Luszczynska M, Dudarewicz A, Szymczak W, Sliwinska-Kowalska M. 2010. Evaluation of annoyance from low frequency noise under laboratory conditions. *J. Noise Health*, 12, 166-81.
- [2] Ziara S.(2011). Effects of low frequency noise in closed space on the human., In: *Proceedings of the Inter-Noise 2011. The 40th International Congress and Exposition on Noise Control Engineering*. Osaka: Publisher INCE/J and ASJ; 2011. p. 8, abstract p. 211.
- [3] Low frequency noise 2001. Technical Research Support for DEFRA. Noise Program.
- [4] A.M.Shehap, Hany A.Shawky and Tarek M.El-Basheer, 2015. A study of the whole body vibration analysis induced by low frequency noise and vibrations in Egyptian power plants. 22nd International Congress on Sound and Vibration, Florence, Italy.12-16 July.

Protocol Enhancements in LEACH

Neha Aggarwal

Electronics & Communication, IIMT Meerut
Meerut, India

Abstract-LEACH is a hierarchical protocol in which most nodes transmit to cluster heads, and the cluster heads aggregate and compress the data and forward it to the base station (sink). In LEACH, a TDMA-based MAC protocol is integrated with clustering and a simple “routing” protocol. The goal of LEACH is to lower the energy consumption required to create and maintain clusters or to use the energy of the nodes in such a manner so as to improve the life time of a wireless sensor network. In this paper we are presenting an overview of the different protocol changes made in LEACH to improve network lifetime, throughput, coverage area of network etc.

Keywords-LEACH, E-LEACH, Enhanced LEACH, EHE-LEACH, Multi-level Leach

1. LEACH: PROTOCOL EXPANATION

LEACH, Low-energy Adaptive Clustering Hierarchy, presented by Wendi B. Heinzelman of MIT, is application specific protocol architecture for Wireless Sensor Network (WSN). It assumes a dense sensor network of homogeneous, energy-constrained nodes, which shall report their data to a sink node. It has become one of the most used bases for developing new architecture protocols or modifying the existing one in WSN.

LEACH [6] is a TDMA-based MAC protocol which is integrated with clustering and a simple routing protocol in wireless sensor network. LEACH partitions the nodes into **clusters** and in each cluster a dedicated node, the **clusterhead**, is responsible for creating and maintaining a TDMA schedule; all the other nodes of a cluster are **member nodes**. To all member nodes, TDMA slots are assigned, which can be used to exchange data between the member and the clusterhead; there is no peer-to-peer communication. Except their time slots, the members can spend their time in sleep state. The clusterhead aggregates the data and transmits it to the sink. Since the sink is often far away, the clusterhead must spend significant energy for this transmission. For a member, it is typically much cheaper to reach the clusterhead than to transmit directly to the sink. The clusterheads role is energy consuming since it is always switched on and is responsible for the long-range transmissions. If a fixed node has this role, it would burn its energy quickly, and after it died, all its members would be “headless” and therefore useless. Therefore, this burden is rotated among the nodes.

Specifically, each node decides independent of other nodes whether it becomes a clusterhead, and therefore there is no signalling traffic related to clusterhead election (although signalling traffic is needed for subsequent association of nodes to some clusterhead). This decision takes into account when the node served as clusterhead the last time, such that a node that has not been a clusterhead for a long time is more likely to elect itself than a node serving just recently. The protocol is round based, that is, all nodes make their decisions whether to become a clusterhead at the same time and the nonclusterhead nodes have to associate to a clusterhead subsequently. The nonclusterheads choose their clusterhead based on received signal strengths. The network partitioning into clusters is time

variable and the protocol assume global time synchronization.

After the clusters have been formed, each clusterhead picks a random CDMA code for its cluster, which it broadcasts and which its member nodes have to use subsequently. This avoids a situation where a border node belonging to clusterhead A distorts transmissions directed to clusterhead B, shown in Figure 1.

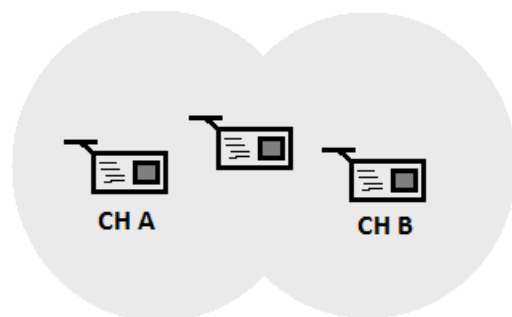


Fig 1

A critical network parameter is the percentage of nodes that are clusterheads. If there are only a few clusterheads, the expected distance between a member node and its clusterhead becomes longer and therefore the member has to spend more energy to reach its clusterhead while maintaining a given BER target. On the other hand, if there are many clusterheads, there will be more energy expensive transmissions from clusterheads to the sink and less aggregation. Therefore, there exists an optimum percentage of clusterheads, which for the scenario investigated in is $\approx 5\%$. If this optimum is chosen, LEACH can achieve a seven to eight times lower overall energy dissipation compared to the case where each node transmits its data directly to the sink, and between four and eight times lower energy than in a scenario where packets are relayed in a multi-hop fashion. In addition, since LEACH distributes the clusterhead role fairly to all nodes, they tend to die at about the same time.

The protocol is organized in **rounds** and each round is subdivided into a setup phase and a steady-state phase, Figure 2. The **setup phase** starts with the self-election of nodes to clusterheads.

In the following **advertisement phase**, the clusterheads inform their neighborhood with an advertisement packet. The clusterheads contend for the medium using a CSMA protocol with no further provision against the hidden-terminal problem.

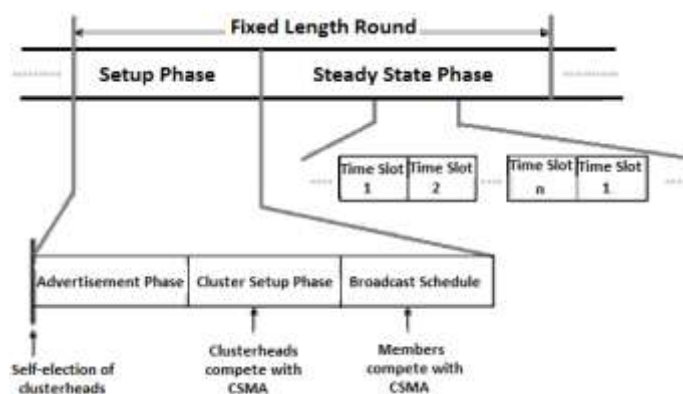


Fig 2

The nonclusterhead nodes pick the advertisement packet with the strongest received signal strength. In the following cluster-setup phase, the members inform their clusterhead (“join”), again using a CSMA protocol. After the cluster setup-phase, the clusterhead knows the number of members and their identifiers. It constructs a TDMA schedule, picks a CDMA code randomly, and broadcasts this information in the broadcast schedule sub phase. After this, the TDMA steady-state phase begins. Because of collisions of advertisement or join packets, the protocol cannot guarantee that each nonclusterhead node belongs to a cluster. However, it can guarantee that nodes belong to at most one cluster as shown in Fig 3.

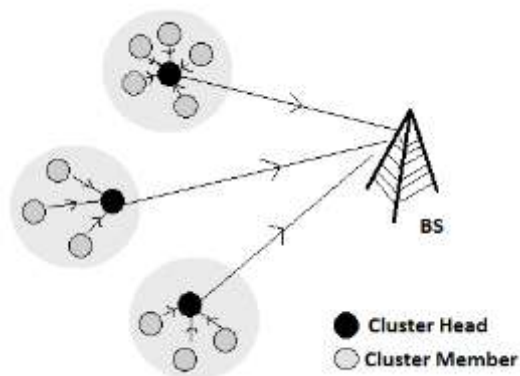


Fig 3

The clusterhead is switched on during the whole round and the member nodes have to be switched on during the setup phase and occasionally in the steady-state phase, according to their position in the cluster’s TDMA schedule.

Nodes that have been cluster heads cannot become cluster heads again for P rounds, where P is the desired percentage of cluster heads. Thereafter, each node has a $1/P$ probability of becoming a cluster head in each round.

In the setup phase, each node decides whether or not to become a cluster head for current round. The selection depends on decision made by the node by choosing a random

number between 0 and 1. If the number is less than the threshold $T(n)$, the node becomes a clusterhead for the current round. The threshold is set as:

$$T(n) = \begin{cases} \frac{P}{1 - p(r \cdot \text{mod}(\frac{1}{p}))} & , \text{if } n \in G; \\ 0 & , \text{else} \end{cases}$$

Where p is the probability of the node being selected as a cluster-head node, r is the number of rounds passed, and G is the set of nodes that have not been cluster-heads in the last $1/p$ rounds, mod denotes modulo operator. Nodes that are cluster heads in round r shall not be selected in the next $1/p$ rounds. The random selection algorithm for LEACH easily leads to the imbalance of the stored energy of sensor nodes, thereby; the consumption of system energy is increased.

2. Enhanced LEACH

In LEACH protocol, time is divided into many rounds, in each round, all the nodes contend to be cluster head according to a predefined criterion. Enhanced LEACH [1] protocol was proposed to set the time length of each round, to prolong the lifetime of the network and increase throughput, which is denoted as the amount of data packs sent to the sink node. LEACH protocol lets the data transmission phase last for a fixed period of time, then enter into a new round of cluster head election. The time length of round has obviously influence on the performance of LEACH protocol. In order to decrease the overhead of set-up phase, we hope to increase the time length of round, which increases the time for data transmission. However, prolonging the time length of round also increases the energy consumption of cluster head, which will causes some nodes die early and in turn shortens the lifetime of wireless sensor networks. So, regarding to configuration of time length of round, there is a trade-off between lifetime and throughput.

If the time of set-up phase is α , and the steady data transmission time is t , then the time length of every round is $t_r = \alpha + t$. Let the time when the first sensor node dies as the lifetime of the network, which is denoted as t_{find} .

$t_{\text{find}} = n(\alpha + t)$, Where n is the number of rounds after which the first sensor node dies.



Fig 4

According to LEACH protocol, there are m frames in the time t , so frame $t = m \cdot T$, here frame T is the time length of each frame. As the time length of a round increase with m , increasing m will increase the energy consumption of cluster head in a round, which makes the energy consumption in the network unbalanced. Therefore, some nodes will die early and

in turn shortens the lifetime of wireless sensor networks. So as per Fig 5 and Fig 6, $m=5$ is good for trade-off between lifetime and throughput.

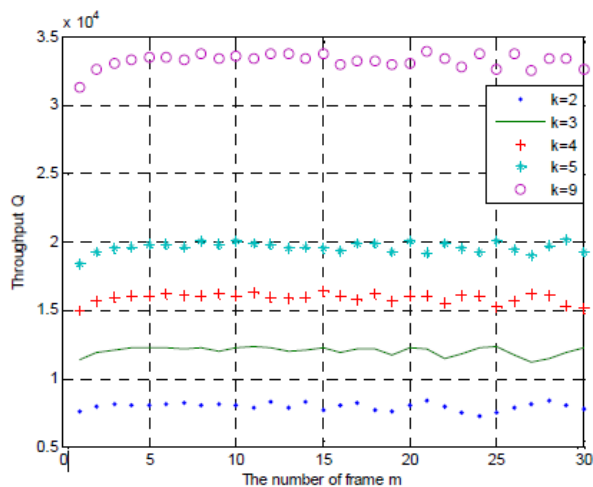


Fig 5

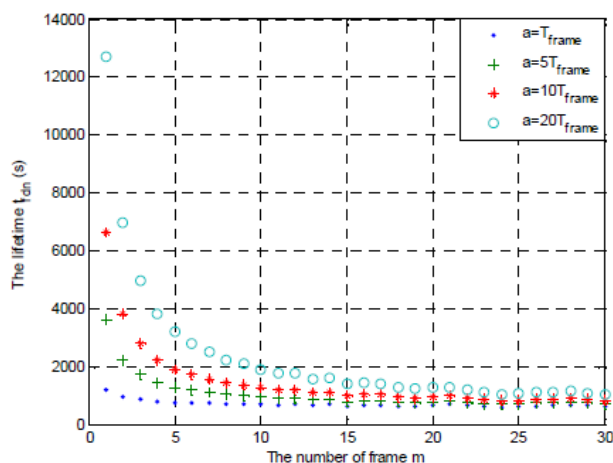


Fig 6

3. E-LEACH

In the E-LEACH [2] algorithm, the original way of the selection of the cluster heads is random and the round time for the selection is fixed. The nodes with low remnant energy have the same priority to be a cluster head as the node with high remnant energy. Therefore, those nodes with less remaining energy may be chosen as the cluster heads which will result that these nodes may die first. In the E-LEACH algorithm, we consider the residual power of the sensor nodes in order to balance network loads and changes the round time depending on the optimal cluster size.

The cluster heads communicate with the base station in single-hop mode which makes LEACH inefficient to be used in large-scale wireless sensor networks for the limit effective communication range of the sensor nodes. The E-LEACH adopts the same round concept with the original LEACH. In hierarchical routing protocols, the number of cluster-heads is a key factor that affects the performance of routing protocols. If the number of cluster-heads is less, each cluster-head needs to cover larger region, this will lead the problem that some

cluster-members get far from their cluster-heads and consume much more energy. As the communication between cluster heads and the base station needs much more energy than common nodes, the excessive number of cluster-heads will increase the energy consumption of the whole network and shorten the network lifetime. Therefore, it is necessary to select optimal clusterhead number to make the energy consumption minimum. In the E-LEACH we use the minimum spanning tree between clusterheads, choose the cluster head which has largest residual energy as the root node. Fig 7 depicts the architecture of ELEACH.

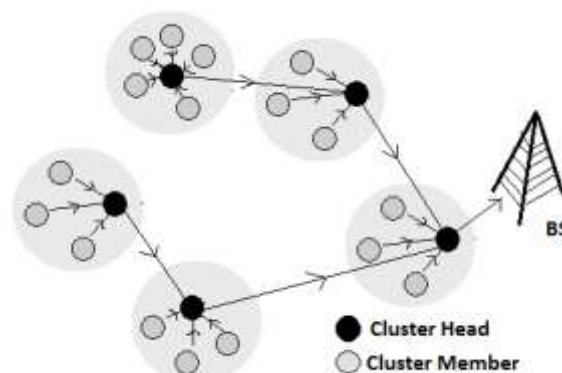


Fig 7

Fig.8 is the comparison of FND and HND between LEACH and E-LEACH. If the system lifetime is defined as the number of rounds for which the first node dies, E-LEACH algorithm can reach 1529 rounds, whereas LEACH only reaches 1029 rounds. The system lifetime is improved by 49% of E-LEACH algorithm than LEACH.

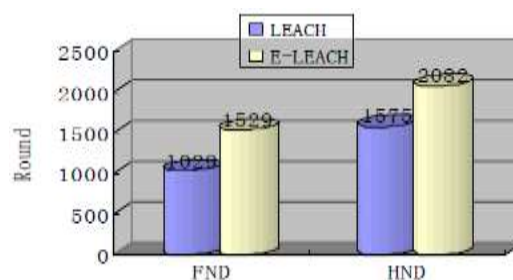


Fig 8

The simulation results show that our proposed protocol increases network lifetime at least by 40% when compared with the LEACH algorithm.

4. EHE-LEACH

The major problem of the sensor node is the limited energy. Therefore, energy efficiency in the design of routing protocols for sensor networks is of principal requirement. EHE-LEACH [3] (Enhanced HETerogeneous - Low Energy Adaptive Cluster based Hierarchical protocol) is based on the fixed distance threshold, which is used to bifurcate the coverage area, used two separate mechanism direct diffusion and clustering. From a survey it is observed that minimum two hop data transmission is required for the cluster based communication, from source to BS even though the distance between source

and BS is very small. This consumes extra execution time for the completion of a round.

From Fig. 9 it is clear that $d_3 > d_2 > d_1$. For LEACH protocol single hop communication is not, minimum two hops communication is required.

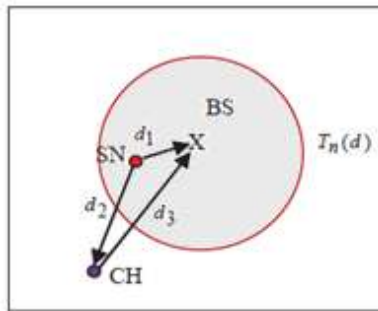


Fig 9

In the proposed model two parameters are considered: firstly- minimize the execution time of a round to some extent by using direct diffusion. Secondly- maximizes the lifetime and stability of the network by using the combination of two techniques simultaneously direct diffusion and clustering. The half nodes alive (HNA) & last node alive (LNA) are the key parameters used for the measurement of lifetime and the stability of the system. SNs near to the BS communicate directly and those which are far away from the BS use cluster based communication. To evaluate the performance of the proposed scheme two key parameters known as: Half Nodes Alive (HNA) and Last Node Alive (LNA) are selected. By selecting the distance based threshold with the ratio of 1:9 between direct communication and cluster based communication it has been observed that EHE-LEACH has better network lifetime with respect to various parameters in comparison to the other well-known proposals such as LEACH.

5. Multi-Level LEACH

Although LEACH protocol conserves energy in the nodes and prolongs the lifetime of the WSN application, it still has the following problems:

- Randomized rotation of the CH without considering the residual energy in the nodes.
- As the network size increases the CH's which are far away from the BS drain their energy sooner.

If the deployment area is less, the LEACH protocol works well. Since the LEACH protocol cannot be used over large areas, a Hierarchical routing protocol based on the LEACH.

In Hierarchical routing protocol [4] the CHs are divided into various levels so that each

CH at a level i transmits the data to its higher level, $(i + 1)$ level CH, instead of transmitting the data to the BS directly. Two-level LEACH (TL-LEACH), Three-level LEACH (3L-LEACH), Four-level LEACH (4L-LEACH) can be implemented to install multi-level LEACH.

5.1 TL-LEACH

In this, we have a two-level structure consisting of leaf nodes, level-1 CH's, level-2 CH's. One of the level-1 CH's is chosen as level-2 CH as shown in figure 3. After collecting the data, a level-1 CH forwards the same to its level-2 CH. This level-2 CH aggregates the data received from its level-1 CH's and the same aggregated data is forwarded to the BS resulting in

energy savings. The operation TL-LEACH can be divided into the following 3 phases, namely:

- Selection of level-1 and level-2 CH's
- Set up phase
- Steady state phase

1) Selection of level-1 and level-2 CH's:

In this the level-1 CH is elected as given in the LEACH protocol. After the election of level-1 CHs, the level-2 CH election is initiated. Among level-1 CHs, the CH with maximum residual energy and proximate to the BS is elected as the level-2 CH as shown figure 3. In addition to its current role as level-1 CH, the node acts as level-2 CH as well.

2) Set-up Phase:

After the election of level-1 CHs, each CH broadcasts an advertisement message to all its leaf nodes. Each leaf node based on received signal strength from all the CHs, decides which CH to join. Then each leaf node transmits an acknowledgement message to its chosen CH along with its node ID. Each level-1 CH records the node IDs of its member nodes. The set up phase for level-2 CH is also similar. In this case, level-1 CHs are treated as the leaf nodes. Each level-1 CHs sends a message containing the number of its member and its own node ID to the elected level-2 CH. Thus, a level-2 CH has information regarding its level-1 CHs and their associated leaf nodes. So based on this information a level-2 CH creates a TDMA schedule to its members and broadcasts a message.

3) Steady state phase:

In the steady state phase transmission of the data takes place. Each leaf node sends the sensed data to its respective CH within its allocated time slot. Until their allocated time slot the leaf nodes can turn off their radio so that energy can be saved. All the leaf nodes transmit their data to its respective level-1 CH. And the level-1 CHs aggregate all the sensed data. The aggregated data received by the level-1 CH is forwarded to their level-2 CH based on its allocated time slot. Thus the data collected by the level-2 CH is sent to the BS. Thus the data from a leaf node to the BS is transmitted using level-1 CH and then level-2 CH. Considerable energy in the WSN application can be saved with this type of hierarchical routing.

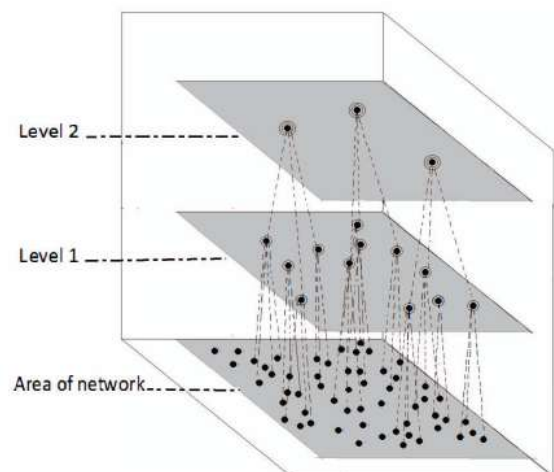


Fig 10

This work presents a multi-level hierarchical routing protocol, which is based on the LEACH protocol. This protocol improves both the energy efficiency and the lifetime of the network. Two-level LEACH (TL-LEACH), Three-level

LEACH (3L-LEACH) and Four-level LEACH (4L-LEACH) have been presented. Analysis (done using NS3) shows that the hierarchical routing protocols, TL-LEACH, 3L-LEACH and 4L-LEACH, are better than the LEACH protocol.

It can be concluded that the multi-level Hierarchical routing protocol is more energy efficient when compared to the LEACH. The lifetime of the network also gets extended. As the deployment area of WSN increases, the 3L-LEACH and 4L-LEACH perform well when compared to the 2L-LEACH.

6. Op-LEACH

LEACH uses a TDMA based MAC protocol, in order to maintain balanced energy consumption. The TDMA schedule maintained by Cluster Head evenly distributes the slots to all of the sensor nodes in its cluster. A number of these TDMA slots are wasted when the nodes have random data distribution. A modification to existing LEACH protocol is needed in order to use the slots corresponding to nodes that do not have data to send at its scheduled slot.

Op-LEACH [5] improves the performance of LEACH algorithm in terms of energy and time delay in real time networks. Every sensor node does not have data all the time. The data is available in random fashion. The sensors may be event driven, so data may be available only when they sense the event. The proposed method is utilizing the slots belonging to the node having no data to send. This method turns free slots into useful slots without making any changes in the TDMA schedule. This will reduce the waiting time for sensor nodes because now sensor nodes can get more than one slot per frame. It will reduce the data transmission delay and increase throughput of the network. The real time sensors are mostly event driven. So until the event occurs, the nodes will not have the data to process or to send (to the cluster head). So the corresponding slots become idle. The proposed algorithm utilizes these idle slots for some other node's data transmission. At the end of setup phase every non cluster head member knows about transmission schedule. Every node waits for its turn to transmit data and if a node does not have any data to transmit, the slot is allotted to the next sensor in TDMA schedule. This algorithm makes the free slots available to sensor nodes with higher traffic without additional overhead Op-LEACH shows effective performance difference when the data sensed by network nodes is uneven.

7. CONCLUSION

With the protocols discussed so far, it is clear that LEACH would not be able to cover large geographical areas of some square miles or more, because a clusterhead two miles away from the sink likely does not have enough energy to reach the sink at all. If clusterheads use other clusterheads for forwarding, this limitation can be mitigated. Even the slots are wasted in uneven traffic conditions which can be allotted to other nodes for forwarding. Energy efficiency is a key design issue in WSN and must be enhanced in order to improve network life time. Many such modifications can be made in LEACH to increase lifetime and throughput.

8. REFERENCES

- [1] "Enhancing the Performance of LEACH Protocol in Wireless Sensor Network" IEEE INFOCOM 2011 Workshop on M2MCN-2011.
- [2] "Improvement of LEACH protocol for WSN" 2012 9th International Conference on Fuzzy Systems and Knowledge Discovery (FSKD 2012).
- [3] "EHE-LEACH: Enhanced heterogeneous LEACH protocol for lifetime enhancement of wireless SNs", 2013 International Conference on Advances in Computing, Communications and Informatics (ICACCI).
- [4] Multi-level LEACH Protocol model using NS-3, 2014 IEEE International Advance Computing Conference (IACC).
- [5] Op-LEACH: An Optimized LEACH Method for busty traffic in WSNs, 2014 Fourth International Conference on Advanced Computing & Communication Technologies.
- [6] Holger Karl and Andreas Willig "PROTOCOLS AND ARCHITECTURES FOR WIRELESS SENSOR NETWORKS", John Wiley & Sons.

Android and iOS Hybrid Applications for Surabaya Public Transportation Route

Djoni Haryadi Setiabudi
Informatics Department
Petra Christian University
Surabaya, Indonesia

Lady Joanne Tjahyana
Communication Science
Petra Christian University
Surabaya, Indonesia

Abstract: This study is conducted to address the lack of route information of public transportation in Surabaya by creating an online guide that can be accessed by passengers to get complete information on maps and travel routes for public transportation. This guide is made interactive, simple, accessible and appropriate for transport adapted to the conditions in the city of Surabaya. This research will develop an Android and iOS applications that can be used on smartphones and tablets using Android and iOS operating systems. Maps and routes are obtained from the Department of Transportation of Surabaya. A survey was done by distributing questionnaires to determine the passengers' need for public transportation. Maps and route are developed using OpenStreetMap, Ajax, Javascript, XML, OpenLayer, PostgreSQL, and PostGIS. The hybrid application is compiled using PhoneGap. Passengers simply point to the destination of their journey, such as the name of the street or landmarks and public places. The system will automatically choose the alternative lyn of bemo they should choose, including the routes to reach the destination. The information includes the connecting line of a public minibus (called *bemo* in Indonesian) if the route needs to be connected by more than one bemo line. The information also includes the fare to be paid. From the test results, both the Android and iOS applications can adapt to a wide range of smartphones with a variety of screen sizes, from 3.5 inch to 5 inch smartphones and 7 inch tablets

Keywords: routes, maps, public transportation, bemo, OpenStreetMaps, android, iOS

1. INTRODUCTION

Currently one of the mass public transportations in the city of Surabaya is the type of small and medium 1000cc minibus commonly called bemo with a maximum carrying capacity of 10 persons [4]. Watkins et al [2] in the studies of open source development of mobile transit traveller OneBusAway information system for King County Metro (KCM) in Seattle suggest that the provision of good information system for public transport passengers will increase passengers' satisfaction and increase the interest of public transport. It would be useful to encourage people to switch from the use of private transportation to the public transportation.

Furthermore, based on the observation of the initial research, there are some Android applications of TransJakarta Busway public transportation in Jakarta. Among them is Komutita that has the highest rating 4.6 out of 1,263 voters and has been downloaded more than 50,000 times in the Google Play Store

However, all the applications that have been created can only be running on one operating system. For instance, the application that can be used on Android cannot be used in iOS, Blackberry and Windows Mobile. Conversely the one that runs on Blackberry cannot be used in other operating systems.

As a result, not all smartphone users can take advantage of software applications that have been created. This is because all of the applications initially were developed using native application and not with the hybrid application [3]. As a result, if an application is already developed as an Android native application, in order to make it available for iOS native application the developer must re-develop the application from the beginning due to different programming languages that are used to develop native applications for different operating systems. If initially the applications were developed

using a hybrid technology to produce cross-platform application, for example for Android, when it would be developed for iOS, only very minor and simple changes needed to be done. The idea of implementing hybrid application could be seen in the diagram of Figure 1.

The head of IDC Operations of Indonesia, Sudev Bangah argued that many smartphones with varying price would be affordable for smartphone users who were on the middle segment market [4].

Based on the fact that market share is issued by IDC Indonesia, to increase the satisfaction of bemo passengers in Surabaya, this research will develop applications that can be used by smartphones of Android and iOS operating systems for trip planning using bemo in Surabaya using Open Street Maps. Those applications will help the passengers plan their trips based on routes, timetables, and costs.

As shown in Figure 1 the time can be shortened and costs can be saved because after developing a web-based application in the form of responsive website, it becomes a native application using PhoneGap that can then be distributed through the application store for each mobile operating system.

The applications will provide information about route guide and timetable of public transportation in Surabaya. The information will be equipped with a search feature and a trip planning using public transportation simply by typing the place of origin and destination specified by the passengers. Both the place of origin and destination can either be a street name or a landmark name and public place such as bemo stations, parks, rivers, shops, schools, and others.

The planning features will use a multimodal transport network that takes into account some factors such as multimodal

routes, timetables, and costs to provide recommendations for the optimized route. This feature will guide the passengers to the nearest public transportation station, by giving the order of public transportation they should take, to arrive at the nearest public transportation to the destination. This feature will also be equipped with an estimation of the fare for the service.



Figure 1. Block Diagram of The System

2. HYBRID APPLICATIONS

There are several types of mobile application, which are Native App, Web App and Cross Platform Mobile App or Hybrid App. According to Stark [5], Native application is application installed on the phone, such as Android and iOS-based Smartphones. Native applications have access to the Smartphone hardware features such as camera, speaker, etc. Developers have to use different kinds of programming language to develop native applications for different platforms. To develop Android native applications, Java programming language is needed. Objective – C is used to develop iOS native applications. Native applications are available on the official application markets such as Google PlayStore for Android and iTunes App Store for iOS.

On the contrary to Native application, Web applications are not installed on the phone and they are not available on the official application markets such as Google PlayStore and iTunes App Store. However, they are easily accessed with the Smartphone's web browsers and that means developers are only required to use HTML, CSS, and JavaScript to build Web applications. The downside for Web applications is that it cannot access certain hardware features on the smartphone [5].

Hybrid application or Cross Platform mobile application is considered to be the right solution for developer to build iOS and Android applications without mastering many programming languages and downloading any SDKs (software development kits) for each platform, but it can put the application on Google PlayStore and iTunes App Store [6]. To build a hybrid application or a cross platform mobile application both for iOS and Android, developers only need to use HTML, CSS and JavaScript to develop a web application. Next, with PhoneGap technology, the web application will be packaged into a native application for iOS, Android and other mobile platforms [5].

A graph that highlights the differences in native, hybrid and mobile web applications can be seen in Figure 2.

Native applications are built for a specific platform with the platform SDK, tools and languages, typically provided by the

platform vendor (e.g. xCode /Objective-C for iOS, Java for Android, Visual Studio/C# for Windows Phone).

Mobile Web applications are server-side applications, built with any server-side technology (PHP, Node.js, ASP.NET) that render HTML that has been styled so that it renders well on a device form factor.

Hybrid applications, like native applications, run on the device, and are written with web technologies (HTML5, CSS and JavaScript). Hybrid applications run inside a native container, and leverage the device's browser engine to render the HTML and process the JavaScript locally. A web-to-native abstraction layer enables access to device capabilities that are not accessible in Mobile Web applications, such as the camera and local storage.

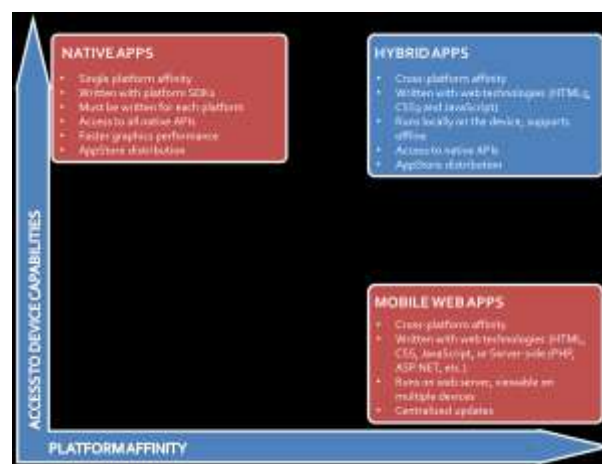


Figure 2. Three Types of Applications

3. RESEARCH METHODOLOGY

3.1 Fishbone Diagram

The method used in this research can be seen in Figure 3. The first step includes a survey of the timetables of public transportation, the fare of travel, and the location of public places.

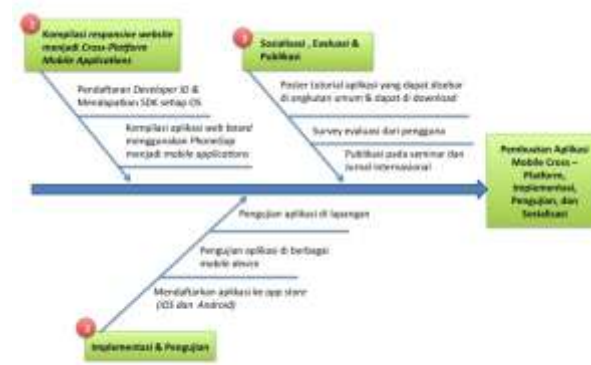


Figure 3. Fishbone Diagram of Research Methodology

The first step is to compile the responsive website that has been made to be cross-platform mobile application using Phonegap. At this stage the process will begin with registration of Developer ID in the application store for each operating system, until a developer SDK for each platform is

secured. After this, the compilation of web-based applications with the SDK of each platform using phonegap, resulting in cross-platform mobile applications needs to be done. The outcomes are cross-platform mobile applications that can be used for each operating system (iOS and Android).

The second step will be the implementation and testing of applications with the following stages: Registering and uploading applications on each application store for each operating system (iOS and Android), namely AppStore for iOS and Google Play Store for Android. Testing the applications on a variety of mobile devices for each operating system with a different screen resolution size. Testing the use of applications in the real case and doing the journey planner on public transportation in Surabaya with some case studies of travel route need to be done.

The last stage or the third step will be to disseminate and evaluate the applications with the following stages: Create tutorial posters to use the application that will be shown at the terminal and all public transportation. Upload the tutorial posters at the Department of Transportation website and official Facebook page of the Department of Transportation. Finally evaluate the application by providing a place for criticisms and suggestions the make the application better.

3.2 System Design

The design of the client system is shown in the flowchart in Figure 4. Firstly, the users must choose what they want to do, whether they want to look all routes or directly get to the direction. If they choose to see all routes, all lists of bemo lines nearby their current position will be shown.

Furthermore, they have to pick one from the list to see the route on the map. However, if they want to get directly to their destination, they must choose one point of interest available in the server database. Then, they have to choose how the application detects their current location using GPS or manually clicking on the map. Nevertheless, the method to detect the user's location still depends on whether the GPS is available on their device or not. If the application can detect the current location of the user, then it will show the routes to go to their destination using the closest line available near their current location.

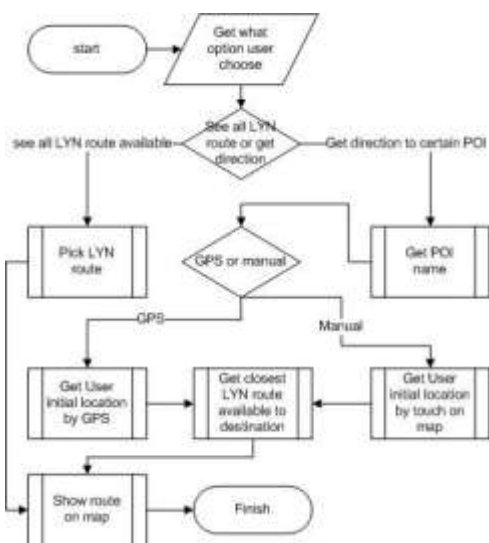


Figure 4. Flowchart of the Client System

4. EXPERIMENTAL RESULTS

The testing of the applications was done using two devices, namely 3.5 inch smartphone and 7 inch tablet. The first time the applications is initialized, it will display the screen like in Figure 5. There are two options to choose, namely 'Search bemo routes to destination' and 'See all existing routes of bemo'.

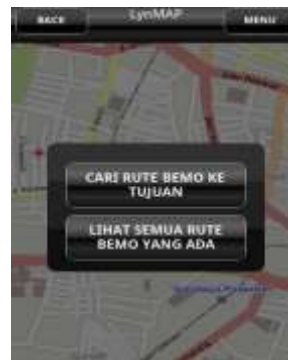


Figure 5. Two Options to Choose



Figure 6. Alternatives of Bemo Routes

If the user selects the option 'See all the existing routes of bemo', then the screen shows as in Figure 6. If the user types a particular letter or word and presses 'ok' then it will display a maximum of 5 lines containing these words or letters typed by the user. If the user presses one of the available buttons from the options, then the application will bring up a page with a map of the selected line like in Figure 7.

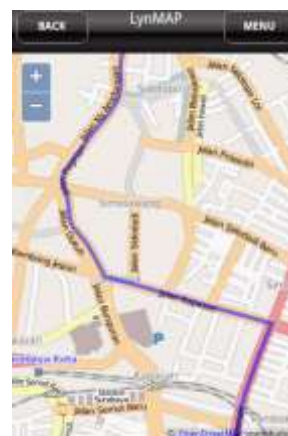


Figure 7. Map route of one Line of Bemo



Figure 8. 5 Point of Interest

If in Figure-5 the user selects the option 'See all the existing routes of the bemo,' the screen will display options as shown in Figure 8. If the user types a particular word (i.e. MALL) and presses 'ok' button, then it will display a maximum of 5 points of interest containing the word typed by the user. Once the user selects one of the existing points of interest, then it will be displayed like in Figure 9.

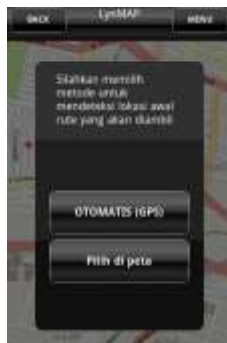


Figure 9. Options Automatically or Manual

Here the user is prompted to choose whether he wants to select the starting location by GPS or to select the starting location on the map using the touchscreen. Once the initial location has been determined, it will show the route to be passed and the estimated fare to be paid as in Figure-10.

In Figure-10 shows that the user originally is on Nyamplungan Street and s/he wants to travel to Ambengan Street. The first time the user is suggested to go by Line A bemo. On the way s/he should get off from the Line A bemo on Tambaksari Street and walk to Kapasari Street to get on Line B bemo. Next s/he has to get off Line B on Tambaksari Street and walk to the destination on Ambengan Street.

When the user wants to see the resulting route s/he can press on the 'view map' button, then options will appear on the display as in Figure 11 on smartphone and Figure 12 on tablet.



Figure 10 Information of Routes

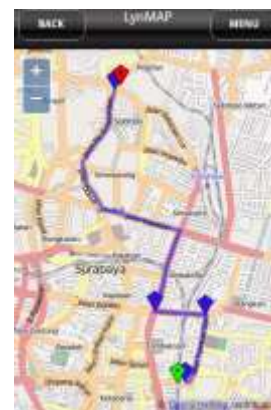


Figure 11 The Routes Generated on The Map (On smartphone)



Figure 12 The Routes Generated on The Map (On tablet)

5. ACKNOWLEDGMENTS

This research can be conducted and accomplished by the grants from the Directorate General of Higher Education Indonesia (DIKTI) using the scheme of "Penelitian Hibah Bersaing 2015" (or 2015 Competitive Research Grant). We would like to thank The Centre of Research of Petra Christian University for their assistance to manage the grants.

6. CONCLUSIONS

Based on the experimental result, it proves that the website of this research can be used to give the information of routes, maps, varying types of bemo lines using any size of

smartphones and tablets without any difficulties. The display can always be adjusted to the screen size of the browser. In searching for the routes, there is a possibility that it does not show the nearest point because to search for the route to the POI, the reference used is the central point of the nearest route that has the bemo line to the POI. However, the result is accurate enough. This is intentionally made this way to make sure that the server does not undergo an overload at receiving many route requests. This method can be faster at least twice compared to making a calculation to all points. If the user is outside 500 meter distance, the application will search for a point of bemo location up to 1.5 kilometers from the user's location. This happens because from the survey results the users feel that 500 meter walk is a comfortable distance to take. However, when the point cannot be located, it will be expanded into 1.5 kilometers presuming that the user can take another transportation or take a walk.

7. REFERENCES

- [1] Angkutan Massal 'Sekarat' .<http://www.surabayapost.co.id/?mnu=berita&act=view&id=0b8729fc9c2f434ea5ffb8252a78680c&jenis=b706835de79a2b4e80506f582af3676a>. April 2013
- [2] K. Watkins, B. Ferris, A. Boring, S. Rutherford, and D. Layton. 2011. Where is My Bus? Impact of mobile real-time information on the perceived and actual wait time of transit riders. In *Transportation Research Part A* 45. 839-848.
- [3] M.Kor, & E.Oksma Native, HTML5, or Hybrid: Understanding Your Mobile Application Development Options. http://wiki.developerforce.com/page/Native,_HTML5,_or_Hybrid:_Understanding_Your_Mobile_Application_Development_Options. April 2013
- [4] M. Grazella. Android to remain champ, Windows to pick up steam in 2013. <http://www.thejakartapost.com/news/2013/01/05/android-remain-champ-windows-pick-steam-2013.html>. April 2013
- [5] Stark, Jonathan. 2010. Building iPhone Apps with HTML, CSS, and JavaScript. USA : O'Reilly Media, Inc.
- [6] Charland, A., & Leroux, B. 2011. Mobile application development: web vs. native. *Communications of the ACM*, 54(5), 49-53.

EEDTCA: Energy Efficient, Reduced Delay and Minimum Distributed Topology Control Algorithm for Mobile Ad Hoc Network

Jayanthi Vagini K
Shiro Software Solutions
Nagercoil, T.N., India

Hemalatha M
Hindustan College of Arts and
Science, Coimbatore
T.N., India

Dinesh R
Shiro Software Solutions
Nagercoil, T.N., India

Abstract: Processing packets across Mobile Ad hoc Network, Topology control minimize interference among node in a network, increase the network capacity and extend lifetime of the network. Emerging research in mobile ad hoc networks (MANETs) says, there is a growing requirement of quality of service (QoS) in terms of delay. In order to resolve the delay problem, it is essential to consider topology control in delay constrained environment with energy efficient. In this paper, we discuss reduced delay and minimum distributed topology control algorithm for mobile ad hoc networks. In this proposed system, we study on the delay-constrained topology control problem, and take into account delay and energy efficiency. Simulation results are presented demonstrating the effectiveness of this new technique as compared to other approaches to topology control.

Keywords: delay; energy efficient; MANETs networks; topology control algorithm; interference.

1. INTRODUCTION

An ad hoc wireless network is a special type of wireless networks that does not have a wired infrastructure to support communication among the wireless nodes. Each node acts as a router, as well as a communication end-point. There are many modern network applications that require QoS provisions in ad hoc networks, such as transmission of multimedia data, real-time collaborative work, and interactive distributed applications.

In order to provide the QoS requirement problem in terms of delay, some researchers found the delay incurred in a forwarding node or a routing path. [2] Delay depends on the speed of propagation and the number of hops a packet must travel to reach its destination that is one portion of the path between source and destination. Then, Xie et al. [3] said that in many cases the queuing delay takes a significant portion of the total delay over a hop. A path, which contains many packets in queue of the nodes and with short transmission delay on links, could have a larger delay than the one, which has less packets in the queue at nodes but longer transmission delay. And the larger the number of the intermediate nodes between the source and destination pair is, the larger the potential delay is. However, in wireless ad hoc networks, the impact of channel contention from neighbors must also be considered. Because of the limited channel source, access delay and collision are generated at nodes. If one of the nodes on a path can not acquire channel in a long period for contention, it may lead to massive packet drops and higher packet dropping rate. Processing delay and propagation delay which change in microseconds are much shorter than transmission delay, contention delay and queuing delay which change in millisecond. Therefore, the end-to-end (E2E) delay should consider: transmission delay over intermediate links, contention delay caused by nodes' contention for the shared channel and queuing delay induced at each intermediate node due to queuing policy or severe channel conditions.

Topology control is to dynamically change the nodes transmission range in order to maintain connectivity of the communication graph, while reducing energy consumption and/or interference that are strictly related to the nodes

transmitting range. A good topology not only can provide a better service for routing layer, but also can save energy, increase network capacity and satisfy the QoS requirements. The previous topology control algorithms [4]–[7] mainly focused on the interference constraint. And how to employ topology control to reduce delay is not fully researched by those works. An alternative way to reduce the E2E delay is to increase the transmission power of a certain node in a path, so that the transmission range of the node is increased and thus the hops between the source and destination are reduced. Transmission delay may be decreased due to the reduction in hops; and the sum of the queuing delay along a path is also decreased because the number of the intermediate nodes is decreased. Thus, increasing the transmission power may reduce the E2E delay. However, it may cause more interference to other nearby active receiving nodes, excessive contention to nearby potential sending nodes, which may incur more retransmissions. And retransmission means the increase of E2E delay. Therefore, reducing delay and minimizing interference are two conflicting goals, and it is necessary to jointly consider a tradeoff between them. Thus, the problem of interference based topology control with delay-constraint is studied.

2. RELATED WORK

During developing real-time service like video, audio and voice over IP (VOIP), it is essential to provide efficient quality of service in MANET. In order to provide QoS to MANET, it should follow the standards of measure include bandwidth, hop count, delay, path reliability, energy consumption and service range. To achieve the above vision, it is significant to consider QoS routing in the QoS architecture. Delay requirement is one of the particularly useful QoS requirements for mobile ad hoc networks. Many QoS routing protocols which consider the end-to-end delay as a QoS measure have been proposed. Draves et al [2] defined the delay as the transmission delay of the packet. But it did not contain the queuing delay. If there are massive packets in the queue waiting for transmission since a node cannot transmit multiple packets simultaneously, the queuing delay

may take a significant portion of the total delay. The delay in [7] contained the queuing delay and the transmission delay. But it did not explicitly consider the effects of channel contention. The contention of the channel can cause access delay and collision at Medium Access Control (MAC) layer.

2.1 Topology Control

2.1.1 Taxonomy

There are several different approaches to topology control and it is possible to organize them into a coherent taxonomy. The first distinction is between approaches that control transmitter power and those that impose a hierarchy in the network. Hierarchical approaches change the logical structure of the network in terms of node adjacencies and may be broken down into approaches that use clustering and those that use dominating sets.

The power control approaches act on the transmission power of nodes using several different techniques. The first distinction to make of power control approaches is between homogeneous and non-homogeneous approaches. Homogeneous topology control is the easier of the two in which nodes are assumed to use the same transmitting power and the problem of topology control becomes in essence one of finding the value of the transmitter range that satisfies a certain network wide property.

In non-homogenous topology control nodes are allowed to select different individual transmitting powers up to a certain maximum that they can support which means that they will have different transmitting ranges. This form of topology control can be split into three different categories according to the type of information that is used to generate the topology. These three categories are location based, direction based, and neighbor based.

In location-based approaches exact node locations are known and are either used by a centralized authority to calculate a set of transmitting range assignments which optimize a certain measure or are exchanged between nodes to create an approximately optimal topology in a distributed fashion. In direction-based approaches, nodes are assumed to not know their positions but can estimate the relative direction to each of their neighbors. Finally, in neighbor-based approaches the only knowledge nodes have of their neighbors is the neighbor IDs and the IDs are ordered according to some criterion when performing topology control.

2.1.2 Quality Measures

Different approaches to topology control will produce different results. For a collection of nodes, let denote the graph on for which there is an edge from node to node only if can directly reach. It is desirable to judge the usefulness of a topology returned by a topology control algorithm and compare it with results from other algorithms. In order to do this, some metrics and measures are required which include connectivity, energy efficiency, throughput, and robustness to mobility.

2.1.2.1 Connectivity: If there is a multihop path between and in, then there should also be a path in. This is a basic requirement for a topology control algorithm, that it should not disconnect a connected graph.

2.1.2.2 Energy Efficiency: The energy consumed for a transmission between u and v is a polynomial function of the distance between u and v. Two common notions of energy efficiency are the energy stretch factor and the hop stretch factor. The energy stretch factor is the worst increase in energy used to deliver a packet between any pair of nodes and along a minimum energy path between the original graph and the topology controlled graph G. The hop stretch is similar except that the focus is on path length as opposed to energy consumption. Formally

$$\text{energy stretch factor} = \max_{u,v \in V} \frac{E_T(u,v)}{E_G(u,v)}$$

(1) where is the energy consumed along the most energy efficient path in graph. Likewise

$$\text{hop stretch factor} = \max_{u,v \in V} \frac{|(u,v)_T|}{|(u,v)_G|}$$

(2) where is the shortest path in graph and is its length.

2.1.2.3 Node Degree: In order to better evaluate the performance of the topology control technique in terms of interference, a distinction is made between the physical and the logical node degree. The physical node degree refers to the number of neighbor nodes that are within the transmitter range of a given node. The logical node degree refers to the number of neighbor nodes that a given node is linked to.

2.1.2.4 Simplicity and Maintainability: It is desirable for a topology to be simple and easy to maintain and objective measures that can be used to evaluate these subjective goals are the number of edges in and the maximum node degree (number of neighbors) of any node in. It is desirable also for the algorithm used to have little overhead in terms of computation and communication requirements.

2.1.2.5 Throughput: It is desirable for the network topology to have a high throughput, where it is possible to sustain a comparable amount of traffic as the original network topology. Several throughput measures can be used [15] one of which is the bit-meter which is defined in terms of the bit-distance product. A network transports one bit-meter when it one bit is transported a distance of one meter. The throughput of the network is then the number of bit-meters transported per second.

2.1.2.6 Robustness to Mobility: The mobility of nodes causes neighborhood relationships to change in the original graph and some other nodes will have to change their topology information. A robust topology should only require a small number of these adaptations and avoid the effects of reorganization due to local node movement affecting the entire network. A measure of robustness is the adaptability which is the maximum.

2.2 ITCD ALGORITHM

ITCD Algorithm [1] describes a cross-layer distributed algorithm called interference-based topology control algorithm for delay-constrained (ITCD) MANETs with considering both the interference constraint and the delay constraint, which is different from the previous work. The transmission delay, contention delay and the queuing delay are taken into account in the proposed algorithm. Moreover, the impact of node mobility on the interference-based

topology control algorithm is investigated and the unstable links are removed from the topology.

2.2.1 Delay Model

2.2.1.1 Delay model of a path:

The end-to-end delay contains transmission delay over intermediate links, contention delay caused by nodes' contention for the shared channel and queuing delay induced at each intermediate node due to queuing policy/or severe channel conditions. The transmission delay is the time for successful transmission, which is defined as the period from the instant that a packet is transmitted for the first time to the instant that it is either successfully transmitted or dropped after a predefined number of retransmissions. The contention delay is the access delay. And each retransmission will cause new access delay. The contention delay is determined by the contention window (CW) size of node, and the contention window size reflects the contention level. The queuing delay at an intermediate node can be interpreted as the interval between the time a packet reaches the node and the time this packet is to be transmitted.

For a path $P : n_1, n_2, \dots, n_i, \dots, n_N (N \geq 1)$, a packet is sent from node n_1 to n_N according to path P . $L_{(i)(i+1)}$ is the transmission delay of link between node i and node $i + 1$. Let C_i and Q_i denote the contention delay and queuing delay at node i , respectively. The total delay D_P contains the contention delay and the queuing delay at each node and the transmission delay of links on the path P .

$$D_P = \sum_{i=1}^{N-1} (L_{(i)(i+1)} + C_i + Q_i).$$

2.2.1.2 Delay model of an intermediate node:

If the data is transmitted successfully in the first attempt, transmission delay of link between node i and node $i + 1$ is

$$L_{(i)(i+1)} = \frac{L}{B} + DIFS + T_{ACK} + SIFS,$$

where L denotes the packet length and B is transmission data rate, $DIFS$ stands for the Distributed Inter-Frame Spacing, $SIFS$ stands for the Short Inter-Frame Spacing and T_{ACK} represents the transmission delay of acknowledge frame.

2.2.1.3 Delay constraint at an intermediate node:

From the above equations, the delay constraint for a path is transformed into delay constraints at intermediate nodes. However, it is an extremely hard problem to partition the end-to-end delay constraint into each node accurately. We define a max delay D_{max} at intermediate nodes, which is similar to the max transmit power. Obviously, D_{max} is determined by the information of the real-time requirement T_{real} and the number of hops n . T_{real} is given by the requirement of applications. As to n , we use a prediction method to estimate the number of hops.

2.2.2 Mobility

Delay and topology control algorithm have been studied under the assumption that all nodes in the networks are stationary. Then the impact of mobility should be investigated. Firstly, our algorithm focuses on reducing a network interference to improve capacity while keeping connectivity and delay requirements. Most of the nodes have minimum connectivity. Frequent link breakages are prone to happen in the mobile environment. The poor links which are easily broken should be moved from the topology to reduce the effects of mobility. Secondly, if a receiving node moves around in a small area in the transmission range of the sender in a lower speed, delay at receiver is only determined by transmission delay, contention delay and queuing delay. If the node has a higher mobility, node may move out of the sender's transmission range quickly. The link between sender and receiver is unstable and prone to break. Once the link breaks, the transmission delay will become infinite. Thus, delay is also affected by mobility.

2.3 SMART BOUNDARY YAO GABRIEL GRAPH (SBYAOGG)

The first objective was that it should be energy efficient and the second was that it should have low interference. To meet the set out design objectives, the routing sub graph T produced by the topology control technique from the original graph G had to meet certain requirements.

2.3.1 Yao-Gabriel Graph With Smart Boundaries

The algorithm is a mixture of the Gabriel graph algorithm and the Yao graph algorithm, with the use of smart region boundaries. The algorithm is referred to as the Smart Boundary Yao Gabriel Graph (SBYaoGG).

3. ENERGY EFFICIENT, REDUCED DELAY AND MINIMUM DISTRIBUTED TOPOLOGY CONTROL ALGORITHM

3.1 Construction of EEDTCA

A heuristic that was used whilst forming the reduced topology graph was to align the axis of the first cone used in the Yao graph computation to the region where nodes are most densely deployed. This can be accomplished by obtaining the unit direction vectors of all the neighboring nodes and then calculating the average direction vector. The average direction vector is then used as the axis of the cone for the first Yao graph region. The neighbor direction vectors and the average direction vector are illustrated in Fig. 1.

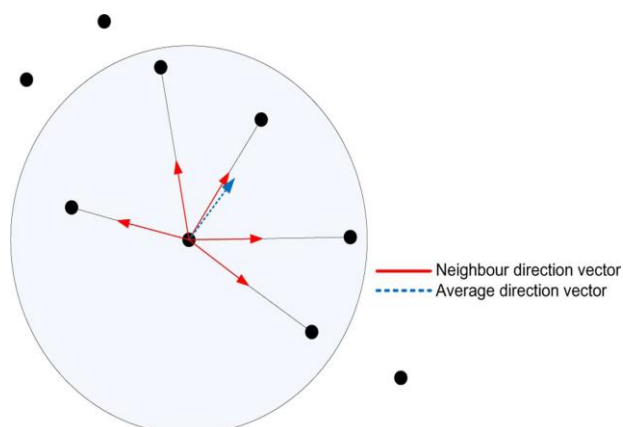


Figure 1 Neighbor direction vectors and the average direction vector.

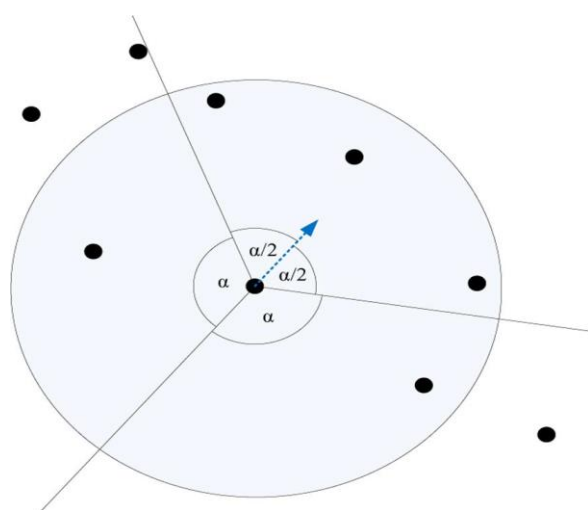


Figure 2 Graph boundaries using an average direction vector

3.2 The Algorithm

The following algorithm describes how to construct the EEDTCA, detailing the node in the network goes through.

- Step1: The node discovers its neighbor nodes by broadcasting at maximum power.
- Step2: The Gabriel graph is constructed locally.
- Step3: The unit direction vectors of neighbor nodes in the Gabriel graph are computed.
- Step4: The average direction vector is computed.
- Step5: The axis of the cone of the first region to use in computing the Yao graph is set to correspond to the average direction vector.
- Step6: The Yao graph is computed from the Gabriel graph, producing the reduced topology.

The final step in obtaining the EEDTCA is to optimize the reduced topology in order to ensure low interference and good power spanner properties. Two optimizations were made.

- 1) All edges are made symmetric by adding the reverse edge for any asymmetric link.
- 2) Transmitter power levels are set to the lowest level that will allow each node to reach all the nodes with which it has an edge.

After this the EEDTCA is fully formed and can be used as input to a routing algorithm.

4. PERFORMANCE EVALUATION

4.1 Simulation Environment

In order to evaluate the performance of the proposed EEDTCA protocol, we compare EEDTCA with the conventional ITCD [1] protocol and the energy-efficient and delay-constrained routing protocol which is to find an energy-efficient path with explicit delay constraint. Adjusting the transmission power in data and set the pause-time to 0. The simulation time for each simulation scenario is set to 50 seconds. In the results, each data point represents the average of 20 trials of experiments. The confidence level is 95%, and the confidence interval is shown as a vertical bar in the figures. The detailed simulation parameters are shown in Table I.

The experiments are divided to three parts, and in each part we research the impact of one of the following parameters on the performance of routing protocols:

Table 1. Simulation parameters

SIMULATION PARAMETERS	
Simulation Parameter	NS-2(v2.34)
Simulation Time	50 s
Topology Size	1000 m * 1000 m
Min speed	0 m/s
Max speed	2 m/s
Max nodes	100
Pause time	0 s
Traffic Type	CBR
Packet size	512 bytes
Mobility mode	Random way point

Number of nodes: We vary the number of nodes from 50 to 100 in a fixed field to research the impact of different network density. In this part, we set the number of CBR connections to 10.

Number of CBR connections: We vary the number of randomly chosen CBR connections from 2 to 10 with a fixed packet rate to research the impact of different traffic load. In this part, we set the number of nodes to 100.

Delay constraint: We vary the delay constraint from 40ms to 140ms in a fixed field to research the impact of delay constraint. In this part, we set the number of nodes to 100, the number of CBR connections to 15.

4.2 Performance with Varied Number of Nodes

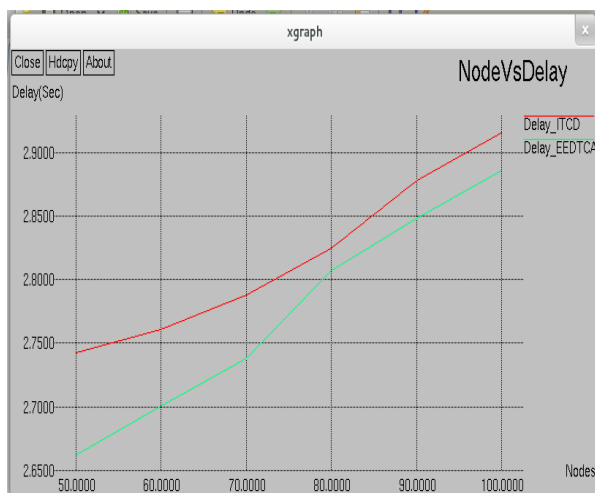


Figure3. Performance of delay with varied Number of Nodes.

Figure. 3 measures the average end-to-end delay of CBR packets received at the destinations with increasing network density. Average delay is defined as the average delay of a successfully delivered CBR packet from the source node to the destination node. In MANETs, inappropriate transmission power will increase the delay. If transmission power is too large, it will incur too many channel contentions, which increases the backoff timer in MAC layer, so as to increase the delay. EEDTCA protocol shows minimum delay while comparing with ITCD.

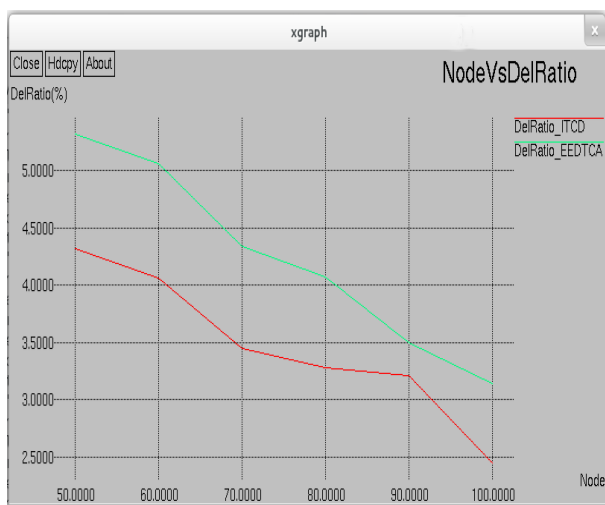


Figure4. Packet delivery ratio with varied number of Nodes.

Figure. 4 shows the packet delivery ratio with increasing network density. Hence, the EEDTCA protocol can increase the packet delivery ratio. On average, the packet delivery ratio is improved in the EEDTCA protocol when compared with the conventional ITCD protocol.

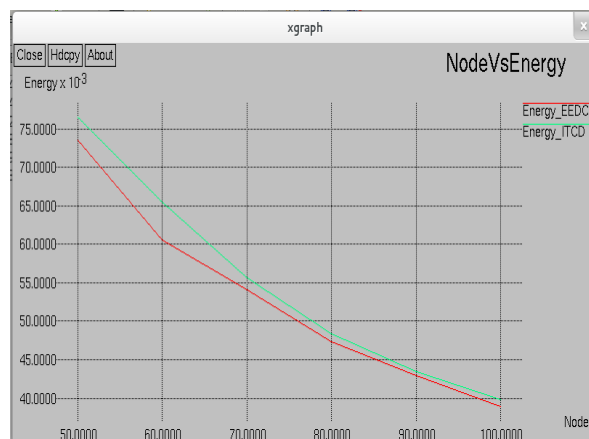


Figure5. Performance with Varied Energy with Node

Figure. 5 describes the energy consumption in the network with increasing the node density. The energy consumption of EEDTCA protocol is lower while comparing with the existing ITCD routing protocol.

4.3 Performance with Varied Number of CBR Connections



Figure 6. Performance of Delay with varied network traffic (ms)

Fig. 6 measures the average end-to-end delay of CBR packets received at the destinations with increasing traffic load. On average, the end to-end delay is reduced in the EEDTCA protocol when compared with the conventional ITCD protocol while increasing the traffic load.

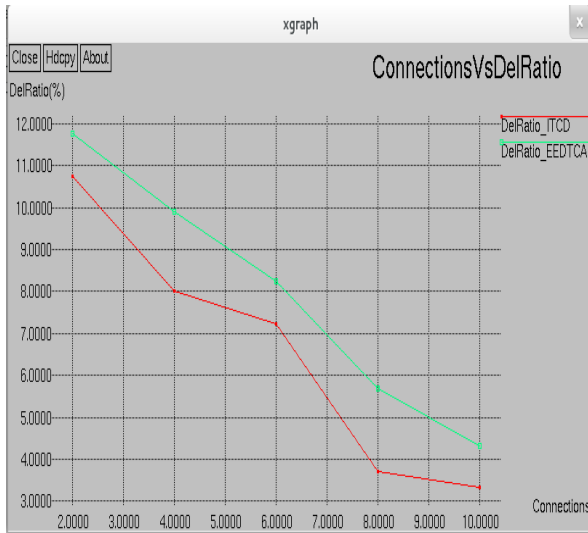


Figure 7. Performance of Packet Delivery Ratio with varied network traffic (ms)

Fig. 7 shows the packet delivery ratio with increasing network traffic. The EEDTCA protocol can increase the packet delivery ratio. The packet delivery ratio is improved in the EEDTCA protocol when compared with the conventional ITCD protocol.

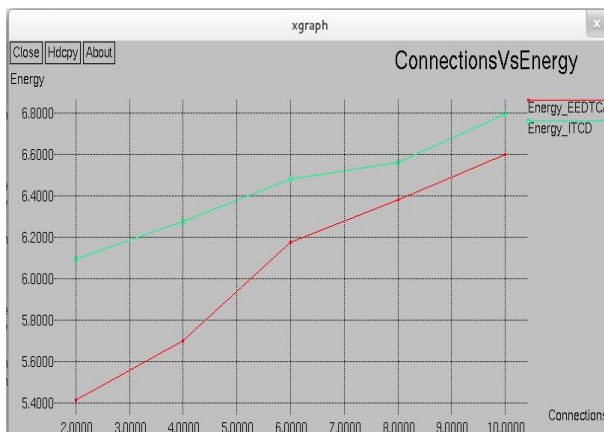


Figure 8. Performance with Varied Node Connection with energy

Fig. 8 describes the energy consumption of EEDTCA protocol. The energy consumption of EEDTCA protocol is low while comparing with the existing ITCD routing protocol.

5. CONCLUSION

In this paper, we propose energy efficient, reduced delay and minimum distributed topology control algorithm for mobile ad hoc networks. The simulation results show that EEDTCA can reduce the delay and improve the packet delivery performance effectively with efficient energy in mobile ad hoc networks. In future we can study behavior of this algorithm for sensor networking environment

6. REFERENCES

[1] Xin Ming Zhang, Member, IEEE, Yue Zhang, Fan Yan, Athanasios V.Vasilakos, Senior Member, IEEE, April 2015, Interference-Based Topology Control Algorithm for Delay-Constrained Mobile Ad Hoc Networks.

[2] Steve A. Borbas and Esther H. Jennings, Neural Networks, 2002. IJCNN '02. Proceedings of the 2002 International Joint Conference on 2002, Distributed Topology Control Algorithm for Multihop Wireless Networks.

[3] F. Xie, X.M. Zhang, J.F. Guo, and G.L. Chen, "A delay oriented adaptive routing protocol for mobile ad hoc networks,(in Chinese with English abstract)," Journal of Software, vol. 16, no. 9, pp. 1661-1667, 2005.

[4] N. Burri, P.V. Rickenbach, R.Wattenhofer and Y. Weber, "Topology control made practical: increasing the performance of source routing," in Proc. 2nd International Conference on Mobile Ad-hoc and Sensor Networks, pp. 1-12, 2006

[5] Forman, G. 2003. An extensive empirical study of feature selection metrics for text classification. J. Mach. Learn. Res. 3 (Mar. 2003), 1289-1305.

[6] Brown, L. D., Hua, H., and Gao, C. 2003. A widget framework for augmented interaction in SCAPE.

[7] M. Kadivar, M.E. Shiri, and M. Dahghan, "Distributed topology control algorithm based on one- and two-hop neighbors' information for ad hoc networks," Computer Communications, vol. 32, no.2, pp. 368-375, 2009.

[8] Spector, A. Z. 1989. Achieving application requirements. In Distributed Systems, S. Mullender

Simulation of A TZFI Fed Induction Motor Drive Using Fuzzy Logic Control

S.Selvakumar
Dhanalakshmi Srinivasan
College of Engineering
Coimbatore,India

V.Kamatchi Kannan
Bannari Amman Institute of
Technology
Erode,India

B.J.C.Monica
Dhanalakshmi Srinivasan
College of Engineering
Coimbatore,India

Abstract: This paper deals with modeling and simulation of FLC based TZSI fed induction motor drive. DC in stepped up using TZ network. The output of TZ network is applied to the three phase inverter. The inverter supplies AC power to the induction motor. Open loop system, closed loop system with PI and FL controllers are simulated and their results are compared. The TZSI fed drive system has advantages like reduced hardware size, reduced settling time and improved system response.

Keywords: TZ network, FLC, settling time, PI controller.

1. INTRODUCTION

Modern power electronic applications, especially those directly connected to the grid, usually require some voltage boosting. Traditional voltage-source inverters (VSIs) are therefore not satisfactory since they can only step down voltages. To add boost functionality, Dc – Dc boost converters can be placed before the FSIs[1]. Alternatively, single-stage buck-boost inverters can be used like the Cuk, SEPIC, and other similar Dc – Ac inverters[2]. These inverters however do not have intensive follow –up research. On the contrary, research in another buck-boost inverter, named as the Z-source inverter, has grown rapidly with its modulation, dynamics, control and sizing studied in its applications do motor drives, solar generation and electric vehicles [12] have also been attempted using the same basic Z-source impedance network found in figure 1.

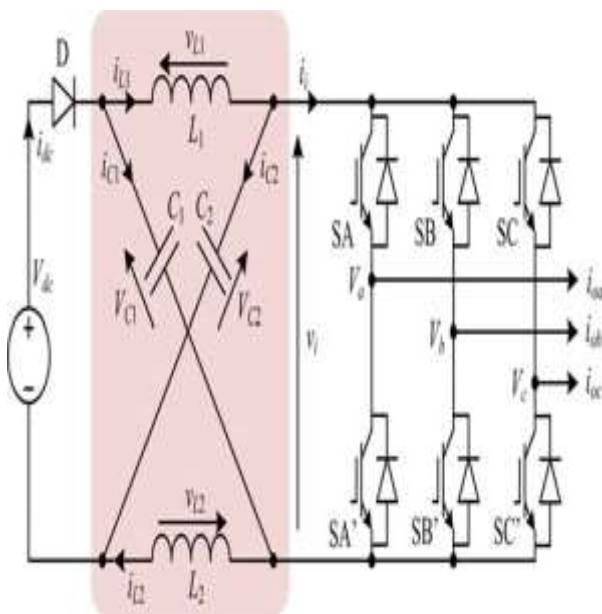


Figure 1. Traditional z-source inverter

Changes to the basic network only surface in, where their respective enhanced networks are name as improved, quasi,

and embedded Z-source networks[3]. Although named differently, these networks are closely similar with explaining that they differ only in their source placements. The three networks can eventually be merged into a single generic network with no changes introduced to the number of LC components and input-to-output gain[11]. The latter is subsequently mentioned as a concern in, whose solutions are to add extra inductors, capacitors, and diodes for further raising gain[9]. The amount of components added is however not economically justifiable. The investigation then continues with using coupled inductors or transformers for gain boosting[14]. The circuits discussed in are particularly interesting since they use only one coupled transformer and one capacitor, which are significantly lesser than those found in. They are respectively, named as T-source inverters in trans-Z inverters in after identifying a few more variations[4].

Although the inverters presented in are attractive, their common turns ratio might become too high at high gain. This is certainly in line with classical transformer theories, but is not an exclusive requirement, as demonstrated by the proposed T-Z-source inverters[6]. The proposed inverters again use a transformer and a capacitor for voltage boosting. Their gain is however raised by lowering their transformer turns ratio, rather than increasing it. This is a feature, which so far, has not been matched by other Z-source circuits[5]. Performances of the proposed circuits have already been tested in experiments.

2. Z-SOURCE AND TRANS-Z-SOURCE INVERTERS

The first Z-source inverter proposed in is shown in where a unique X-shaped impedance network can clearly be seen. This added network allows switches from the same phase-leg, to be turned ON simultaneously without causing damages[7]. Instead, the shoot-through state created causes the inverter output to be boosted without distortion if it is used properly with the other eight nonschool-through active and null states. The resulting expressions for computing the network capacitor voltage Vc. Peak de-link voltage during the no shoot-through state, and peak ac output voltage – can subsequently be derived and written in the following equation.

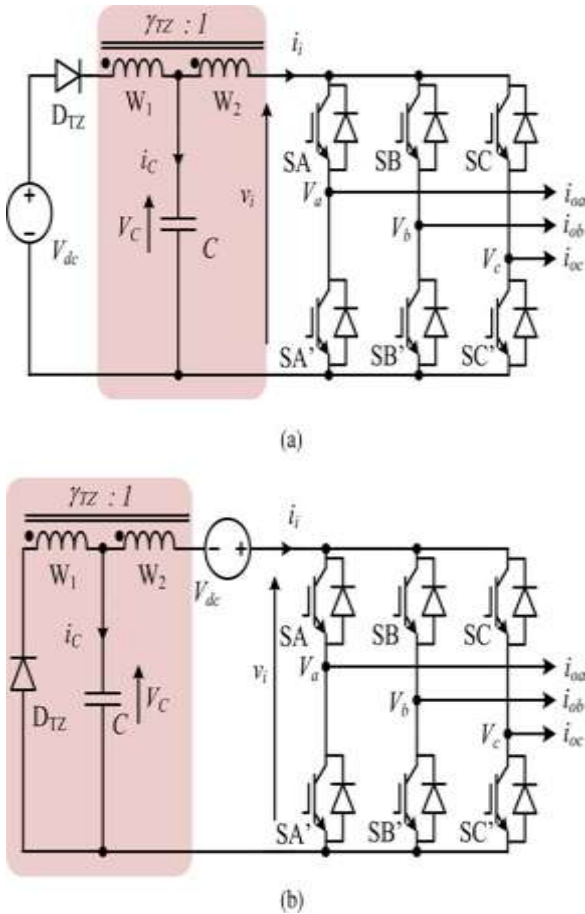


Figure 2. Trans Z-source inverter with source placed (a) diode or (b) VSI bridge

$$V_c = \frac{1 - d_{ST}}{1 - 2d_{ST}} V_{sc} \quad 0_1 = \frac{1}{1 - 2d_{ST}} V_{de} \quad (1)$$

$$0_u = M \frac{0_1}{2} = \frac{1}{2(1 - 2d_{ST})} (0.5MV_{de}) \quad (2)$$

Where V_{dc} , M and d_{ST} represent the input voltage, modulation ratio, and fractional shoot-through time, respectively.

The boost factor from hence expressed as $B = 1/(1 - 2d_{ST})$. Setting its denominator to be greater than zero then results in the operating range of $0 \leq d_{ST} < 0.5$. Since the shoot-through state can only be placed within a null interval to avoid introducing volt-see error, relationship between M and d_{ST} can further be written as $M \leq 1.15(1 - d_{ST})$. To produce a high-voltage boost, M must hence be lowered. Lower M how ever leads to high-voltage stresses across the components and poor spectral performances. To avoid these constraints, T-source or trans-Z-source inverters are proposed. In common, the rans-Z-source inverters shown in use only one transformer with turns ratio $Trz = W_1 / W_2$ and one capacitor. They differ only in their source placements, whose effect is to vary V_c but not the other voltages. This can clearly be seen from where

expressions for computing V_c , 0_1 , and 0 for the trans-Z-source inverters are presented.

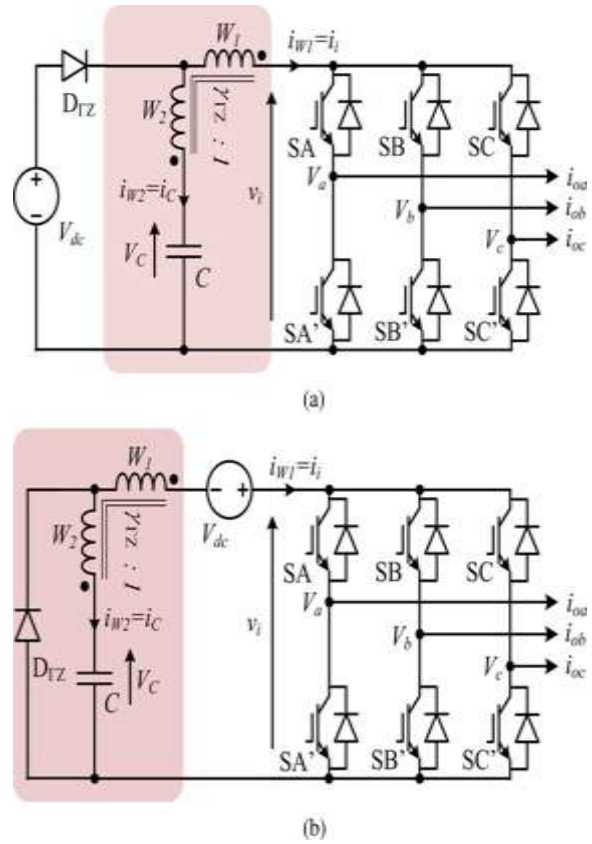


Figure 3. TZ source inverter with source placed in series with (a) diode or (b) VSI bridge

$$V_c = \frac{1 - d_{ST}}{1 - (rrz + 1)d_{ST}} V_{de} \quad (3)$$

$$V_c = \frac{rrxd_{ST}}{1 - (rrx + 1)d_{ST}} V_{sc} \quad (4)$$

$$0_1 = \frac{1}{1 - (rrz + 1)d_{ST}} V_{sc} \quad (5)$$

$$0_{sc} = \frac{1}{(rrz + 1)d_{ST}} (0.5MV_{dc}) \quad (6)$$

Comparing the denominators fo it is clear that the trans-Z-source gain can be raised above the traditional Z-source gain if Trz is set greater than one ($rrz \geq 1$). From the new limits for d_{ST} can also be determined as $0 \geq d_{ST} < 1/(rrz + 1)$. After setting the denominator of to be greater than zero. Clearly, the upper limit of d_{ST} can be reduced by using a higher rrz for gain boosting. The lower d_{ST} then leads to a higher modulation ratio since $M \leq 1.15(1 - d_{ST})$.

3. SIMULATION RESULTS

The Matlab/Simulink model of PI controlled closed loop system is shown in fig.4. the actual speed is measured and it is compared with a set speed. The error controls the pulse width to regulate the speed. Output voltage of TZ-Source inverter is shown in Fig.5. The speed response is shown in Fig.6. And torque response is shown in Fig.7. Macintosh, use the font named Times. Right margins should be justified, not ragged.

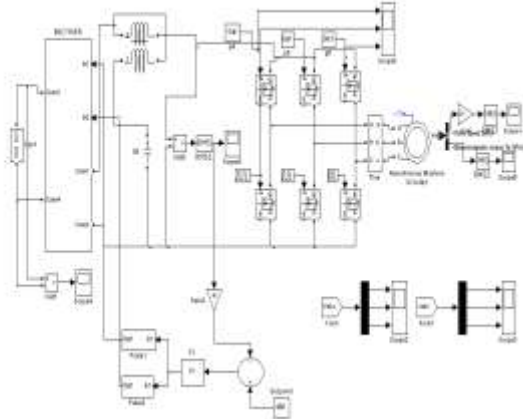


Figure 4. PI controlled closed loop induction motor drive

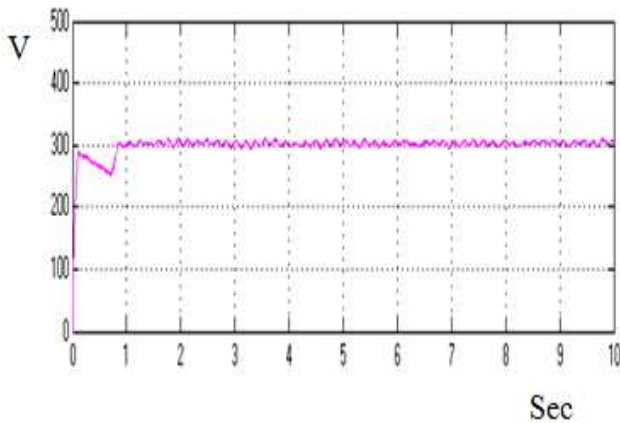


Figure 5. Closed loop PI fed TZ-source output voltage

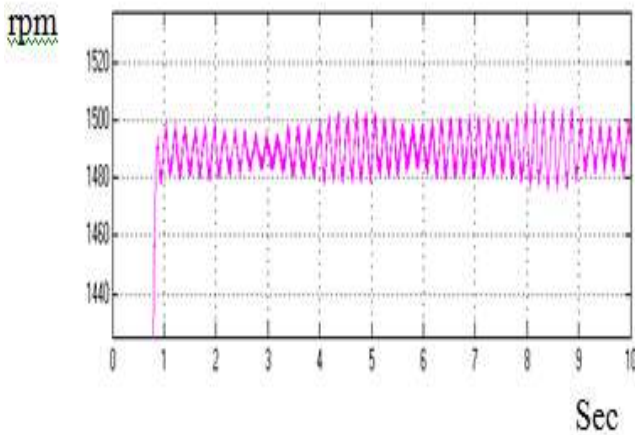


Figure 6. Closed loop PI fed induction motor speed curve

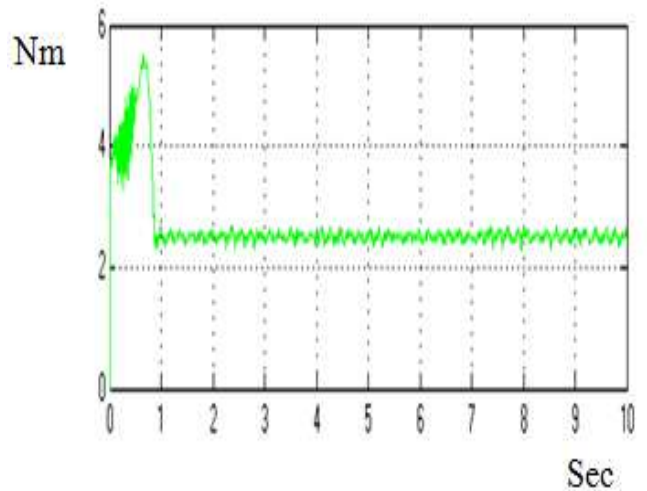


Figure 7. Closed loop PI fed induction motor torque curve

The Matlab/Simulink model of closed loop system with FLC is shown in Fig.8. The PI controller is replaced by FLC. The output voltage waveforms are shown in Fig.9. The speed and torque response are shown in Fig.10 and Fig.11 respectively.

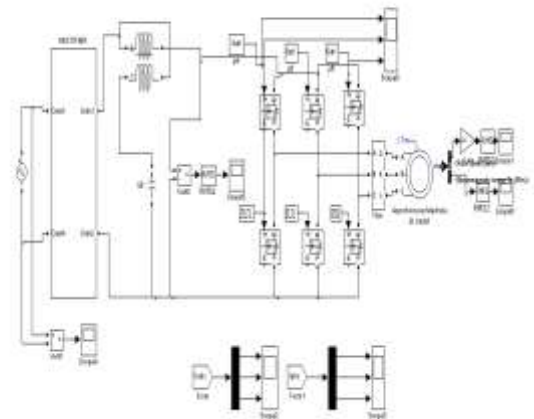


Figure 8. FLC controlled induction motor drive

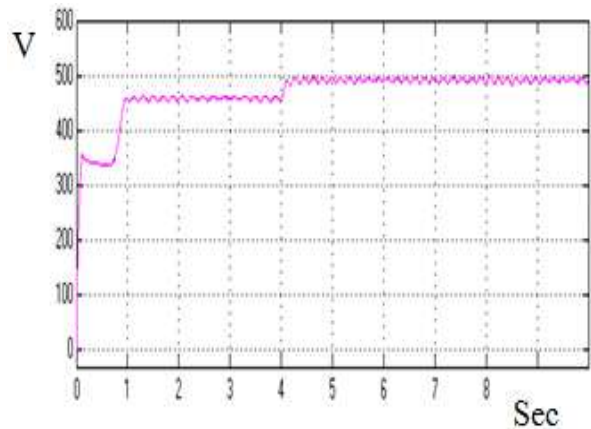


Figure 9. Closed loop FLC fed TZ-source output voltage

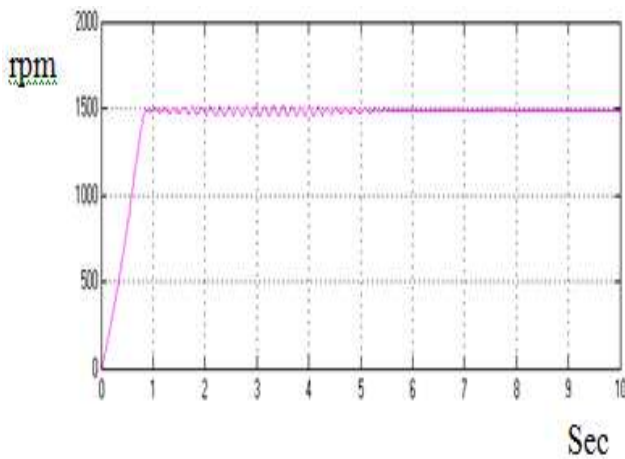


Figure 10. Closed loop FLC fed induction motor speed curve

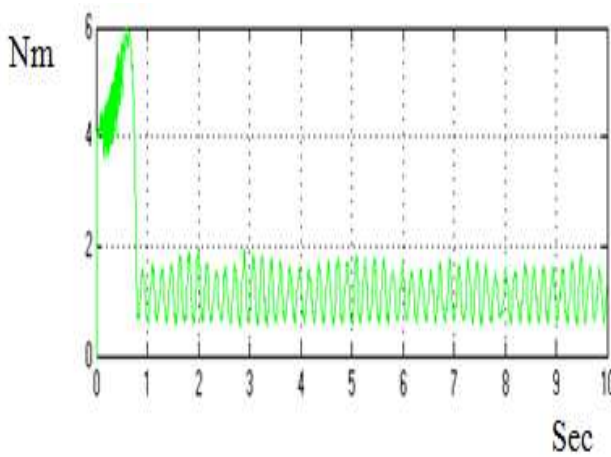


Figure 11. Closed loop FLC fed induction motor torque curve

4. COMPARISON TABLE

Table .1 Comparisons between PI and FLC controller

Controllers	Rise time (sec)	Settling time (sec)	Steady state error (rpm)
PI Controller	0.3	0.35	30
Fuzzy Logic Controller	0.25	0.26	0.5

5. CONCLUSION

FLC based TZSI fed induction motor drive is successfully modeled and simulated using Matlab/Simulink software. The comparison of PI & FLC controlled TZSI fed drives indicate that FLC has better response since the settling time and steady state error are reduced. This drive has advantages like minimum hardware size and steady state error. The disadvantage of TZSI is that it needs a coupled coil. The present work deals with comparison between PI and FLC

based systems. The comparison between PI & ANN systems will be done in future.

6. REFERENCES

- [1] J. Kikuchi and T. A. Lipo, "Three phase PWM boost-buck rectifiers with power regenerating capability," *IEEE Trans. Ind. Appl.*, vol. 38, no. 5, pp. 1361–1369, Sep./Oct. 2002.
- [2] G. Moschopoulos and Y. Zheng, "Buck-boost type ac-dc single-stageconverters," in *Proc. IEEE Int. Symp. Ind. Electron.*, Jul. 2006, pp. 1123–1128.
- [3] F. Z. Peng, "Z-source inverter," *IEEE Trans. Ind. Appl.*, vol. 39, no. 2, pp. 504–510, Mar./Apr. 2003.
- [4] P. C. Loh, D. M. Vilathgamuwa, Y. S. Lai, G. T. Chua, and Y. W. Li, "Pulse-width modulation of Z-source inverters," *IEEE Trans. Power Electron.*, vol. 20, no. 6, pp. 1346–1355, Nov. 2005.
- [5] J. Liu, J. Hu, and L. Xu, "Dynamic modeling and analysis of Z-source converter—Derivation of ac small signal model and design-oriented analysis," *IEEE Trans. Power Electron.*, vol. 22, no. 5, pp. 1786–1796, Sep. 2007.
- [6] G. Sen and M. E. Elbuluk, "Voltage and current-programmed modes in control of the Z-source converter," *IEEE Trans. Ind. Applicat.*, vol. 46, no. 2, pp. 680–686, Mar./Apr. 2010.
- [7] S. Rajakaruna and L. Jayawickrama, "Steady-state analysis and designing impedance network of Z-source inverters," *IEEE Trans. Ind. Electron.*, vol. 57, no. 7, pp. 2483–2491, Jul. 2010.
- [8] F. Z. Peng, A. Joseph, J. Wang, M. Shen, L. Chen, Z. Pan, E. Ortiz-Rivera, and Y. Huang, "Z-source inverter for motor drives," *IEEE Trans. Power Electron.*, vol. 20, no. 4, pp. 857–863, Jul. 2005.
- [9] M. Hanif, M. Basu, and K. Gaughan, "Understanding the operation of a Z-source inverter for photovoltaic application with a design example," *IET Power Electron.*, vol. 4, no. 3, pp. 278–287, Mar. 2011.
- [10] F. Z. Peng, M. Shen, and K. Holland, "Application of Z-source inverter for traction drive of fuel cell—Battery hybrid electric vehicles," *IEEE Trans. Power Electron.*, vol. 22, no. 3, pp. 1054–1061, May 2007.
- [11] Y. Tang, S. Xie, C. Zhang, and Z. Xu, "Improved Z-source inverter with reduced Z-source capacitor voltage stress and soft-start capability," *IEEE Trans. Power Electron.*, vol. 24, no. 2, pp. 409–415, Feb. 2009.
- [12] J. Anderson and F. Z. Peng, "A class of quasi-Z-source inverters," in *Proc. IEEE Ind. Appl. Soc.*, Oct. 2008, pp. 1–7.
- [13] P. C. Loh, F. Gao, and F. Blaabjerg, "Embedded EZ-source inverters," *IEEE Trans. Ind. Appl.*, vol. 46, no. 1, pp. 256–267, Jan./Feb. 2010.
- [14] F. Gao, P. C. Loh, F. Blaabjerg, and C. J. Gajanayake, "Operational analysis and comparative evaluation of embedded Z-Source inverters," in *Proc. IEEE Power Electron. Spec. Conf.*, Jun. 2008, pp. 2757–2763.

- [15] D. Li, F. Gao, P. C. Loh, M. Zhu, and F. Blaabjerg, "Hybrid-source impedance networks: Layouts and generalized cascading concepts," *IEEE Trans. Power Electron.*, vol. 26, no. 7, pp. 2028–2040, Jul. 2011.
- [16] M. Zhu, K. Yu, and F. L. Luo, "Switched inductor Z-source inverter," *IEEE Trans. Power Electron.*, vol. 25, no. 8, pp. 2150–2158, Aug. 2010.